GW240925 and GW250207: Astrophysical Calibration of Gravitational-wave Detectors

A. G. Abac,[1] I. Abouelfettouh,[2] F. Acernese,[3,4] K. Ackley,[5] A. Adam,[6] C. Adamcewicz,[7] S. Adhicary,[8] D. Adhikari,[9,10] N. Adhikari,[11] R. X. Adhikari,[12] V. K. Adkins,[13] S. Afroz,[14] A. Agapito,[15] D. Agarwal,[16] M. Agathos,[17] N. Aggarwal,[18] S. Aggarwal,[19] O. D. Aguiar,[20] I.-L. Ahrend,[21] L. Aiello,[22,23] A. Ain,[24] P. Ajith,[25] T. Akutsu,[26,27] S. Albanesi,[28,29] L. Albers,[30] W. Ali,[31,32] S. Al-Kershi,[9,10] C. Alléné,[33] A. Allocca,[34,4] S. Al-Shammari,[35] P. A. Altin,[36] S. Alvarez-Lopez,[37] W. Amar,[33] O. Amarasinghe,[35] A. Amato,[38,39] F. Amicucci,[40,41] C. Amra,[42] C. Anand,[7] A. Ananyeva,[12] S. B. Anderson,[12] W. G. Anderson,[12] M. Andia,[43] M. Ando,[44,45] M. Andrés-Carcasona,[37] J. L. Andrey,[46] T. Andrić,[47,48] J. Anglin,[49] J. Anna,[50] S. Ansoldi,[51,52] J. M. Antelis,[53] S. Antier,[43] M. Aoumi,[54] E. Z. Appavuravther,[55,56] S. Appert,[12] S. K. Apple,[57] K. Arai,[12] A. Araya,[58] M. C. Araya,[12] M. Arca Sedda,[47,48] F. Arciprete,[22,23] J. S. Areeda,[59] N. Aritomi,[2] F. Armato,[31,32] S. Armstrong,[60] N. Arnaud,[61] M. Arogeti,[62] S. M. Aronson,[49] K. G. Arun,[63] G. Ashton,[64] Y. Aso,[54,65] L. Asprea,[29] M. Assiduo,[66,67] S. Assis de Souza Melo,[68] S. M. Aston,[69] P. Astone,[40] F. Attadio,[41,40] F. Aubin,[70] K. AultONeal,[50] G. Avallone,[71] E. A. Avila,[53] S. Babak,[21] C. Badger,[72] S. Bae,[73] S. Bagnasco,[29] L. Baiotti,[74] R. Bajpai,[75] T. Baka,[76,39] K. A. Baker,[6] T. Baker,[77] G. Balbi,[78] G. Baldi,[79,80] N. Baldicchi,[81,55] M. Ball,[82] G. Ballardin,[68] S. W. Ballmer,[83] S. Banagiri,[7] B. Banerjee,[47] D. Bankar,[84] T. M. Baptiste,[13] P. Baral,[11] M. Baratti,[85,86] J. C. Barayoga,[12] K. Baric,[12] B. C. Barish,[12] D. Barker,[2] N. Barman,[84] P. Barneo,[87,88,89] F. Barone,[90,4] B. Barr,[91] M. Barrios,[92] L. Barsotti,[37] M. Barsuglia,[21] D. Barta,[93] M. A. Barton,[91] I. Bartos,[49] A. Basalaev,[9,10] R. Bassiri,[94] A. Basti,[86,85] M. Bawaj,[81,55] P. Baxi,[95] J. C. Bayley,[91] A. C. Baylor,[11] P. A. Baynard II,[62] M. Bazzan,[96,97] V. M. Bedakihale,[98] F. Beirnaert,[99] M. Bejger,[100] D. Belardinelli,[23] A. S. Bell,[91] C. Bellani,[101] L. Bellizzi,[85,86] D. Beltran-Martinez,[102] W. Benoit,[19] I. Bentara,[61] M. Ben Yaala,[60] S. Bera,[103] F. Bergamin,[35] B. K. Berger,[94] S. Bernuzzi,[28] M. Beroiz,[12] C. P. L. Berry,[91] I. Berry,[104] D. Bersanetti,[31] T. Bertheas,[105] A. Bertolini,[39,38] J. Betzwieser,[69] D. Beveridge,[6] G. Bevilacqua,[106] N. Bevins,[107] R. Bhandare,[108] R. Bhatt,[12] A. Bhattacharjee,[109] D. Bhattacharjee,[110,111] S. Bhattacharyya,[112] S. Bhaumik,[49] V. Biancalana,[106] A. Bianchi,[39,113] F. Bianchi,[55] I. A. Bilenko,[114] G. Billingsley,[12] A. Binetti,[101] S. Bini,[79,80,12] C. Binu,[115] S. Biot,[116] O. Birnholtz,[117] S. Biscoveanu,[118,119] A. Bisht,[10] M. Bitossi,[68,85] M.-A. Bizouard,[120] S. Blaber,[121] J. K. Blackburn,[12] L. A. Blagg,[82] C. D. Blair,[6,69] D. G. Blair,[6] N. Bode,[9,10] N. Boettner,[30] P. Bogdan,[122] G. Boileau,[120] M. Boldrini,[40] G. N. Bolingbroke,[123] A. Bolliand,[124,42] L. D. Bonavena,[49] R. Bondarescu,[87] F. Bondu,[125] V. A. Bonhomme,[37] E. Bonilla,[94] M. S. Bonilla,[59] A. Bonino,[126] R. Bonnand,[33,124] A. Borchers,[9,10] N. Borghi,[127,78] V. Boschi,[85] S. Bose,[128] V. Bossilkov,[69] Y. Bothra,[39,113] A. Boudon,[61] M. Boyle,[129] A. Bozzi,[68] C. Bradaschia,[85] M. J. Brady,[130] P. R. Brady,[11] A. Branch,[69] M. Branchesi,[47,48] T. Briant,[131] A. Brillet,[120] M. Brinkmann,[9,10] P. Brockill,[11] E. Brockmueller,[9,10] A. F. Brooks,[12] B. C. Brown,[49] D. D. Brown,[123] M. L. Brozzetti,[81,55] S. Brunett,[12] G. Bruno,[16] R. Bruntz,[122] J. Bryant,[126] Y. Bu,[132] F. Bucci,[67] J. Buchanan,[122] O. Bulashenko,[87,88] T. Bulik,[133] H. J. Bulten,[39] A. Buonanno,[134,1] K. Burtnyk,[2] R. Buscicchio,[135,136] D. Buskulic,[33] C. Buy,[105] R. L. Byer,[94] R. Cabrita,[16] V. Cáceres-Barbosa,[8] L. Cadonati,[62] G. Cagnoli,[137] C. Cahillane,[83] A. Calafat,[138] T. A. Callister,[139] E. Calloni,[34,4] S. R. Callos,[82] M. Canepa,[32,31] G. Caneva Santoro,[140] K. C. Cannon,[45] H. Cao,[37] L. A. Capistran,[141] E. Capocasa,[21] G. Capoccia,[55] E. Capote,[2] G. Capurri,[86,85] G. Carapella,[71,142] F. Carbognani,[68] K. J. Cardona-Martínez,[13] M. Carlassara,[9,10] J. B. Carlin,[132] T. K. Carlson,[143] M. F. Carney,[110] M. Carpinelli,[135,68] G. Carrillo,[82] J. J. Carter,[9,10] G. Carullo,[126] A. Casallas-Lagos,[144] J. Casanueva Diaz,[68] C. Casentini,[145,23] S. Caudill,[143] M. Cavaglià,[111] R. Cavalieri,[68] G. Cella,[85] S. Cepic,[127] P. Cerdá-Durán,[146,147] E. Cesarini,[23] N. Chabbra,[36] W. Chaibi,[120] A. Chakraborty,[14] P. Chakraborty,[9,10] S. Chakraborty,[108] S. Chalathadka Subrahmanya,[30] R. Chalmers,[77] C. Chan,[148] J. C. L. Chan,[149] M. Chan,[121] K. Chang,[150] P. Charlton,[151] E. Chassande-Mottin,[21] C. Chatterjee,[152] Debarati Chatterjee,[84] Deep Chatterjee,[37] M. Chaturvedi,[108] S. Chaty,[21] K. Chatziioannou,[12] A. Chen,[153] A. H.-Y. Chen,[154] D. Chen,[155] H. Chen,[156] H. Y. Chen,[157] S. Chen,[152] Y. Chen,[158] G. Cheng,[153] H. P. Cheng,[104] P. Chessa,[81,55] T. Cheunchitra,[132] H. T. Cheung,[95] S. Y. Cheung,[7] F. Chiadini,[159,142] G. Chiarini,[9,10] A. Chiba,[160] A. Chincarini,[31] D. Chintala,[110] M. L. Chiofalo,[86,85] A. Chiummo,[4,68] C. Chou,[161] S. Choudhary,[6] N. Christensen,[120,162] S. S. Y. Chua,[36] G. Ciani,[79,80] P. Ciecielag,[100] M. Cieślar,[133] M. Cifaldi,[23] B. Cirok,[163] F. Clara,[2] J. A. Clark,[12,62] T. A. Clarke,[7] P. Clearwater,[148] S. Clesse,[116] F. Cleva,[120] S. M. Clyne,[130] E. Coccia,[47,48,140] E. Codazzo,[164] P.-F. Cohadon,[131] D. E. Cohen,[9,10] S. Colace,[32] E. Colangeli,[77] O. Cole,[148] M. Colleoni,[138] C. G. Collette,[165] J. Collins,[69] S. Colloms,[91] A. Colombo,[166,136] C. M. Compton,[2] G. Connolly,[82] L. Conti,[97] T. R. Corbitt,[13] I. Cordero-Carrión,[167] S. Corezzi,[81,55] N. J. Cornish,[168] I. Coronado,[169] A. Corsi,[170] L. A. Corubolo,[22,23] L. Cotnoir,[122] R. Cottingham,[69] M. W. Coughlin,[19] P. Couvares,[12,62] D. M. Coward,[6] D. C. Coyne,[12] R. Coyne,[130] A. Cozzumbo,[47] J. D. E. Creighton,[11] T. D. Creighton,[171] S. Crook,[69]

R. Crouch,[2] J. Csizmazia,[2] J. R. Cudell,[172] T. J. Cullen,[12] A. Cumming,[91] E. Cuoco,[127,78] M. Cusinato,[146] L. V. Da Conceição,[173] T. Dal Canton,[43] S. Dall'Osso,[174,78] S. Dal Pra,[175] G. Dálya,[105] O. Dan,[117] Y. Dang,[8] B. D'Angelo,[31] S. Danilishin,[38,39] S. D'Antonio,[40] K. Danzmann,[9,10] K. E. Darroch,[122] L. P. Dartez,[69] R. Das,[112] A. Dasgupta,[98] V. Dattilo,[68] A. Daumas,[21] I. Dave,[108] A. Davenport,[176] M. Davier,[43] T. F. Davies,[6] D. Davis,[12] L. Davis,[6] M. C. Davis,[19] P. Davis,[177,178] E. J. Daw,[179] M. Dax,[1] J. De Bolle,[99] M. Deenadayalan,[84] J. Degallaix,[180] M. De Laurentis,[34,4] C. J. Delgado Mendez,[102] F. De Lillo,[24] S. Della Torre,[136] W. Del Pozzo,[86,85] O. M. del Rio,[181] A. Demagny,[33] F. De Marco,[41,40] G. Demasi,[182,67] F. De Matteis,[22,23] N. Demos,[37] T. Dent,[183] A. Depasse,[16] N. DePergola,[107] R. De Pietri,[184,185] R. De Rosa,[34,4] C. De Rossi,[68] M. Desai,[37] V. Deshmukh,[91] R. De Simone,[159,142] S. Determan,[186] A. Dhani,[1] R. Dhurkunde,[77] R. Diab,[49] C. Diaz,[102] M. C. Díaz,[171] M. Di Cesare,[34,4] G. Dideron,[187] T. Dietrich,[1] L. Di Fiore,[4] C. Di Fronzo,[6] M. Di Giovanni,[188,85] T. Di Girolamo,[34,4] D. Diksha,[39,38] J. Ding,[37,21,189] S. Di Pace,[41,40] I. Di Palma,[41,40] D. Di Piero,[190,52] F. Di Renzo,[67,182] Divyajyoti,[35] A. Dmitriev,[126] J. P. Docherty,[91] Z. Doctor,[118] N. Doerksen,[173] E. Dohmen,[2] A. Doke,[143] A. Domiciano De Souza,[191] L. D'Onofrio,[4] F. Donovan,[37] K. L. Dooley,[35] T. Dooney,[76] S. Doravari,[84] O. Dorosh,[192] F. Dosopoulou,[35] W. J. D. Doyle,[122] M. Drago,[41,40] J. C. Driggers,[2] M. Dubois,[105] R. R. Dumbreck,[35] L. Dunn,[132] U. Dupletsa,[47] D. D'Urso,[193,164] P. Dutta Roy,[49] H. Duval,[194] P.-A. Duverne,[21] S. E. Dwyer,[2] C. Eassa,[2] M. Eberhardt,[186] M. Ebersold,[195,33] T. Eckhardt,[30] G. Eddolls,[83] A. Effler,[69] J. Eichholz,[36] H. Einsle,[120] M. Eisenmann,[26] R. A. Eisenstein,[37] M. Emma,[64] K. Endo,[160] R. Enficiaud,[1] L. Errico,[34,4] R. Espinosa,[171] M. Esposito,[4,34] R. C. Essick,[196] H. Estellés,[1] T. Etzel,[12] M. Evans,[37] T. Evstafyeva,[187] B. E. Ewing,[8] J. M. Ezquiaga,[149] F. Fabrizi,[66,67] V. Fafone,[22,23] S. Fairhurst,[35] X. Fan,[153] A. M. Farah,[139] B. Farr,[82] W. M. Farr,[197,198] M. Favata,[199] M. Fays,[172] M. Fazio,[60] J. Feicht,[12] M. M. Fejer,[94] J.-N. Feldhusen,[30] E. Fenyvesi,[93,200] J. Fernandes,[201] T. Fernandes,[202,146] D. Fernando,[115] S. Ferraiuolo,[203,41,40] T. A. Ferreira,[13] M. Ferrer,[138] F. Fidecaro,[86,85] P. Figura,[100] E. Finch,[12] A. Fiori,[85,86] I. Fiori,[68] M. Fishbach,[196] R. P. Fisher,[122] R. Fittipaldi,[204,142] V. Fiumara,[205,142] R. Flaminio,[33] S. M. Fleischer,[181] L. S. Fleming,[206] E. Floden,[19] H. Fong,[121] J. A. Font,[146,147] F. Fontinele-Nunes,[19] C. Foo,[1] B. Fornal,[207] P. W. F. Forsyth,[36] K. Franceschetti,[184] A. Franco-Ordovas,[12] F. Frappez,[33] S. Frasca,[41,40] F. Frasconi,[85] J. P. Freed,[50] Z. Frei,[208] A. Freise,[39,113] O. Freitas,[202,146] R. Frey,[82] W. Frischhertz,[69] P. Fritschel,[37] V. V. Frolov,[69] M. Fuentes-Garcia,[12] S. Fujii,[209] T. Fujimori,[210] P. Fulda,[49] M. Fyffe,[69] B. Gadre,[76] J. R. Gair,[1] S. Galaudage,[191] V. Galdi,[211] R. Gamba,[8] A. Gamboa,[1] S. Gamoji,[212] A. Ganguly,[84] B. Garaventa,[31] P. García Abia,[102] J. García-Bellido,[213] C. García-Quirós,[195] J. W. Gardner,[36] S. Garg,[45] J. Gargiulo,[68] X. Garrido,[43] A. Garron,[138] F. Garufi,[34,4] P. A. Garver,[94] C. Gasbarra,[214,23] B. Gateley,[2] F. Gautier,[215] V. Gayathri,[11] T. Gayer,[83] G. Gemme,[31] A. Gennai,[85] V. Gennari,[105] J. George,[108] R. George,[157] O. Gerberding,[30] L. Gergely,[163] Archisman Ghosh,[99] Sayantan Ghosh,[201] Shaon Ghosh,[199] Shrobana Ghosh,[9,10] Suprovo Ghosh,[216] Tathagata Ghosh,[84] J. A. Giaime,[13,69] K. D. Giardina,[69] D. R. Gibson,[206] C. Gier,[60] S. Gkaitatzis,[86,85] J. Glanzer,[12] F. Glotin,[43] J. Godfrey,[82] R. V. Godley,[9,10] P. Godwin,[12] A. S. Goettel,[35] E. Goetz,[121] J. Golomb,[12] S. Gomez Lopez,[41,40] G. González,[13] P. Goodarzi,[46] S. Goode,[7] A. Goodwin-Jones,[16] M. Gosselin,[68] C. Gostiaux,[70] R. Gouaty,[33] D. W. Gould,[36] K. Govorkova,[37] A. Grado,[81,55] A. E. Granados,[19] M. Granata,[180] V. Granata,[217,142] S. Gras,[37] P. Grassia,[12] C. Gray,[2] R. Gray,[91] G. Greco,[55] A. C. Green,[39,113] L. Green,[218] S. M. Green,[77] S. R. Green,[219] A. M. Gretarsson,[50] E. M. Gretarsson,[50] H. K. Griffin,[19] D. Griffith,[12] H. L. Griggs,[62] G. Grignani,[81,55] C. Grimaud,[33] H. Grote,[35] S. Grunewald,[1] D. Guerra,[146] A. G. Guerrero,[139] D. Guetta,[220] G. M. Guidi,[66,67] T. Guidry,[2] H. K. Gulati,[98] F. Gulminelli,[177,178] A. M. Gunny,[37] H. Guo,[153] W. Guo,[6] Y. Guo,[39,38] Anuradha Gupta,[221] I. Gupta,[8] N. C. Gupta,[98] S. K. Gupta,[49] V. Gupta,[19] N. Gupte,[1] J. Gurs,[30] N. Gutierrez,[180] N. Guttman,[7] F. Guzman,[141] D. Haba,[222] M. Haberland,[1] S. Haino,[223] E. D. Hall,[37] E. Z. Hamilton,[138] G. Hammond,[91] M. Haney,[39] J. Hanks,[2] C. Hanna,[8] M. D. Hannam,[35] O. A. Hannuksela,[224] H. Hansen,[2] J. Hanson,[69] R. Harada,[45] A. R. Hardison,[186] S. Harikumar,[100] K. Haris,[225] I. Harley-Trochimczyk,[141] T. Harmark,[226] J. Harms,[47,48] G. M. Harry,[227] I. W. Harry,[77] J. Hart,[110] M. T. Hartman,[21] B. Haskell,[100,228,229] C.-J. Haster,[218] K. Haughian,[91] H. Hayakawa,[54] K. Hayama,[230] A. Heffernan,[138] D. Hegde,[16] M. C. Heintze,[69] J. Heinze,[126] J. Heinzel,[37] H. Heitmann,[120] F. Hellman,[92] A. F. Helmling-Cornell,[82] G. Hemming,[68] O. Henderson-Sapir,[123] M. Hendry,[91] I. S. Heng,[91] M. H. Hennig,[91] C. Henshaw,[62] M. Heurs,[9,10] A. L. Hewitt,[231,232] J. Heynen,[16] J. Heyns,[37] S. Higginbotham,[35] S. Hild,[38,39] S. Hill,[91] Y. Himemoto,[233] N. Hirata,[26] C. Hirose,[234] D. Hofman,[180] B. E. Hogan,[50] N. A. Holland,[39,113] K. Holley-Bockelmann,[152] I. J. Hollows,[179] D. E. Holz,[139] L. Honet,[116] K. M. Hoops,[212] M. E. Hoque,[235] D. J. Horton-Bailey,[92] J. Hough,[91] S. Hourihane,[12] N. T. Howard,[152] E. J. Howell,[6] C. G. Hoy,[77] C. A. Hrishikesh,[22] P. Hsi,[37] H.-F. Hsieh,[156] H.-Y. Hsieh,[156] C. Hsiung,[236] S.-H. Hsu,[237] W.-F. Hsu,[101] Q. Hu,[91] H. Y. Huang,[150] Y. Huang,[8] Y. T. Huang,[83] A. D. Huddart,[238] B. Hughey,[50] V. Hui,[33]

S. Husa,[138] L. Iampieri,[41,40] G. A. Iandolo,[38] M. Ianni,[23,22] G. Iannone,[142] J. Iascau,[82] K. Ide,[239] R. Iden,[222] A. Ierardi,[47,48] S. Ikeda,[155] H. Imafuku,[45] Y. Inoue,[150] G. Iorio,[96] P. Iosif,[190,52] J. Irwin,[91] R. Ishikawa,[239] T. Ishikawa,[240] M. Isi,[198] K. S. Isleif,[241] Y. Itoh,[210,242] S. Iwaguchi,[240] M. Iwaya,[209] B. R. Iyer,[25] C. D. Jackson,[49] C. Jacquet,[105] P.-E. Jacquet,[131] T. Jacquot,[43] S. J. Jadhav,[243] S. P. Jadhav,[148] M. Jain,[143] T. Jain,[231] A. L. James,[12] K. Jani,[152] J. Janquart,[16] N. N. Janthalur,[243] S. Jaraba,[244] P. Jaranowski,[245] R. Jaume,[138] W. Javed,[35] M. Jensen,[2] W. Jia,[37] J. Jiang,[104] H.-B. Jin,[246,247] G. R. Johns,[122] N. A. Johnson,[49] N. K. Johnson-McDaniel,[221] R. Johnston,[91] N. Johny,[9,10] D. H. Jones,[36] D. I. Jones,[216] R. Jones,[91] H. E. Jose,[82] P. Joshi,[62] S. K. Joshi,[84] G. Joubert,[61] J. Ju,[248] L. Ju,[6] I. L. Juarez-Reyes,[82] K. Jung,[249] J. Junker,[36] V. Juste,[116] H. B. Kabagoz,[37] T. Kajita,[209] I. Kaku,[210] V. Kalogera,[118] M. Kalomenopoulos,[218] M. Kamiizumi,[54] N. Kanda,[242,210] S. Kandhasamy,[84] G. Kang,[250] J. B. Kanner,[12] S. A. KantiMahanty,[19] S. J. Kapadia,[84] D. P. Kapasi,[59] M. Karthikeyan,[143] M. Kasprzack,[12] H. Kato,[160] T. Kato,[209] E. Katsavounidis,[37] W. Katzman,[69] R. Kaushik,[108] K. Kawabe,[2] R. Kawamoto,[210] D. Keitel,[138] S. A. Kemper,[57] L. J. Kemperman,[123] J. Kennington,[8] F. A. Kerkow,[19] R. Kesharwani,[84] J. S. Key,[251] R. Khadela,[9,10] S. Khadka,[94] S. S. Khadkikar,[8] F. Y. Khalili,[114] F. Khan,[9,10] T. Khanam,[170] M. Khursheed,[108] N. M. Khusid,[197,198] W. Kiendrebeogo,[120,252] N. Kijbunchoo,[123] C. Kim,[253] J. C. Kim,[254] K. Kim,[255] M. H. Kim,[248] S. Kim,[256] Y.-M. Kim,[255] C. Kimball,[118] K. Kimes,[59] M. Kinnear,[35] J. S. Kissel,[2] S. Klimenko,[49] A. M. Knee,[121] E. J. Knox,[82] N. Knust,[9,10] K. Kobayashi,[209] S. M. Koehlenbeck,[94] G. Koekoek,[39,38] K. Kohri,[257] K. Kokeyama,[35,240] S. Koley,[47,172] P. Kolitsidou,[126] A. E. Koloniari,[258] K. Komori,[44,45] K. Kompanets,[19] A. K. H. Kong,[156] A. Kontos,[259] K. Kopczuk,[110] L. M. Koponen,[126] M. Korobko,[30] X. Kou,[19] A. Koushik,[24] N. Kouvatsos,[72] M. Kovalam,[6] T. Koyama,[160] D. B. Kozak,[12] E. Kraja,[68] S. L. Kranzhoff,[38,39] V. Kringel,[9,10] N. V. Krishnendu,[126] S. Kroker,[260] A. Królak,[261,192] K. Kruska,[9,10] J. Kubisz,[262] G. Kuehn,[9,10] A. Kulur Ramamohan,[36] Achal Kumar,[49] Anil Kumar,[243] Praveen Kumar,[183] Prayush Kumar,[25] Rahul Kumar,[2] Rakesh Kumar,[98] Saurabh Kumar,[63] J. Kume,[263,264,45] K. Kuns,[37] N. Kuntimaddi,[35] S. Kuroyanagi,[265,266] S. Kuwahara,[45] K. Kwak,[249] K. Kwan,[36] S. Kwon,[45] G. Lacaille,[91] D. Laghi,[195] A. H. Laity,[130] A. Lakhal,[131] E. Lalande,[267] M. Lalleman,[24] S. Lalvani,[118] M. Landry,[2] R. N. Lang,[37] J. Lange,[157] R. Langgin,[218] B. Lantz,[94] I. La Rosa,[138] A. Lartaux-Vollard,[43] P. D. Lasky,[7] L. Lavezzi,[29] J. Lawrence,[171] M. Laxen,[69] C. Lazarte,[146] A. Lazzarini,[12] C. Lazzaro,[268,164] P. Leaci,[41,40] L. Leali,[19] Y. K. Lecoeuche,[121] H. W. Lee,[269] J. Lee,[83] K. Lee,[248] R.-K. Lee,[156] R. Lee,[37] Sungho Lee,[270] Sunjae Lee,[248] Y. Lee,[150] Y. S. C. Lee,[132] I. N. Legred,[12] J. Lehmann,[9,10] L. Lehner,[187] M. Le Jean,[180,124] A. Lemaître,[271] M. Lenti,[67,182] M. Leonardi,[79,80,272] M. Lequime,[42] N. Leroy,[43] M. Lesovsky,[12] N. Letendre,[33] M. Lethuillier,[61] S. E. Levin,[46] Y. Levin,[7] S. Lexmond,[113] K. Leyde,[77] K. L. Li,[273] T. G. F. Li,[101] X. Li,[158] Y. Li,[118] Z. Li,[91] Q. Liang,[153] A. Lihos,[122] E. T. Lin,[156] F. Lin,[150] L. C.-C. Lin,[273] Y.-C. Lin,[156] C. Lindsay,[206] S. D. Linker,[212] A. Liu,[224] G. C. Liu,[236] Jian Liu,[6] S. Liu,[153] F. Llamas Villarreal,[171] J. Llobera-Querol,[138] R. K. L. Lo,[149] J.-P. Locquet,[101] S. C. G. Loggins,[274] M. R. Loizou,[143] L. T. London,[72,37] A. Longo,[66,67] D. Lopez,[172] M. Lopez Portilla,[76] A. Lorenzo-Medina,[183] V. Loriette,[43] M. Lormand,[69] G. Losurdo,[188,85] E. Lotti,[143] T. P. Lott IV,[62] J. D. Lough,[9,10] H. A. Loughlin,[37] C. O. Lousto,[115] N. K. Y Low,[132] N. Lu,[36] L. Lucchesi,[85] H. Lück,[9,10] O. Lukina,[37] D. Lumaca,[23] A. P. Lundgren,[275,276] L. Lunghini,[68,34,4] A. W. Lussier,[267] S. Ma,[187] X. Ma,[46] D. M. Macleod,[35] I. A. O. MacMillan,[12] A. Macquet,[43] S. S. Madekar,[140] K. Maeda,[160] S. Maenaut,[101] S. S. Magare,[84] R. M. Magee,[12] E. Maggio,[1] R. Maggiore,[39,113] M. Magnozzi,[31,32] P. Mahapatra,[35] M. Mahesh,[30] S. Majhi,[84] E. Majorana,[41,40] C. N. Makarem,[12] E. Makelele,[110] D. Malakar,[111] J. A. Malaquias-Reis,[20] U. Mali,[196] S. Maliakal,[12] A. Malik,[108] L. Mallick,[173,196] A.-K. Malz,[64] N. Man,[120] M. Mancarella,[103] V. Mandic,[19] V. Mangano,[193,164] B. Mannix,[82] G. L. Mansell,[83,37] M. Manske,[11] M. Mantovani,[68] M. Mapelli,[96,97,277] S. Marchetti,[96,97] C. Marinelli,[106] F. Marion,[33] A. S. Markosyan,[94] A. Markowitz,[12] E. Maros,[12] S. Marsat,[105] F. Martelli,[66,67] I. W. Martin,[91] R. M. Martin,[199] B. B. Martinez,[141] D. A. Martinez,[59] M. Martinez,[140,278] V. Martinez,[137] A. Martini,[79,80] J. C. Martins,[20] D. V. Martynov,[126] E. J. Marx,[37] L. Massaro,[38,39] A. Masserot,[33] M. Masso-Reid,[91] T. Masters,[110] S. Mastrogiovanni,[40] G. Mastropasqua,[78] T. Matcovich,[55] M. Matiushechkina,[9,10] A. Matte-Landry,[267] L. Maurin,[215] N. Mavalvala,[37] N. Maxwell,[2] G. McCarrol,[69] R. McCarthy,[2] D. E. McClelland,[36] S. McCormick,[69] L. McCuller,[12] L. I. McDermott,[128] S. McEachin,[122] C. McElhenny,[122] G. I. McGhee,[91] K. B. M. McGowan,[152] J. McIver,[121] A. McLeod,[6] T. McRae,[36] R. McTeague,[91] D. Meacher,[11] B. N. Meagher,[83] R. Mechum,[115] Q. Meijer,[76] A. Melatos,[132] C. S. Menoni,[176] F. Mera,[2] R. A. Mercer,[11] L. Mereni,[180] K. Merfeld,[170] E. L. Merilh,[69] G. Merino,[102] J. R. Mérou,[138] J. D. Merritt,[82] M. Merzougui,[120] C. Messick,[11] B. Mestichelli,[47] M. Meyer-Conde,[279] F. Meylahn,[9,10] A. Mhaske,[84] A. Miani,[79,80] H. Miao,[280] I. Michaloliakos,[49] C. Michel,[180] Y. Michimura,[12,45] H. Middleton,[126] D. P. Mihaylov,[110] S. J. Miller,[12] M. Millhouse,[62] E. Milotti,[190,52] V. Milotti,[96] Y. Minenkov,[23] E. M. Minihan,[50] Ll. M. Mir,[140]

L. Mirasola,[164,268] C.-A. Miritescu,[140] A. Mishra,[25] C. Mishra,[112] T. Mishra,[49] A. L. Mitchell,[39,113] J. G. Mitchell,[50] O. Mitchem,[82] S. Mitra,[84] V. P. Mitrofanov,[114] K. Mitsuhashi,[26] R. Mittleman,[37] O. Miyakawa,[54] S. Miyoki,[54] G. Mo,[37] L. Mobilia,[66,67] S. R. P. Mohapatra,[12] S. R. Mohite,[8] M. Molina-Ruiz,[92] M. Mondin,[212] M. Montani,[66,67] C. J. Moore,[231] D. Moraru,[2] A. More,[84] S. More,[84] C. Moreno,[281] E. A. Moreno,[37] G. Moreno,[2] A. Moreso Serra,[87] C. Morgan,[35] S. Morisaki,[209] Y. Moriwaki,[160] G. Morras,[213] A. Moscatello,[96] M. Mould,[37] B. Mours,[70] C. M. Mow-Lowry,[39,113] L. Muccillo,[182,67] F. Muciaccia,[41,40] Arunava Mukherjee,[235] D. Mukherjee,[126] Samanwaya Mukherjee,[25] Soma Mukherjee,[171] Subroto Mukherjee,[98] Suvodip Mukherjee,[14] N. Mukund,[37] A. Mullavey,[69] A. R. Muller,[91] C. L. Mungioli,[6] M. Murakoshi,[239] P. G. Murray,[91] D. Nabari,[79,80] S. L. Nadji,[9,10] S. Nadji,[180] A. Nagar,[29,282] N. Nagarajan,[91] K. Nakagaki,[54] K. Nakamura,[26] H. Nakano,[283] M. Nakano,[12] D. Nanadoumgar-Lacroze,[140] D. Nandi,[13] V. Napolano,[68] S. U. Naqvi,[112] P. Narayan,[221] I. Nardecchia,[23] T. Narikawa,[209] H. Narola,[76] L. Naticchioni,[284,40] R. K. Nayak,[285] J. Neeson,[35] L. Negri,[76] A. Nela,[91] C. Nelle,[82] A. Nelson,[141] T. J. N. Nelson,[69] A. Nemmani,[100] M. Nery,[9,10] A. Neunzert,[2] M. Newell,[17] S. Ng,[59] L. Nguyen Quynh,[286] A. B. Nielsen,[287] Y. Nishino,[26,288] A. Nishizawa,[289] S. Nissanke,[290,39] W. Niu,[8] F. Nocera,[68] J. Noller,[291] M. Norman,[35] C. North,[35] J. Novak,[244,292] R. Nowicki,[152] J. F. Nuño Siles,[213] G. Nurbek,[171] L. K. Nuttall,[77] K. Obayashi,[239] J. Oberling,[2] C. E. Ochoa,[46] J. O'Dell,[238] M. Oertel,[244,292] G. Oganesyan,[47,48] T. O'Hanlon,[69] M. Ohashi,[54,279] F. Ohme,[9,10] I. Oke,[60] R. Omer,[19] B. O'Neal,[122] M. Onishi,[160] K. Oohara,[293,294] B. O'Reilly,[69] M. Orselli,[55,81] R. O'Shaughnessy,[115] S. Oshino,[54] C. Osthelder,[12] I. Ota,[13] G. Othman,[241] D. J. Ottaway,[123] A. Ouzriat,[61] H. Overmier,[69] B. J. Owen,[109] R. Ozaki,[239] A. E. Pace,[8] R. Pagano,[13] M. A. Page,[26] A. Pai,[201] L. Paiella,[47] A. Pal,[295] S. Pal,[285] M. A. Palaia,[85,86] M. Pálfi,[208] P. P. Palma,[41,22,23] C. Palomba,[40] P. Palud,[21] H. Pan,[156] J. Pan,[6] K.-C. Pan,[156,156] P. K. Panda,[243] Shiksha Pandey,[8] Swadha Pandey,[37] P. T. H. Pang,[39,76] F. Pannarale,[41,40] K. A. Pannone,[59] B. C. Pant,[108] F. H. Panther,[6] M. Panzeri,[66,67] F. Paoletti,[85] A. Paolone,[40,296] A. Papadopoulos,[91] E. E. Papalexakis,[46] L. Papalini,[85,86] G. Papigkiotis,[258] A. Paquis,[43] A. Parisi,[81,55] B.-J. Park,[270] J. Park,[297] W. Parker,[69] G. Pascale,[9,10] D. Pascucci,[99] A. Pasqualetti,[68] R. Passaquieti,[86,85] L. Passenger,[7] D. Passuello,[85] O. Patane,[2] A. V. Patel,[150] D. Pathak,[84] A. Patra,[35] B. Patricelli,[86,85] B. G. Patterson,[35] K. Paul,[112] S. Paul,[82] E. Payne,[12] T. Pearce,[35] M. Pedraza,[12] A. Pele,[12] F. E. Peña Arellano,[298] X. Peng,[126] Y. Peng,[62] S. Penn,[299,83] M. D. Penuliar,[59] A. Perego,[79,80] Z. Pereira,[143] C. Périgois,[300,97,96] G. Perna,[96] A. Perreca,[47,48] J. Perret,[21] S. Perriès,[61] J. W. Perry,[39,113] S. Peters,[172] S. Petracca,[211] C. Petrillo,[81] H. P. Pfeiffer,[1] H. Pham,[69] K. A. Pham,[19] K. S. Phukon,[126] H. Phurailatpam,[224] M. Piarulli,[105] L. Piccari,[41,40] O. J. Piccinni,[36] M. Pichot,[120] A. Pied,[91] M. Piendibene,[86,85] F. Piergiovanni,[66,67] L. Pierini,[40] G. Pierra,[40] V. Pierro,[301,142] M. Pietrzak,[100] M. Pillas,[302] L. Pinard,[180] I. M. Pinto,[301,142,303,34] M. Pinto,[68] B. J. Piotrzkowski,[11] M. Pirello,[2] M. D. Pitkin,[231,91] A. Placidi,[55] E. Placidi,[41,40] M. L. Planas,[138] W. Plastino,[217,23] C. Plunkett,[37] R. Poggiani,[86,85] E. Polini,[120] J. Pomper,[85,86] L. Pompili,[1] J. Poon,[224] E. Porcelli,[39] A. S. Porter,[109] E. K. Porter,[21] C. Posnansky,[8] R. Poulton,[68] J. Powell,[148] G. S. Prabhu,[84] M. Pracchia,[172] B. K. Pradhan,[84] T. Pradier,[70] A. K. Prajapati,[98] K. Prasai,[304] R. Prasanna,[243] P. Prasia,[305] G. Pratten,[126] A. Praveen,[196] G. Principe,[190,52] G. A. Prodi,[79,80] P. Prosperi,[85] P. Prosposito,[22,23] A. Puecher,[1] J. Pullin,[13] P. Puppo,[40] M. Pürrer,[130] H. Qi,[17] M. Qiao,[153] J. Qin,[36] G. Quéméner,[178,124] V. Quetschke,[171] P. J. Quinonez,[50] R. Rading,[241] I. Rainho,[146] S. Raja,[108] C. Rajan,[108] B. Rajbhandari,[115] K. E. Ramirez,[69] F. A. Ramis Vidal,[138] M. Ramos Arevalo,[171] A. Ramos-Buades,[138,39] S. Ranjan,[62] M. Ranjbar,[46] K. Ransom,[69] P. Rapagnani,[41,40] B. Ratto,[50] A. Ravichandran,[143] A. Ray,[118] V. Raymond,[35] M. Razzano,[86,85] J. Read,[59] J. Regan,[218] T. Regimbau,[33] T. Reichardt,[148] S. Reid,[60] C. Reissel,[37] D. H. Reitze,[12] A. I. Renzini,[12,135,136] B. Revenu,[306,43] A. Revilla Peña,[87] L. Ricca,[16] F. Ricci,[41,40] M. Ricci,[40,41] A. Ricciardone,[86,85] J. Rice,[83] J. W. Richardson,[46] M. L. Richardson,[123] A. Rijal,[50] K. Riles,[95] H. K. Riley,[35] S. Rinaldi,[277] J. Rittmeyer,[30] C. Robertson,[238] F. Robinet,[43] M. Robinson,[2] A. Rocchi,[23] L. Rolland,[33] J. G. Rollins,[12] A. E. Romano,[307] R. Romano,[3,4] A. Romero-Rodríguez,[33] I. M. Romero-Shaw,[231] J. H. Romie,[69] S. Ronchini,[8] T. J. Roocke,[123] L. Rosa,[4,34] T. J. Rosauer,[46] C. A. Rose,[62] D. Rosińska,[133] M. P. Ross,[57] M. Rossello-Sastre,[138] S. Rowan,[91] K. Rowlands,[186] S. K. Roy,[197,198] S. Roy,[16] D. Rozza,[135,136] P. Ruggi,[68] N. Ruhama,[249] G. H. Ruiz,[274] E. Ruiz Morales,[308,213] K. Ruiz-Rocha,[152] V. Russ,[181] S. Sachdev,[62] T. Sadecki,[2] P. Saffarieh,[39,113] S. Safi-Harb,[173] M. R. Sah,[14] S. Saha,[156] T. Sainrat,[70] S. Sajith Menon,[220,41,40] K. Sakai,[309] Y. Sakai,[279] M. Sakellariadou,[72] S. Sakon,[8] O. S. Salafia,[166,136,135] F. Salces-Carcoba,[12] L. Salconi,[68] M. Saleem,[157] F. Salemi,[41,40] M. Sallé,[39] S. U. Salunkhe,[84] S. Salvador,[178,177] A. Salvarese,[157] A. Samajdar,[76,39] A. Sanchez,[2] E. J. Sanchez,[12] N. Sanchis-Gual,[146] J. R. Sanders,[186] E. M. Sänger,[1] F. Santoliquido,[47,48] F. Sarandrea,[29] T. R. Saravanan,[84] N. Sarin,[7] P. Sarkar,[9,10] A. Sasli,[19,258] P. Sassi,[55,81] B. Sassolas,[180] B. S. Sathyaprakash,[8,35] R. Sato,[234] S. Sato,[160] Yukino Sato,[160] Yu Sato,[160] O. Sauter,[49]

R. L. Savage,[2] T. Sawada,[54] H. L. Sawant,[84] S. Sayah,[180] V. Scacco,[22,23] D. Schaetzl,[12] M. Scheel,[158] A. Schiebelbein,[196] M. G. Schiworski,[83] P. Schmidt,[126] S. Schmidt,[76] R. Schnabel,[30] M. Schneewind,[9,10] R. M. S. Schofield,[82,2] K. Schouteden,[101] B. W. Schulte,[9,10] M. Schulz,[47,48] B. F. Schutz,[35,9,10] E. Schwartz,[310] M. Scialpi,[311] J. Scott,[91] S. M. Scott,[36] R. M. Sedas,[69] T. C. Seetharamu,[91] M. Seglar-Arroyo,[140] Y. Sekiguchi,[312] D. Sellers,[69] N. Sembo,[210] A. S. Sengupta,[313] E. G. Seo,[91] J. W. Seo,[101] V. Sequino,[34,4] M. Serra,[40] A. Sevrin,[194] T. Shaffer,[2] U. S. Shah,[62] M. A. Shaikh,[314] L. Shao,[315] J. Sharkey,[91] A. K. Sharma,[138] Preeti Sharma,[13] Priyanka Sharma,[108] Ritwik Sharma,[19] Sushant Sharma-Chaudhary,[19] P. Shawhan,[134] N. S. Shcheblanov,[316,271] E. Sheridan,[152] Z.-H. Shi,[156] R. Shimomura,[317] H. Shinkai,[317] S. Shirke,[84] D. H. Shoemaker,[37] D. M. Shoemaker,[157] R. W. Short,[2] S. ShyamSundar,[108] A. Sider,[165] H. Siegel,[197,198] V. Sierra,[281] D. Sigg,[2] L. Silenzi,[38,39] L. Silvestri,[41,175] M. Simmonds,[123] L. P. Singer,[318] Amitesh Singh,[221] Anika Singh,[12] D. Singh,[92] M. K. Singh,[35] N. Singh,[138] S. Singh,[222,26] M. R. Sinha,[7] A. M. Sintes,[138] V. Sipala,[193,164] V. Skliris,[35] B. J. J. Slagmolen,[36] T. J. Slaven-Blair,[6] J. Smetana,[126] D. A. Smith,[69] J. R. Smith,[59] L. Smith,[190,52] R. J. E. Smith,[7] W. J. Smith,[152] S. Soares de Albuquerque Filho,[66] K. Somiya,[222] I. Song,[156] S. Soni,[37] V. Sordini,[61] F. Sorrentino,[31] H. Sotani,[319] F. Spada,[85] V. Spagnuolo,[39] A. P. Spencer,[91] P. Spinicelli,[68] A. K. Srivastava,[98] F. Stachurski,[91] C. J. Stark,[122] D. A. Steer,[320] N. Steinle,[173] J. Steinlechner,[38,39] S. Steinlechner,[38,39] N. Stergioulas,[258] P. Stevens,[43] M. StPierre,[130] M. D. Strong,[13] A. Strunk,[2] A. L. Stuver,[107,*] M. Suchenek,[100] S. Sudhagar,[100] Y. Sudo,[239] N. Sueltmann,[30] L. Suleiman,[59] K. D. Sullivan,[13] J. Sun,[254,250] L. Sun,[36] S. Sunil,[98] J. Suresh,[120] B. J. Sutton,[72] P. J. Sutton,[35] K. Suzuki,[222] M. Suzuki,[209] A. Svizzeretto,[81] S. Swain,[126] B. L. Swinkels,[39] A. Syx,[124] M. J. Szczepańczyk,[144] P. Szewczyk,[133] M. Tacca,[39] M. Tagliazucchi,[127,78] H. Tagoshi,[209] S. C. Tait,[12] K. Takada,[209] H. Takahashi,[279] R. Takahashi,[26] A. Takamori,[58] S. Takano,[9,10] H. Takeda,[321,322] K. Takeshita,[222] I. Takimoto Schmiegelow,[47,48] M. Takou-Ayaoh,[83] C. Talbot,[139] M. Tamaki,[209] N. Tamanini,[105] D. Tanabe,[150] K. Tanaka,[54] S. J. Tanaka,[239] S. Tanioka,[35] D. B. Tanner,[49] W. Tanner,[9,10] L. Tao,[46] R. D. Tapia,[8] E. N. Tapia San Martín,[39] C. Taranto,[22,23] A. Taruya,[323] J. D. Tasson,[162] J. G. Tau,[115] A. Tejera,[170] R. Tenorio,[138] H. Themann,[212] A. Theodoropoulos,[146] M. P. Thirugnanasambandam,[84] L. M. Thomas,[12] M. Thomas,[69] P. Thomas,[2] J. E. Thompson,[216] S. R. Thondapu,[108] K. A. Thorne,[69] E. Thrane,[7] J. Tissino,[47,48] A. Tiwari,[84] Pawan Tiwari,[47] Praveer Tiwari,[201] S. Tiwari,[195] V. Tiwari,[126] E. M. Todd,[91] M. R. Todd,[83] E. Tofani,[40] M. Toffano,[96] A. M. Toivonen,[19] K. Toland,[91] A. E. Tolley,[77] T. Tomaru,[26] V. Tommasini,[12] T. Tomura,[54] H. Tong,[7] C. Tong-Yu,[150] A. Torres-Forné,[146,147] C. I. Torrie,[12] I. Tosta e Melo,[324] E. Tournefier,[33] M. Trad Nery,[120] A. Trapananti,[56,55] R. Travaglini,[78] F. Travasso,[56,55] G. Traylor,[69] M. Trevor,[134] M. C. Tringali,[68] A. Tripathee,[95] G. Troian,[190,52] A. Trovato,[190,52] L. Trozzo,[4] R. J. Trudeau,[12] T. Tsang,[35] S. Tsuchida,[325] K. Tsuji,[240] L. Tsukada,[218] K. Turbang,[194,24] M. Turconi,[120] C. Turski,[99] H. Ubach,[87,88] A. S. Ubhi,[126] N. Uchikata,[209] T. Uchiyama,[54] R. P. Udall,[121] T. Uehara,[326] K. Ueno,[45] V. Undheim,[287] L. E. Uronen,[224] T. Ushiba,[54] M. Vacatello,[85,86] H. Vahlbruch,[9,10] G. Vajente,[12] J. Valencia,[138] M. Valentini,[113,39] E. Vallejo-Pagès,[140] S. A. Vallejo-Peña,[307] S. Vallero,[29] M. van Dael,[39,327] E. Van den Bossche,[194] J. F. J. van den Brand,[38,113,39] C. Van Den Broeck,[76,39] M. van der Kolk,[113] M. van der Sluys,[39,76] A. Van de Walle,[43] J. van Dongen,[39] K. Vandra,[107] M. VanDyke,[128] H. van Haevermaet,[24] J. V. van Heijningen,[39,113] P. Van Hove,[70] J. Vanier,[267] J. Vanosky,[2] N. van Remortel,[24] M. Vardaro,[38,39] A. F. Vargas,[132] V. Varma,[143] A. Vecchio,[126] G. Vedovato,[97] J. Veitch,[91] P. J. Veitch,[123] S. Venikoudis,[16] J. Venneberg,[37] R. C. Venterea,[19] P. Verdier,[61] M. Vereecken,[16] D. Verkindt,[33] B. Verma,[143] Y. Verma,[108] S. M. Vermeulen,[12] F. Vetrano,[66] A. Veutro,[40,41] A. Viceré,[66,67] S. Vidyant,[83] A. D. Viets,[328] A. Vijaykumar,[196] A. Vilkha,[115] N. Villanueva Espinosa,[146] V. Villa-Ortega,[183] E. T. Vincent,[62] J.-Y. Vinet,[120] S. Viret,[61] S. Vitale,[37] A. Vives,[82] L. Vizmeg,[181] H. Vocca,[81,55] D. Voigt,[30] E. R. G. von Reis,[2] J. S. A. von Wrangel,[9,10] W. E. Vossius,[241] L. Vujeva,[149] S. P. Vyatchanin,[114] J. Wack,[12] L. E. Wade,[110] M. Wade,[110] K. J. Wagner,[115] L. Wallace,[12] E. J. Wang,[94] H. Wang,[222] W. H. Wang,[171] Y. F. Wang,[1] Z. Wang,[153] G. Waratkar,[201] R. L. Ward,[36] J. Warner,[2] M. Was,[33] T. Washimi,[26] N. Y. Washington,[12] B. Weaver,[2] S. A. Webster,[91] N. L. Weickhardt,[30] M. Weinert,[9,10] A. J. Weinstein,[12] R. Weiss,[37,†] L. Wen,[6] K. Wette,[36] C. Wheeler,[69] J. T. Whelan,[115] B. F. Whiting,[49] C. Whittall,[126] E. G. Wickens,[77] D. Wilken,[9,10] B. M. Williams,[128] D. Williams,[91] M. J. Williams,[77] N. S. Williams,[1] J. L. Willis,[12] B. Willke,[9,10] M. Wils,[101] L. Wilson,[110] C. W. Winborn,[111] J. Winterflood,[6] C. C. Wipf,[12] G. Woan,[91] J. Woehler,[38,39] N. E. Wolfe,[37] H. T. Wong,[150] I. C. F. Wong,[101] K. Wong,[196] T. Wouters,[76,39] J. L. Wright,[2] M. Wright,[91,76] B. Wu,[83] C. Wu,[156] D. S. Wu,[9,10] H. Wu,[156] K. Wu,[128] Q. Wu,[57] Z. Wu,[105] E. Wuchner,[59] D. M. Wysocki,[11] V. A. Xu,[92] Y. Xu,[138] N. Yadav,[29] H. Yamamoto,[12] K. Yamamoto,[160] T. S. Yamamoto,[45] T. Yamamoto,[54] R. Yamazaki,[239] T. Yan,[126] H. Yang,[280] K. Z. Yang,[19] Y. Yang,[161] Z. Yarbrough,[13] J. Yebana,[138] S.-W. Yeh,[156] A. B. Yelikar,[152] X. Yin,[37] J. Yokoyama,[329,45,44] T. Yokozawa,[54] S. Yuan,[6] H. Yuzurihara,[54] M. Zanolin,[50]

M. Zeeshan,[115] T. Zelenova,[68] J.-P. Zendri,[97] M. Zeoli,[16] M. Zerrad,[42] M. Zevin,[118] H. Zhang,[153] L. Zhang,[12] N. Zhang,[62] R. Zhang,[104] T. Zhang,[126] C. Zhao,[6] Yue Zhao,[169] Yuhang Zhao,[21] Z.-C. Zhao,[330] Y. Zheng,[111] H. Zhong,[19] H. Zhou,[83] H. O. Zhu,[6] Z.-H. Zhu,[330, 331] Z. Zhu,[115] A. B. Zimmerman,[157] L. Zimmermann,[61] and M. E. Zucker[37, 12]

(The LIGO Scientific Collaboration, the Virgo Collaboration, and the KAGRA Collaboration)

[1]*Max Planck Institute for Gravitational Physics (Albert Einstein Institute), D-14476 Potsdam, Germany*
[2]*LIGO Hanford Observatory, Richland, WA 99352, USA*
[3]*Dipartimento di Farmacia, Università di Salerno, I-84084 Fisciano, Salerno, Italy*
[4]*INFN, Sezione di Napoli, I-80126 Napoli, Italy*
[5]*University of Warwick, Coventry CV4 7AL, United Kingdom*
[6]*OzGrav, University of Western Australia, Crawley, Western Australia 6009, Australia*
[7]*OzGrav, School of Physics & Astronomy, Monash University, Clayton 3800, Victoria, Australia*
[8]*The Pennsylvania State University, University Park, PA 16802, USA*
[9]*Max Planck Institute for Gravitational Physics (Albert Einstein Institute), D-30167 Hannover, Germany*
[10]*Leibniz Universität Hannover, D-30167 Hannover, Germany*
[11]*University of Wisconsin-Milwaukee, Milwaukee, WI 53201, USA*
[12]*LIGO Laboratory, California Institute of Technology, Pasadena, CA 91125, USA*
[13]*Louisiana State University, Baton Rouge, LA 70803, USA*
[14]*Tata Institute of Fundamental Research, Mumbai 400005, India*
[15]*Centre de Physique Théorique, Aix-Marseille Université, Campus de Luminy, 163 Av. de Luminy, 13009 Marseille, France*
[16]*Université catholique de Louvain, B-1348 Louvain-la-Neuve, Belgium*
[17]*Queen Mary University of London, London E1 4NS, United Kingdom*
[18]*University of California, Davis, Davis, CA 95616, USA*
[19]*University of Minnesota, Minneapolis, MN 55455, USA*
[20]*Instituto Nacional de Pesquisas Espaciais, 12227-010 São José dos Campos, São Paulo, Brazil*
[21]*Université Paris Cité, CNRS, Astroparticule et Cosmologie, F-75013 Paris, France*
[22]*Università di Roma Tor Vergata, I-00133 Roma, Italy*
[23]*INFN, Sezione di Roma Tor Vergata, I-00133 Roma, Italy*
[24]*Universiteit Antwerpen, 2000 Antwerpen, Belgium*
[25]*International Centre for Theoretical Sciences, Tata Institute of Fundamental Research, Bengaluru 560089, India*
[26]*Gravitational Wave Science Project, National Astronomical Observatory of Japan, 2-21-1 Osawa, Mitaka City, Tokyo 181-8588, Japan*
[27]*Advanced Technology Center, National Astronomical Observatory of Japan, 2-21-1 Osawa, Mitaka City, Tokyo 181-8588, Japan*
[28]*Theoretisch-Physikalisches Institut, Friedrich-Schiller-Universität Jena, D-07743 Jena, Germany*
[29]*INFN Sezione di Torino, I-10125 Torino, Italy*
[30]*Universität Hamburg, D-22761 Hamburg, Germany*
[31]*INFN, Sezione di Genova, I-16146 Genova, Italy*
[32]*Dipartimento di Fisica, Università degli Studi di Genova, I-16146 Genova, Italy*
[33]*Univ. Savoie Mont Blanc, CNRS, Laboratoire d'Annecy de Physique des Particules - IN2P3, F-74000 Annecy, France*
[34]*Università di Napoli "Federico II", I-80126 Napoli, Italy*
[35]*Cardiff University, Cardiff CF24 3AA, United Kingdom*
[36]*OzGrav, Australian National University, Canberra, Australian Capital Territory 0200, Australia*
[37]*LIGO Laboratory, Massachusetts Institute of Technology, Cambridge, MA 02139, USA*
[38]*Maastricht University, 6200 MD Maastricht, Netherlands*
[39]*Nikhef, 1098 XG Amsterdam, Netherlands*
[40]*INFN, Sezione di Roma, I-00185 Roma, Italy*
[41]*Università di Roma "La Sapienza", I-00185 Roma, Italy*
[42]*Aix Marseille Univ, CNRS, Centrale Med, Institut Fresnel, F-13013 Marseille, France*
[43]*Université Paris-Saclay, CNRS/IN2P3, IJCLab, 91405 Orsay, France*
[44]*Department of Physics, The University of Tokyo, 7-3-1 Hongo, Bunkyo-ku, Tokyo 113-0033, Japan*
[45]*Research Center for the Early Universe (RESCEU), The University of Tokyo, 7-3-1 Hongo, Bunkyo-ku, Tokyo 113-0033, Japan*
[46]*University of California, Riverside, Riverside, CA 92521, USA*
[47]*Gran Sasso Science Institute (GSSI), I-67100 L'Aquila, Italy*
[48]*INFN, Laboratori Nazionali del Gran Sasso, I-67100 Assergi, Italy*
[49]*University of Florida, Gainesville, FL 32611, USA*
[50]*Embry-Riddle Aeronautical University, Prescott, AZ 86301, USA*
[51]*Dipartimento di Scienze Matematiche, Informatiche e Fisiche, Università di Udine, I-33100 Udine, Italy*
[52]*INFN, Sezione di Trieste, I-34127 Trieste, Italy*
[53]*Tecnologico de Monterrey, Escuela de Ingeniería y Ciencias, 64849 Monterrey, Nuevo León, Mexico*
[54]*Institute for Cosmic Ray Research, KAGRA Observatory, The University of Tokyo, 238 Higashi-Mozumi, Kamioka-cho, Hida City, Gifu 506-1205, Japan*
[55]*INFN, Sezione di Perugia, I-06123 Perugia, Italy*
[56]*Università di Camerino, I-62032 Camerino, Italy*

[57]*University of Washington, Seattle, WA 98195, USA*
[58]*Earthquake Research Institute, The University of Tokyo, 1-1-1 Yayoi, Bunkyo-ku, Tokyo 113-0032, Japan*
[59]*California State University Fullerton, Fullerton, CA 92831, USA*
[60]*SUPA, University of Strathclyde, Glasgow G1 1XQ, United Kingdom*
[61]*Université Claude Bernard Lyon 1, CNRS, IP2I Lyon / IN2P3, UMR 5822, F-69622 Villeurbanne, France*
[62]*Georgia Institute of Technology, Atlanta, GA 30332, USA*
[63]*Chennai Mathematical Institute, Chennai 603103, India*
[64]*Royal Holloway, University of London, London TW20 0EX, United Kingdom*
[65]*Department of Astronomical Science, The Graduate University for Advanced Studies (SOKENDAI), 2-21-1 Osawa, Mitaka City, Tokyo 181-8588, Japan*
[66]*Università degli Studi di Urbino "Carlo Bo", I-61029 Urbino, Italy*
[67]*INFN, Sezione di Firenze, I-50019 Sesto Fiorentino, Firenze, Italy*
[68]*European Gravitational Observatory (EGO), I-56021 Cascina, Pisa, Italy*
[69]*LIGO Livingston Observatory, Livingston, LA 70754, USA*
[70]*Université de Strasbourg, CNRS, IPHC UMR 7178, F-67000 Strasbourg, France*
[71]*Dipartimento di Fisica "E.R. Caianiello", Università di Salerno, I-84084 Fisciano, Salerno, Italy*
[72]*King's College London, University of London, London WC2R 2LS, United Kingdom*
[73]*Korea Institute of Science and Technology Information, Daejeon 34141, Republic of Korea*
[74]*International College, Osaka University, 1-1 Machikaneyama-cho, Toyonaka City, Osaka 560-0043, Japan*
[75]*Accelerator Laboratory, High Energy Accelerator Research Organization (KEK), 1-1 Oho, Tsukuba City, Ibaraki 305-0801, Japan*
[76]*Institute for Gravitational and Subatomic Physics (GRASP), Utrecht University, 3584 CC Utrecht, Netherlands*
[77]*University of Portsmouth, Portsmouth, PO1 3FX, United Kingdom*
[78]*Istituto Nazionale Di Fisica Nucleare - Sezione di Bologna, viale Carlo Berti Pichat 6/2 - 40127 Bologna, Italy*
[79]*Università di Trento, Dipartimento di Fisica, I-38123 Povo, Trento, Italy*
[80]*INFN, Trento Institute for Fundamental Physics and Applications, I-38123 Povo, Trento, Italy*
[81]*Università di Perugia, I-06123 Perugia, Italy*
[82]*University of Oregon, Eugene, OR 97403, USA*
[83]*Syracuse University, Syracuse, NY 13244, USA*
[84]*Inter-University Centre for Astronomy and Astrophysics, Pune 411007, India*
[85]*INFN, Sezione di Pisa, I-56127 Pisa, Italy*
[86]*Università di Pisa, I-56127 Pisa, Italy*
[87]*Institut de Ciències del Cosmos (ICCUB), Universitat de Barcelona (UB), c. Martí i Franquès, 1, 08028 Barcelona, Spain*
[88]*Departament de Física Quàntica i Astrofísica (FQA), Universitat de Barcelona (UB), c. Martí i Franqués, 1, 08028 Barcelona, Spain*
[89]*Institut d'Estudis Espacials de Catalunya, c. Gran Capità, 2-4, 08034 Barcelona, Spain*
[90]*Dipartimento di Medicina, Chirurgia e Odontoiatria "Scuola Medica Salernitana", Università di Salerno, I-84081 Baronissi, Salerno, Italy*
[91]*IGR, University of Glasgow, Glasgow G12 8QQ, United Kingdom*
[92]*University of California, Berkeley, CA 94720, USA*
[93]*HUN-REN Wigner Research Centre for Physics, H-1121 Budapest, Hungary*
[94]*Stanford University, Stanford, CA 94305, USA*
[95]*University of Michigan, Ann Arbor, MI 48109, USA*
[96]*Università di Padova, Dipartimento di Fisica e Astronomia, I-35131 Padova, Italy*
[97]*INFN, Sezione di Padova, I-35131 Padova, Italy*
[98]*Institute for Plasma Research, Bhat, Gandhinagar 382428, India*
[99]*Universiteit Gent, B-9000 Gent, Belgium*
[100]*Nicolaus Copernicus Astronomical Center, Polish Academy of Sciences, 00-716, Warsaw, Poland*
[101]*Katholieke Universiteit Leuven, Oude Markt 13, 3000 Leuven, Belgium*
[102]*Centro de Investigaciones Energéticas Medioambientales y Tecnológicas, Avda. Complutense 40, 28040, Madrid, Spain*
[103]*Aix-Marseille Université, Université de Toulon, CNRS, CPT, Marseille, France*
[104]*Northeastern University, Boston, MA 02115, USA*
[105]*Laboratoire des 2 Infinis - Toulouse (L2IT-IN2P3), F-31062 Toulouse Cedex 9, France*
[106]*Università di Siena, Dipartimento di Scienze Fisiche, della Terra e dell'Ambiente, I-53100 Siena, Italy*
[107]*Villanova University, Villanova, PA 19085, USA*
[108]*RRCAT, Indore, Madhya Pradesh 452013, India*
[109]*University of Maryland, Baltimore County, Baltimore, MD 21250, USA*
[110]*Kenyon College, Gambier, OH 43022, USA*
[111]*Missouri University of Science and Technology, Rolla, MO 65409, USA*
[112]*Indian Institute of Technology Madras, Chennai 600036, India*
[113]*Department of Physics and Astronomy, Vrije Universiteit Amsterdam, 1081 HV Amsterdam, Netherlands*
[114]*Lomonosov Moscow State University, Moscow 119991, Russia*
[115]*Rochester Institute of Technology, Rochester, NY 14623, USA*
[116]*Université libre de Bruxelles, 1050 Bruxelles, Belgium*
[117]*Bar-Ilan University, Ramat Gan, 5290002, Israel*

[118]*Northwestern University, Evanston, IL 60208, USA*
[119]*Department of Physics, Princeton University, Princeton, NJ 08544, USA*
[120]*Université Côte d'Azur, Observatoire de la Côte d'Azur, CNRS, Artemis, F-06304 Nice, France*
[121]*University of British Columbia, Vancouver, BC V6T 1Z4, Canada*
[122]*Christopher Newport University, Newport News, VA 23606, USA*
[123]*OzGrav, University of Adelaide, Adelaide, South Australia 5005, Australia*
[124]*Centre national de la recherche scientifique, 75016 Paris, France*
[125]*Univ Rennes, CNRS, Institut FOTON - UMR 6082, F-35000 Rennes, France*
[126]*University of Birmingham, Birmingham B15 2TT, United Kingdom*
[127]*DIFA- Alma Mater Studiorum Università di Bologna, Via Zamboni, 33 - 40126 Bologna, Italy*
[128]*Washington State University, Pullman, WA 99164, USA*
[129]*Cornell University, Ithaca, NY 14850, USA*
[130]*University of Rhode Island, Kingston, RI 02881, USA*
[131]*Laboratoire Kastler Brossel, Sorbonne Université, CNRS,*
ENS-Université PSL, Collège de France, F-75005 Paris, France
[132]*OzGrav, University of Melbourne, Parkville, Victoria 3010, Australia*
[133]*Astronomical Observatory, University of Warsaw, 00-478 Warsaw, Poland*
[134]*University of Maryland, College Park, MD 20742, USA*
[135]*Università degli Studi di Milano-Bicocca, I-20126 Milano, Italy*
[136]*INFN, Sezione di Milano-Bicocca, I-20126 Milano, Italy*
[137]*Université de Lyon, Université Claude Bernard Lyon 1,*
CNRS, Institut Lumière Matière, F-69622 Villeurbanne, France
[138]*IAC3–IEEC, Universitat de les Illes Balears, E-07122 Palma de Mallorca, Spain*
[139]*University of Chicago, Chicago, IL 60637, USA*
[140]*Institut de Física d'Altes Energies (IFAE), The Barcelona Institute of*
Science and Technology, Campus UAB, E-08193 Bellaterra (Barcelona), Spain
[141]*University of Arizona, Tucson, AZ 85721, USA*
[142]*INFN, Sezione di Napoli, Gruppo Collegato di Salerno, I-80126 Napoli, Italy*
[143]*University of Massachusetts Dartmouth, North Dartmouth, MA 02747, USA*
[144]*Faculty of Physics, University of Warsaw, Ludwika Pasteura 5, 02-093 Warszawa, Poland*
[145]*Istituto di Astrofisica e Planetologia Spaziali di Roma, 00133 Roma, Italy*
[146]*Departamento de Astronomía y Astrofísica, Universitat de València, E-46100 Burjassot, València, Spain*
[147]*Observatori Astronòmic, Universitat de València, E-46980 Paterna, València, Spain*
[148]*OzGrav, Swinburne University of Technology, Hawthorn VIC 3122, Australia*
[149]*Niels Bohr Institute, University of Copenhagen, 2100 Kóbenhavn, Denmark*
[150]*National Central University, Taoyuan City 320317, Taiwan*
[151]*OzGrav, Charles Sturt University, Wagga Wagga, New South Wales 2678, Australia*
[152]*Vanderbilt University, Nashville, TN 37235, USA*
[153]*University of Chinese Academy of Sciences / International Centre for Theoretical Physics Asia-Pacific, Bejing 100190, China*
[154]*Institute of Physics, National Yang Ming Chiao Tung University, 101 Univ. Street, Hsinchu, Taiwan*
[155]*Kamioka Branch, National Astronomical Observatory of Japan,*
238 Higashi-Mozumi, Kamioka-cho, Hida City, Gifu 506-1205, Japan
[156]*National Tsing Hua University, Hsinchu City 30013, Taiwan*
[157]*University of Texas, Austin, TX 78712, USA*
[158]*CaRT, California Institute of Technology, Pasadena, CA 91125, USA*
[159]*Dipartimento di Ingegneria Industriale (DIIN), Università di Salerno, I-84084 Fisciano, Salerno, Italy*
[160]*Faculty of Science, University of Toyama, 3190 Gofuku, Toyama City, Toyama 930-8555, Japan*
[161]*School of Physical Science and Technology, ShanghaiTech University,*
393 Middle Huaxia Road, Pudong, Shanghai, 201210, China
[162]*Carleton College, Northfield, MN 55057, USA*
[163]*University of Szeged, Dóm tér 9, Szeged 6720, Hungary*
[164]*INFN Cagliari, Physics Department, Università degli Studi di Cagliari, Cagliari 09042, Italy*
[165]*Université Libre de Bruxelles, Brussels 1050, Belgium*
[166]*INAF, Osservatorio Astronomico di Brera sede di Merate, I-23807 Merate, Lecco, Italy*
[167]*Departamento de Matemáticas, Universitat de València, E-46100 Burjassot, València, Spain*
[168]*Montana State University, Bozeman, MT 59717, USA*
[169]*The University of Utah, Salt Lake City, UT 84112, USA*
[170]*Johns Hopkins University, Baltimore, MD 21218, USA*
[171]*The University of Texas Rio Grande Valley, Brownsville, TX 78520, USA*
[172]*Université de Liège, B-4000 Liège, Belgium*
[173]*University of Manitoba, Winnipeg, MB R3T 2N2, Canada*
[174]*INAF, Osservatorio di Astrofisica e Scienza dello Spazio, I-40129 Bologna, Italy*
[175]*INFN-CNAF - Bologna, Viale Carlo Berti Pichat, 6/2, 40127 Bologna BO, Italy*
[176]*Colorado State University, Fort Collins, CO 80523, USA*

[177]*Université de Normandie, ENSICAEN, UNICAEN, CNRS/IN2P3, LPC Caen, F-14000 Caen, France*
[178]*Laboratoire de Physique Corpusculaire Caen, 6 boulevard du maréchal Juin, F-14050 Caen, France*
[179]*The University of Sheffield, Sheffield S10 2TN, United Kingdom*
[180]*Université Claude Bernard Lyon 1, CNRS, Laboratoire des Matériaux Avancés (LMA), IP2I Lyon / IN2P3, UMR 5822, F-69622 Villeurbanne, France*
[181]*Western Washington University, Bellingham, WA 98225, USA*
[182]*Università di Firenze, Sesto Fiorentino I-50019, Italy*
[183]*IGFAE, Universidade de Santiago de Compostela, E-15782 Santiago de Compostela, Spain*
[184]*Dipartimento di Scienze Matematiche, Fisiche e Informatiche, Università di Parma, I-43124 Parma, Italy*
[185]*INFN, Sezione di Milano Bicocca, Gruppo Collegato di Parma, I-43124 Parma, Italy*
[186]*Marquette University, Milwaukee, WI 53233, USA*
[187]*Perimeter Institute, Waterloo, ON N2L 2Y5, Canada*
[188]*Scuola Normale Superiore, I-56126 Pisa, Italy*
[189]*Corps des Mines, Mines Paris, Université PSL, 60 Bd Saint-Michel, 75272 Paris, France*
[190]*Dipartimento di Fisica, Università di Trieste, I-34127 Trieste, Italy*
[191]*Université Côte d'Azur, Observatoire de la Côte d'Azur, CNRS, Lagrange, F-06304 Nice, France*
[192]*National Center for Nuclear Research, 05-400 Świerk-Otwock, Poland*
[193]*Università degli Studi di Sassari, I-07100 Sassari, Italy*
[194]*Vrije Universiteit Brussel, 1050 Brussel, Belgium*
[195]*University of Zurich, Winterthurerstrasse 190, 8057 Zurich, Switzerland*
[196]*Canadian Institute for Theoretical Astrophysics, University of Toronto, Toronto, ON M5S 3H8, Canada*
[197]*Stony Brook University, Stony Brook, NY 11794, USA*
[198]*Center for Computational Astrophysics, Flatiron Institute, New York, NY 10010, USA*
[199]*Montclair State University, Montclair, NJ 07043, USA*
[200]*HUN-REN Institute for Nuclear Research, H-4026 Debrecen, Hungary*
[201]*Indian Institute of Technology Bombay, Powai, Mumbai 400 076, India*
[202]*Centro de Física das Universidades do Minho e do Porto, Universidade do Minho, PT-4710-057 Braga, Portugal*
[203]*Aix Marseille Univ, CNRS/IN2P3, CPPM, Marseille, France*
[204]*CNR-SPIN, I-84084 Fisciano, Salerno, Italy*
[205]*Dipartimento di Ingegneria, Università della Basilicata, I-85100 Potenza, Italy*
[206]*SUPA, University of the West of Scotland, Paisley PA1 2BE, United Kingdom*
[207]*Barry University, Miami Shores, FL 33168, USA*
[208]*Eötvös University, Budapest 1117, Hungary*
[209]*Institute for Cosmic Ray Research, KAGRA Observatory, The University of Tokyo, 5-1-5 Kashiwa-no-Ha, Kashiwa City, Chiba 277-8582, Japan*
[210]*Department of Physics, Graduate School of Science, Osaka Metropolitan University, 3-3-138 Sugimoto-cho, Sumiyoshi-ku, Osaka City, Osaka 558-8585, Japan*
[211]*University of Sannio at Benevento, I-82100 Benevento, Italy and INFN, Sezione di Napoli, I-80100 Napoli, Italy*
[212]*California State University, Los Angeles, Los Angeles, CA 90032, USA*
[213]*Instituto de Fisica Teorica UAM-CSIC, Universidad Autonoma de Madrid, 28049 Madrid, Spain*
[214]*Istituto Nazionale di Astrofisica - Osservatorio di Roma, Viale del Parco Mellini 84 - 00136 Roma, Italy*
[215]*Laboratoire d'Acoustique de l'Université du Mans, UMR CNRS 6613, F-72085 Le Mans, France*
[216]*University of Southampton, Southampton SO17 1BJ, United Kingdom*
[217]*Dipartimento di Ingegneria Industriale, Elettronica e Meccanica, Università degli Studi Roma Tre, I-00146 Roma, Italy*
[218]*University of Nevada, Las Vegas, Las Vegas, NV 89154, USA*
[219]*University of Nottingham NG7 2RD, UK*
[220]*Ariel University, Ramat HaGolan St 65, Ari'el, Israel*
[221]*The University of Mississippi, University, MS 38677, USA*
[222]*Graduate School of Science, Institute of Science Tokyo, 2-12-1 Ookayama, Meguro-ku, Tokyo 152-8551, Japan*
[223]*Institute of Physics, Academia Sinica, 128 Sec. 2, Academia Rd., Nankang, Taipei 11529, Taiwan*
[224]*The Chinese University of Hong Kong, Shatin, NT, Hong Kong*
[225]*Nirula Institute of Technology, Kolkata, West Bengal 700109, India*
[226]*Niels Bohr Institute, Copenhagen University, 2100 København, Denmark*
[227]*American University, Washington, DC 20016, USA*
[228]*Dipartimento di Fisica, Università degli studi di Milano, Via Celoria 16, I-20133, Milano, Italy*
[229]*INFN, sezione di Milano, Via Celoria 16, I-20133, Milano, Italy*
[230]*Department of Applied Physics, Fukuoka University, 8-19-1 Nanakuma, Jonan, Fukuoka City, Fukuoka 814-0180, Japan*
[231]*University of Cambridge, Cambridge CB2 1TN, United Kingdom*
[232]*University of Lancaster, Lancaster LA1 4YW, United Kingdom*

[233]*College of Industrial Technology, Nihon University, 1-2-1 Izumi, Narashino City, Chiba 275-8575, Japan*
[234]*Faculty of Engineering, Niigata University, 8050 Ikarashi-2-no-cho, Nishi-ku, Niigata City, Niigata 950-2181, Japan*
[235]*Saha Institute of Nuclear Physics, Bidhannagar, West Bengal 700064, India*
[236]*Department of Physics, Tamkang University, No. 151,*
Yingzhuan Rd., Danshui Dist., New Taipei City 25137, Taiwan
[237]*Department of Electrophysics, National Yang Ming Chiao Tung University, 101 Univ. Street, Hsinchu, Taiwan*
[238]*Rutherford Appleton Laboratory, Didcot OX11 0DE, United Kingdom*
[239]*Department of Physical Sciences, Aoyama Gakuin University,*
5-10-1 Fuchinobe, Sagamihara City, Kanagawa 252-5258, Japan
[240]*Nagoya University, Nagoya, 464-8601, Japan*
[241]*Helmut Schmidt University, D-22043 Hamburg, Germany*
[242]*Nambu Yoichiro Institute of Theoretical and Experimental Physics (NITEP),*
Osaka Metropolitan University, 3-3-138 Sugimoto-cho, Sumiyoshi-ku, Osaka City, Osaka 558-8585, Japan
[243]*Directorate of Construction, Services & Estate Management, Mumbai 400094, India*
[244]*Observatoire Astronomique de Strasbourg, Université de Strasbourg,*
CNRS, 11 rue de l'Université, 67000 Strasbourg, France
[245]*Faculty of Physics, University of Białystok, 15-245 Białystok, Poland*
[246]*National Astronomical Observatories, Chinese Academy of Sciences, 20A Datun Road, Chaoyang District, Beijing, China*
[247]*School of Astronomy and Space Science, University of Chinese Academy of Sciences, 20A Datun Road, Chaoyang District, Beijing, China*
[248]*Sungkyunkwan University, Seoul 03063, Republic of Korea*
[249]*Department of Physics, Ulsan National Institute of Science and Technology (UNIST),*
50 UNIST-gil, Ulju-gun, Ulsan 44919, Republic of Korea
[250]*Chung-Ang University, Seoul 06974, Republic of Korea*
[251]*University of Washington Bothell, Bothell, WA 98011, USA*
[252]*Laboratoire de Physique et de Chimie de l'Environnement,*
Université Joseph KI-ZERBO, 9GH2+3V5, Ouagadougou, Burkina Faso
[253]*Ewha Womans University, Seoul 03760, Republic of Korea*
[254]*National Institute for Mathematical Sciences, Daejeon 34047, Republic of Korea*
[255]*Korea Astronomy and Space Science Institute, Daejeon 34055, Republic of Korea*
[256]*Department of Astronomy and Space Science, Chungnam National University,*
9 Daehak-ro, Yuseong-gu, Daejeon 34134, Republic of Korea
[257]*Division of Science, National Astronomical Observatory of Japan, 2-21-1 Osawa, Mitaka City, Tokyo 181-8588, Japan*
[258]*Department of Physics, Aristotle University of Thessaloniki, 54124 Thessaloniki, Greece*
[259]*Bard College, Annandale-On-Hudson, NY 12504, USA*
[260]*Technical University of Braunschweig, D-38106 Braunschweig, Germany*
[261]*Institute of Mathematics, Polish Academy of Sciences, 00656 Warsaw, Poland*
[262]*Astronomical Observatory, Jagiellonian University, 31-007 Cracow, Poland*
[263]*Department of Physics and Astronomy, University of Padova, Via Marzolo, 8-35151 Padova, Italy*
[264]*Sezione di Padova, Istituto Nazionale di Fisica Nucleare (INFN), Via Marzolo, 8-35131 Padova, Italy*
[265]*Instituto de Fisica Teorica UAM-CSIC, Universidad Autonoma de Madrid, 28049 Madrid, Spain*
[266]*Department of Physics, Nagoya University, ES building, Furocho, Chikusa-ku, Nagoya, Aichi 464-8602, Japan*
[267]*Université de Montréal/Polytechnique, Montreal, Quebec H3T 1J4, Canada*
[268]*Università degli Studi di Cagliari, Via Università 40, 09124 Cagliari, Italy*
[269]*Department of Computer Simulation, Inje University,*
197 Inje-ro, Gimhae, Gyeongsangnam-do 50834, Republic of Korea
[270]*Korea Astronomy and Space Science Institute (KASI),*
776 Daedeokdae-ro, Yuseong-gu, Daejeon 34055, Republic of Korea
[271]*NAVIER, École des Ponts, Univ Gustave Eiffel, CNRS, Marne-la-Vallée, France*
[272]*Gravitational Wave Science Project, National Astronomical Observatory of Japan (NAOJ), Mitaka City, Tokyo 181-8588, Japan*
[273]*Department of Physics, National Cheng Kung University, No.1, University Road, Tainan City 701, Taiwan*
[274]*St. Thomas University, Miami Gardens, FL 33054, USA*
[275]*Institució Catalana de Recerca i Estudis Avançats, E-08010 Barcelona, Spain*
[276]*Institut de Física d'Altes Energies, E-08193 Barcelona, Spain*
[277]*Institut fuer Theoretische Astrophysik, Zentrum fuer Astronomie Heidelberg,*
Universitaet Heidelberg, Albert Ueberle Str. 2, 69120 Heidelberg, Germany
[278]*Institucio Catalana de Recerca i Estudis Avançats (ICREA),*
Passeig de Lluís Companys, 23, 08010 Barcelona, Spain
[279]*Research Center for Space Science, Advanced Research Laboratories, Tokyo City University,*
3-3-1 Ushikubo-Nishi, Tsuzuki-Ku, Yokohama, Kanagawa 224-8551, Japan
[280]*Tsinghua University, Beijing 100084, China*
[281]*Universidad de Guadalajara, 44430 Guadalajara, Jalisco, Mexico*
[282]*Institut des Hautes Etudes Scientifiques, F-91440 Bures-sur-Yvette, France*
[283]*Faculty of Law, Ryukoku University, 67 Fukakusa Tsukamoto-cho, Fushimi-ku, Kyoto City, Kyoto 612-8577, Japan*
[284]*Istituto Nazionale di Fisica Nucleare (INFN), Universita di Roma "La Sapienza", P.le A. Moro 2, 00185 Roma, Italy*

[285]*Indian Institute of Science Education and Research, Kolkata, Mohanpur, West Bengal 741252, India*
[286]*Phenikaa Institute for Advanced Study (PIAS), Phenikaa University, Yen Nghia, Ha Dong, Hanoi, Vietnam*
[287]*University of Stavanger, 4021 Stavanger, Norway*
[288]*Department of Astronomy, The University of Tokyo, 7-3-1 Hongo, Bunkyo-ku, Tokyo 113-0033, Japan*
[289]*Physics Program, Graduate School of Advanced Science and Engineering, Hiroshima University, 1-3-1 Kagamiyama, Higashihiroshima City, Hiroshima 739-8526, Japan*
[290]*GRAPPA, Anton Pannekoek Institute for Astronomy and Institute for High-Energy Physics, University of Amsterdam, 1098 XH Amsterdam, Netherlands*
[291]*University College London, London WC1E 6BT, United Kingdom*
[292]*Observatoire de Paris, 75014 Paris, France*
[293]*Graduate School of Science and Technology, Niigata University, 8050 Ikarashi-2-no-cho, Nishi-ku, Niigata City, Niigata 950-2181, Japan*
[294]*Niigata Study Center, The Open University of Japan, 754 Ichibancho, Asahimachi-dori, Chuo-ku, Niigata City, Niigata 951-8122, Japan*
[295]*CSIR-Central Glass and Ceramic Research Institute, Kolkata, West Bengal 700032, India*
[296]*Consiglio Nazionale delle Ricerche - Istituto dei Sistemi Complessi, I-00185 Roma, Italy*
[297]*Department of Astronomy, Yonsei University, 50 Yonsei-Ro, Seodaemun-Gu, Seoul 03722, Republic of Korea*
[298]*Department of Physics, University of Guadalajara, Av. Revolucion 1500, Colonia Olimpica C.P. 44430, Guadalajara, Jalisco, Mexico*
[299]*Hobart and William Smith Colleges, Geneva, NY 14456, USA*
[300]*INAF, Osservatorio Astronomico di Padova, I-35122 Padova, Italy*
[301]*Dipartimento di Ingegneria, Università del Sannio, I-82100 Benevento, Italy*
[302]*Institut d'Astrophysique de Paris, Sorbonne Université, CNRS, UMR 7095, 75014 Paris, France*
[303]*Museo Storico della Fisica e Centro Studi e Ricerche "Enrico Fermi", I-00184 Roma, Italy*
[304]*Kennesaw State University, Kennesaw, GA 30144, USA*
[305]*Government Victoria College, Palakkad, Kerala 678001, India*
[306]*Subatech, CNRS/IN2P3 - IMT Atlantique - Nantes Université, 4 rue Alfred Kastler BP 20722 44307 Nantes CÉDEX 03, France*
[307]*Universidad de Antioquia, Medellín, Colombia*
[308]*Departamento de Física - ETSIDI, Universidad Politécnica de Madrid, 28012 Madrid, Spain*
[309]*Department of Electronic Control Engineering, National Institute of Technology, Nagaoka College, 888 Nishikatakai, Nagaoka City, Niigata 940-8532, Japan*
[310]*Trinity College, Hartford, CT 06106, USA*
[311]*Dipartimento di Fisica e Scienze della Terra, Università Degli Studi di Ferrara, Via Saragat, 1, 44121 Ferrara FE, Italy*
[312]*Faculty of Science, Toho University, 2-2-1 Miyama, Funabashi City, Chiba 274-8510, Japan*
[313]*Indian Institute of Technology, Palaj, Gandhinagar, Gujarat 382355, India*
[314]*Seoul National University, Seoul 08826, Republic of Korea*
[315]*Kavli Institute for Astronomy and Astrophysics, Peking University, Yiheyuan Road 5, Haidian District, Beijing 100871, China*
[316]*Laboratoire MSME, Cité Descartes, 5 Boulevard Descartes, Champs-sur-Marne, 77454 Marne-la-Vallée Cedex 2, France*
[317]*Faculty of Information Science and Technology, Osaka Institute of Technology, 1-79-1 Kitayama, Hirakata City, Osaka 573-0196, Japan*
[318]*NASA Goddard Space Flight Center, Greenbelt, MD 20771, USA*
[319]*Faculty of Science and Technology, Kochi University, 2-5-1 Akebono-cho, Kochi-shi, Kochi 780-8520, Japan*
[320]*Laboratoire de Physique de l'École Normale Supérieure, ENS, (CNRS, Université PSL, Sorbonne Université, Université Paris Cité), F-75005 Paris, France*
[321]*The Hakubi Center for Advanced Research, Kyoto University, Yoshida-honmachi, Sakyou-ku, Kyoto City, Kyoto 606-8501, Japan*
[322]*Department of Physics, Kyoto University, Kita-Shirakawa Oiwake-cho, Sakyou-ku, Kyoto City, Kyoto 606-8502, Japan*
[323]*Yukawa Institute for Theoretical Physics (YITP), Kyoto University, Kita-Shirakawa Oiwake-cho, Sakyou-ku, Kyoto City, Kyoto 606-8502, Japan*
[324]*University of Catania, Department of Physics and Astronomy, Via S. Sofia, 64, 95123 Catania CT, Italy*
[325]*National Institute of Technology, Fukui College, Geshi-cho, Sabae-shi, Fukui 916-8507, Japan*
[326]*Department of Communications Engineering, National Defense Academy of Japan, 1-10-20 Hashirimizu, Yokosuka City, Kanagawa 239-8686, Japan*
[327]*Eindhoven University of Technology, 5600 MB Eindhoven, Netherlands*
[328]*Concordia University Wisconsin, Mequon, WI 53097, USA*
[329]*Kavli Institute for the Physics and Mathematics of the Universe (Kavli IPMU), WPI, The University of Tokyo, 5-1-5 Kashiwa-no-Ha, Kashiwa City, Chiba 277-8583, Japan*
[330]*Department of Astronomy, Beijing Normal University, Xinjiekouwai Street 19, Haidian District, Beijing 100875, China*

[331]*School of Physics and Technology, Wuhan University,*
Bayi Road 299, Wuchang District, Wuhan, Hubei, 430072, China
(Dated: May 7, 2026)

GW240925 and GW250207 are two loud gravitational-wave signals from binary black hole coalescences observed with network signal-to-noise ratios ∼ 32 and ∼ 69, respectively, by the LIGO Hanford–LIGO Livingston–Virgo network. Gravitational-wave signals from coalescing binaries have characteristic phase and amplitude evolution predicted by general relativity. These signal waveforms, together with measured instrumental calibration uncertainties, are used to infer source parameters. However, for sufficiently loud detections it is possible to constrain the calibration of the detectors directly using the signals themselves. We present the first informative astrophysical measurements of gravitational-wave detector calibration. For GW240925, we verify the inference of Hanford calibration from the astrophysical signal through cross-checks with known calibration errors obtained from in-situ measurements. At the time of GW250207, the Hanford detector was not fully stabilized, leading to elevated calibration uncertainties; thus, astrophysical calibration is essential to obtain accurate data and to enable source localization. These well-localized, high signal-to-noise observations have the potential to offer precise measurements of source properties, stringent tests of general relativity, and informative dark siren measurements, provided that calibration uncertainties are properly incorporated. As detector sensitivity improves, astrophysical calibration will become an increasingly valuable complement to in-situ calibration measurements. Obtaining accurate calibration will be essential for precision gravitational-wave science.

Introduction— We report the discovery of GW240925_005809 and GW250207_115645 (hereafter, GW240925 and GW250207), two loud gravitational-wave (GW) signals detected by the Laser Interferometer Gravitational-Wave Observatory (LIGO) Hanford, LIGO Livingston and Virgo during their fourth observing run (O4). Since the first direct observation of GWs in 2015 [1], the LIGO–Virgo–KAGRA (LVK) network [2–4] has undergone substantial upgrades, achieving a roughly tenfold increase in detection rate and facilitating high signal-to-noise ratio (SNR) observations of compact binary coalescences (CBCs) [5–10]. These advances mark a transition from an era of initial discoveries to one of precision GW astronomy. High-SNR observations enable precise measurements of signal properties [11–13], advancing our understanding of source astrophysics, the nature of gravity, and cosmology.

Interpreting GW signals requires accurate understanding of detector behavior [13]. GW240925 and GW250207 both coincide with times where the LIGO Hanford detector was not in its usual observational state with well-characterized calibration. The calibration process typically reconstructs the raw digitized output of each interferometer into an accurate and reliable measure of the dimensionless strain [14–17]. Its accuracy directly impacts signal-parameter estimation [18, 19]; miscalibrations can bias inferred source properties [20, 21], affect cosmological measurements [22] and even mimic or obscure deviations from general relativity (GR) [23, 24]. To take advantage of the small statistical uncertainties offered by high SNRs, we must ensure small systematic uncertainties.

Fortunately, GW signals can be used to constrain the detector response directly. This *astrophysical* calibration approach leverages accurate modeling of GW waveforms, allowing the astrophysical signal to serve as an independent reference for the frequency-dependent detector calibration [5, 25, 26]. Astrophysical calibration may be performed in a variety of ways: using the frequency and amplitude evolution of the (predicted) signal to infer calibration parameters together with source parameters [26–28]; using an electromagnetic counterpart (and assumed cosmology) to establish the distance to a source [29], which provides more information than using the GW signal alone [26]; combining data from multiple detectors so the signals should cancel out if the data are correctly calibrated [30], or using the population of detections to constrain the relative sensitivity of the detectors [31]. The sensitivity of the first years of observations was insufficient for astrophysical measurements to be informative compared to in-situ results [26–28], but with the improvements of the detector network, astrophysical calibration is now becoming feasible.

We present the first astrophysical calibrations of a GW detector used to enhance our understanding of the state of the instrument. We perform a coherent analysis of data from Hanford, Livingston and Virgo for GW240925 and GW250207, inferring calibration properties for Hanford at the times of the two observations using the GW signals.

For GW240925, there was a significant frequency-dependent calibration systematic error for Hanford at the time of the observation. The frequency-dependent error can be inferred using the signal, and cross-checked with the in-situ measurements. Agreement between results validates the GW-informed calibration measurements and demonstrates the utility of inferring calibration from an astrophysical signal.

At the time of GW250207, the Hanford detector response had not yet fully stabilized, leading to larger calibration uncertainties. Lacking in-situ measurements of the calibration, astrophysical calibration was essential to ensure the reliability of the Hanford data and accurate inference of source properties such as localization.

These results establish astrophysical calibration as a complementary cross-check and, when required, a critical input to GW analysis. While not yet as precise as typical in-situ measurements, astrophysical calibration will improve as detector sensitivity continues to be enhanced.

Detector calibration— GW detectors like LIGO [2], Virgo [3] and KAGRA [4] are enhanced Michelson interfer-

ometers that measure spacetime strain by detecting changes in light-travel time between their orthogonal arms [32, 33]. The detector output strain data d are defined as the free (uncontrolled) differential change in arm length $\Delta L_{\rm free}$ divided by arm length L, i.e., $d \equiv \Delta L_{\rm free}/L$; however, $\Delta L_{\rm free}$ is not directly measurable, as the detector actively suppresses differential motion via feedback control. A detailed *calibration* procedure is therefore required to convert the raw digitized electrical output of the detector into the reconstructed strain data [14–16, 34, 35].

To reconstruct the strain, we need the frequency-dependent and time-varying detector response function $R(f;t)$ (detailed in the Supplemental Material); however, in the calibration procedure, the true response function is not perfectly known. The strain data are reconstructed using a *modeled* response function $R^{(\rm model)}(f;t)$ [14–16]. Calibration systematic errors arise from discrepancies between the true and modeled response functions; these errors and associated statistical uncertainties directly translate into the errors and uncertainties in the reconstructed d. In the absence of configuration changes (which are typically associated with updates to $R^{(\rm model)}$), $R(f;t)$ remains approximately stable, but can vary on hour timescales during periods of evolving detector state, e.g., at the beginning of a lock stretch (see discussion of thermal lens below) [36]. For LIGO, we quantify calibration errors using a complex correction factor $\eta(f;t)$ [16, 37]:

$$\eta(f;t) = \frac{R(f;t)}{R^{(\rm model)}(f;t)} = \left[1 + \delta\mathcal{A}(f;t)\right] \exp\left[i\delta\phi(f;t)\right], \quad (1)$$

where $\delta\mathcal{A}(f;t)$ and $\delta\phi(f;t)$ denote amplitude and phase errors, respectively. A more accurate estimate of the true strain is obtained by multiplying the (frequency-domain) detector strain data by the correction factor η,

$$d^{(\rm corr)} = \eta d. \quad (2)$$

The probability distribution of $\eta(f;t)$ is evaluated using in-situ calibration measurements, primarily through excitations via photon calibrators [38–41] and quadruple-pendulum actuators [16, 42], and is used to construct the calibration prior for signal parameter estimation [43] (see Supplemental Material).

The low-latency, online calibrated (C00) strain data produced during observing runs may contain systematic errors due to model inaccuracies that are not identified or corrected in real time. In previous observing runs, offline calibrated data (C01) were produced for the LIGO detectors as the standard final data product, incorporating all known corrections [14–16]. In O4, the photon calibrators were used to monitor the calibration accuracy at a discrete set of frequencies in real time [17, 42], and C01 data were generated when necessary, e.g., when the calibration error was known to exceed $\sim 10\%$ in amplitude or ~ 10 deg in phase (68% probability).

At the times of GW240925 and GW250207, Livingston and Virgo were observing normally, but the Hanford detector was either miscalibrated or still stabilizing, with a response deviating from the modeled behavior. KAGRA was not observing over this period of O4 [5]. Detailed real-time calibration monitoring measurements [42] at the Hanford detector around the times of these two observations are provided in the Supplemental Material. The Livingston and Virgo detectors had reliable calibration: in the most sensitive frequency band 20–2000 Hz, their frequency-dependent uncertainties (68% probability) were constrained to $\lesssim 2\%$ in amplitude and $\lesssim 2$ deg in phase for Livingston, and $\lesssim 2.5\%$ in amplitude and $\lesssim 6$ deg ($\lesssim 3$ deg below 500 Hz) in phase for Virgo [44].

For GW240925, a procedural inconsistency at Hanford resulted in a temporary mismatch between a calibration parameter used in the interferometer control system and the corresponding value adopted in the calibration model. The mismatch led to a mischaracterization of the detector response, introducing a frequency-dependent systematic error in the reconstructed strain data. The error reached up to $\sim 20\%$ in amplitude and ~ 12 deg in phase across the sensitive frequency band [45]. This large error in the C00 calibration, combined with GW240925's high SNR, provided a unique opportunity to cross-check signal-informed astrophysical calibration with in-situ measurements. C01 data were later generated around the time of GW240925, correcting the miscalibration.

For GW250207, the Hanford detector had just reached its low-noise operational state but had not yet formally entered observing mode [45]. The detector was still settling; in particular, the changing thermal lens of the test masses affected the low-frequency response [10]. While real-time calibration monitoring can provide valuable information about the evolution of systematic errors during such transient periods [42], the monitoring lines had not yet stabilized, and several were not yet recording measurements. As a result, no reliable measurement of the real-time detector response is available for this period, and the associated calibration systematic errors and uncertainties in the Hanford strain data cannot be robustly quantified using in-situ measurements. Astrophysical calibration is essential to analyze Hanford data.

Detection— GW240925 and GW250207 were observed by the three-detector Hanford–Livingston–Virgo network. Time–frequency spectrograms of the data around the two signals are shown in Fig. 1. The characteristic chirps of CBC signals are visible sweeping up from low frequencies.

GW240925 was observed at 00:58:09 Coordinated Universal Time (UTC) on September 25, 2024 during the second part of O4 (O4b). It was identified in low latency in Hanford and Livingston data by the minimally modeled cWB [47–50] pipeline as well as the GstLAL [51–59], MBTA [60–62] and SPIIR [63] matched-filtering pipelines. The candidate was identified with SNRs of 17.3 and 25.8 in Hanford and Livingston, respectively, and a false alarm rate (FAR) of $< 1 \times 10^{-5}\ \mathrm{yr}^{-1}$. The Virgo detector was operating at the time, but the candidate's SNR of 2.7 was too small to contribute to the coincident detection. Nevertheless, the Virgo SNR time series was analyzed by BAYESTAR [64, 65] to infer the location. General Coordinate Network (GCN) Notices and Circu-

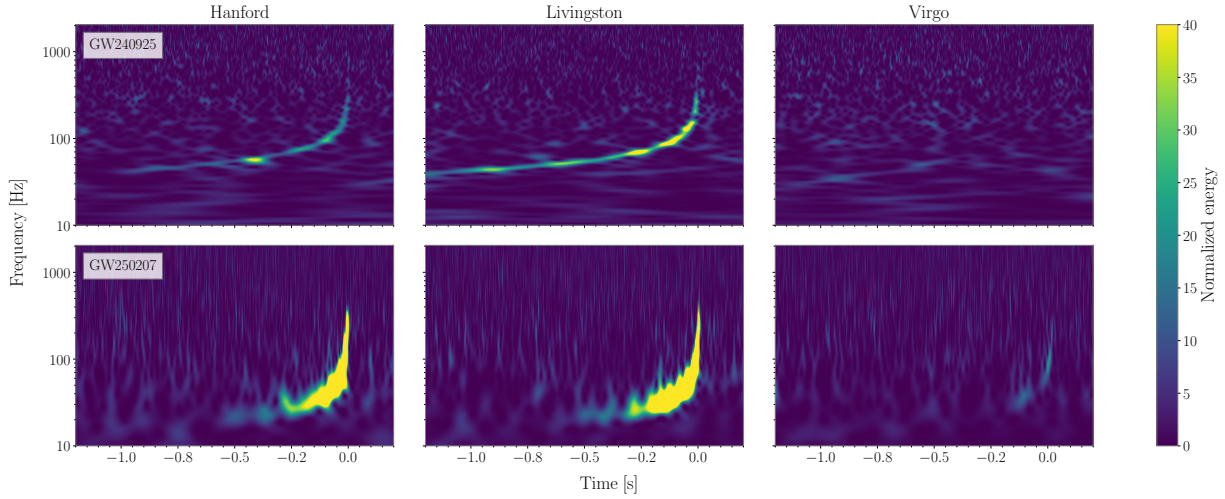

FIG. 1. Time–frequency spectrograms [46] showing data from LIGO Hanford (left), LIGO Livingston (middle) and Virgo (right) for GW240925 (top) and GW250207 (bottom). Times are relative to the times reported from the search algorithms for the two detections. We use C00 LIGO data. The data are whitened [13], and the scale bar shows the normalized energy.

lars about the detection were shared in low latency.[1]

Data quality (DQ) was scrutinized around GW240925 following established procedures [66]. We identified a burst of non-Gaussian noise (a *glitch* [67, 68]) in Livingston data, but this occurred sufficiently after the signal to not require mitigation [69]. No DQ issues impacting the analysis were found.

GW250207 was observed at 11:56:45 UTC on February 7, 2025 during the third part of O4 (O4c). It was identified in low latency in Livingston and Virgo data by the GstLAL and SPIIR search pipelines. The signal was measured with SNRs of 48.3 and 8.1 in the Livingston and Virgo detectors, respectively, and a FAR of $< 1 \times 10^{-5}$ yr^{-1}. DQ checks [66] revealed no issues impacting the detection. As Hanford was not in observing mode, its data were not used in low-latency, but were later determined to be of good quality [45]. GCN Notices and Circulars were again shared in low latency.[2]

Further DQ and search-analysis results for both detections are given in the Supplemental Material.

Inference of calibration errors and source properties— We analyze the detector data for each signal using Bilby [70, 71] to obtain posterior probability distributions on the parameters $\boldsymbol{\theta}$ characterizing the source binary and those describing the calibration of each detector [43]. We assume that a GR waveform $h(\boldsymbol{\theta})$ accurately describes the signal. To account for calibration uncertainty, the reciprocal of the correction factor $(1/\eta)$ is applied to the waveform. This reciprocal factor is parametrized using amplitude and phase deviations, derived from their counterparts in Eq. (1) [43, 72], which are modeled using splines and inferred from the data [43, 73, 74]. Further details on inferences are given in the Supplemental Material.

The consistency of the signal across frequencies and between detectors provides information about the detector calibration. Typically, we use the in-situ measured calibration-uncertainty estimates from the time closest to the signal as priors in the analysis. As these are usually well constrained, the GW signal adds little information [6, 26]. However, for higher SNR signals or cases where calibration errors are significant, astrophysical calibration is expected to become informative.

We first demonstrate the measurement of the Hanford calibration error with GW240925, performing three analyses. For each, we use the usual calibration priors informed by in-situ measurements for Livingston and Virgo. We analyze LIGO C00 data, which contains the large Hanford calibration error, assuming two different priors for the Hanford calibration: one narrow, informed by in-situ measurements, and one wide across all frequencies. As the cause of the calibration error can be identified, we can directly compare the in-situ measured calibration error to the calibration independently inferred from the signal. We also analyze LIGO C01 data, where the calibration error has been corrected, assuming a narrow in-situ calibration prior.

In Fig. 2 (left), we plot the Hanford calibration parameters for GW240925 as a function of frequency. With the wide prior, the posterior provides the tightest constraints at frequencies where the signal is loud (below the peak of the dominant $\ell = |m| = 2$ multipole at a frequency $f_{22}^{\rm peak}$ of $\sim$ 680 Hz), and tends towards the prior at higher frequencies where there is no signal to constrain the calibration (the oscillations reflect the discrete placement of spline nodes). To quantify the difference between the wide prior and the corresponding posterior, we use the Jensen–Shannon divergences (JSDs) [75] between the distributions, finding $0.06^{+0.09}_{-0.05}$ nat for amplitude and $0.05^{+0.13}_{-0.05}$ nat for phase, quoting the median and 90% range across the frequency nodes, where JSD $\lesssim 0.002$ nat is consid-

[1] GCN Circular archive for S240925n.
[2] GCN Circular archive for S250207bg.

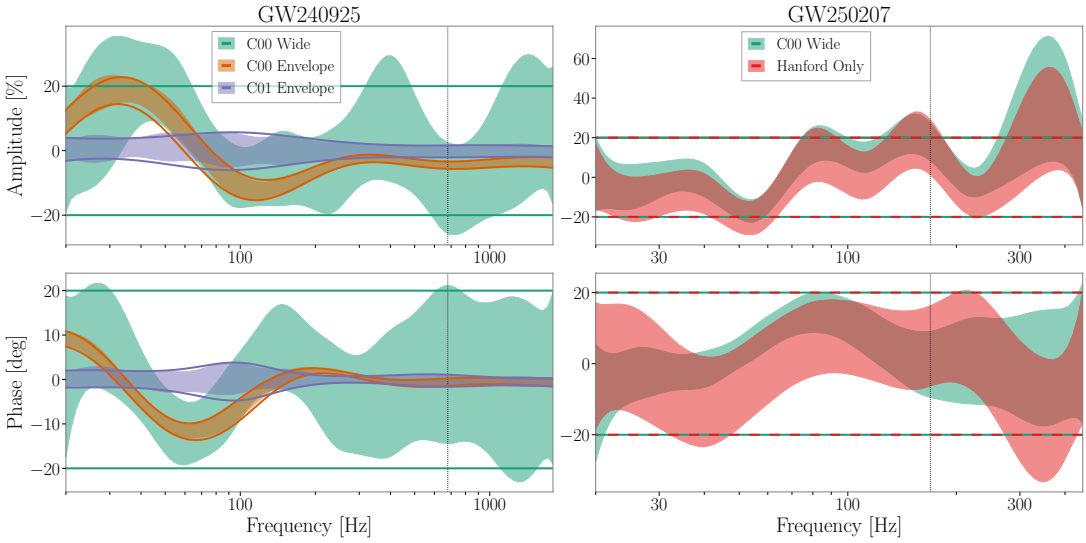

FIG. 2. LIGO Hanford calibration as a function of frequency over the analysis band for each signal. The top and bottom panels show the frequency-dependent amplitude error $\delta\mathcal{A}$, and phase error $\delta\phi$, respectively. Shaded regions indicate the 68% credible intervals of the posteriors, and the lines denote the 68% probability envelopes from which the priors are derived (see Supplemental Material). GW240925 results (left) are from three analyses: one using a wide, uninformative prior on the miscalibrated C00 data (green), one using a narrow prior envelope based upon in-situ measurements on the same data (orange), and one using a narrow in-situ measured prior envelope for the recalibrated C01 data (purple). GW250207 results (right) are from two analyses, both using the same wide priors on the miscalibrated Hanford C00 data: one using data from all three detectors (green), with the in-situ priors applied to Livingston and Virgo data, and one using only Hanford data (red). Results are more informative for frequencies where there is more signal power (Fig. 1), and the dotted vertical lines indicate the approximate peak frequencies $f_{22}^{\rm peak}$ for the $\ell = |m| = 2$ multipole of the signals.

ered a negligible difference [71]. This indicates that the posterior is informed by the signal at various frequencies. The posterior obtained with the wide, uninformative prior agrees well with the results informed by the in-situ measurements, demonstrating that detector calibration can be inferred from an astrophysical signal. Although the signal-informed calibration is less constrained than the in-situ measurements, it provides an independent cross-check and a valuable diagnostic for uncovering analysis inconsistencies. In this case, the direct comparison between constraints revealed (and led to the correction of) a long-standing convention mismatch in the analysis procedure for incorporating calibration uncertainties, which had only had a minor effect prior to O4 [43, 72]. Results from the C01 data for both LIGO detectors and Virgo are consistent with zero error, as expected after calibration correction.

We find that inferred source parameters are typically consistent between analyses. We adopt the C01 results as our default for interpretation, with medians and 90% symmetric credible intervals for the parameters listed in Table I.

The sky localization is illustrated in Fig. 3. Calibration uncertainty can have a significant impact on source localization [20, 27, 76], and using the wider calibration prior increases the localization area. Also shown in Fig. 3 is a medium-latency localization [77]; this did not use Hanford data because of the miscalibration. To leading order, the sky localization depends upon the time delay observed between detectors, and adding a third detector enables triangulation of the source [78–80]. The inclusion of the Hanford data significantly changes the inferred localization (the 90% localization volume shrinks from $\sim 1 \times 10^7$ Mpc^3 to $\sim 2 \times 10^5$ Mpc^3), as further discussed in the Supplemental Material, demonstrating the importance of using data from all detectors.

GW240925's source is inferred to be a low-mass binary black hole (BBH). The binary has a total mass of $M = 16.1^{+0.7}_{-0.4} M_\odot$ (median and 90% symmetric credible interval) and has support for equal-mass components, with mass ratio $q > 0.57$ (90% probability). The masses are consistent with the peak of the BBH mass distribution [83] and the masses of black holes in X-ray binaries [84–89]. The source is inferred to not have high spins ($\chi_1 < 0.53$ and $\chi_2 < 0.69$); the effective inspiral spin $\chi_{\rm eff}$ [90, 91] is small ($|\chi_{\rm eff}| < 0.08$), with positive values preferred, indicating a probable net alignment of the component spins with the orbital angular momentum.

Having demonstrated the efficacy of astrophysical calibration with GW240925, we turn to GW250207, where we must rely on signal-based inference to constrain the Hanford calibration. We analyze the C00 data using a wide prior across all frequencies for the Hanford calibration parameters, and in-situ measured priors for Livingston and Virgo. For comparison we also perform (i) an analysis using only Hanford data, to show what can be inferred without constraints from other detectors, and (ii) an analysis assuming that the data from all three detectors are perfectly calibrated, to investigate the impact of neglecting calibration uncertainties.

The results in Fig. 2 (right) show that the astrophysical cal-

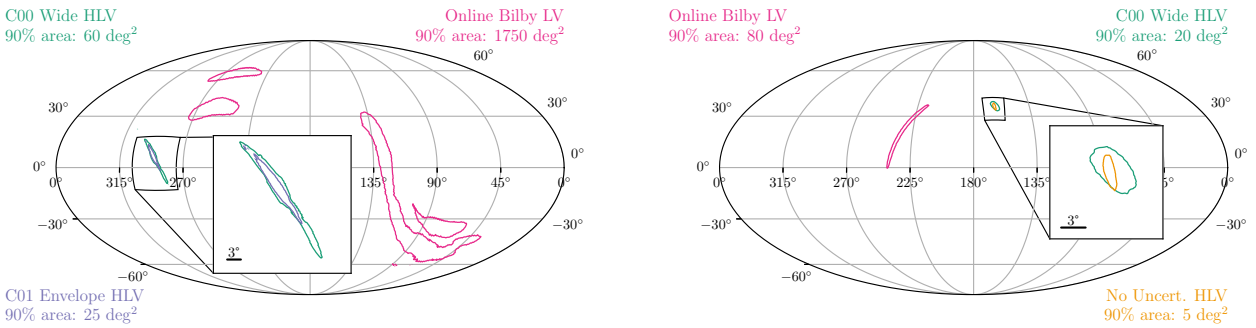

FIG. 3. Sky localization for GW240925 (left) and GW250207 (right) from analyses using data from all three detectors (HLV) and just Livingston and Virgo (LV). The contours show 90% credible areas. We show results using the wide calibration prior for Hanford (green), plus the result using the in-situ measured prior for GW240925 (purple) and the result neglecting calibration uncertainty for GW250207 (yellow). The medium-latency Online Bilby (magenta) analyses only used Livingston and Virgo data for both signals [77, 82]. Inclusion of the Hanford data, enabled by the simultaneous estimation of the calibration parameters, has a significant impact on both localizations.

TABLE I. Inferred source properties [5] for GW240925 and GW250207. We report median values with 90% symmetric credible intervals. GW240925 results use C01 data and calibration uncertainties based upon in-situ measurements. GW250207 results use a wide prior for the Hanford calibration uncertainty, and a prior based upon in-situ measurements for Livingston and Virgo calibration. Quantities that evolve throughout the inspiral are quoted at a reference frequency of 20 Hz. Results are computed assuming a standard cosmology with $H_0 = 67.9\,\mathrm{km\,s^{-1}\,Mpc^{-1}}$ [43, 81].

Parameter	GW240925	GW250207
Primary mass $m_1/M_\odot$	$9.0^{+2.0}_{-1.0}$	$35.2^{+1.7}_{-1.7}$
Secondary mass $m_2/M_\odot$	$7.0^{+0.8}_{-1.3}$	$30.6^{+1.5}_{-1.8}$
Total mass $M/M_\odot$	$16.1^{+0.7}_{-0.4}$	$65.9^{+1.0}_{-1.7}$
Chirp mass $\mathcal{M}/M_\odot$	$6.85^{+0.22}_{-0.08}$	$28.57^{+0.44}_{-0.77}$
Final mass $M_\mathrm{f}/M_\odot$	$15.3^{+0.7}_{-0.4}$	$62.7^{+1.0}_{-1.6}$
Effective inspiral spin χ_eff	$0.02^{+0.08}_{-0.02}$	$0.00^{+0.03}_{-0.04}$
Effective precession spin χ_p	$0.25^{+0.37}_{-0.20}$	$0.06^{+0.15}_{-0.05}$
Final spin χ_f	$0.69^{+0.02}_{-0.03}$	$0.69^{+0.01}_{-0.01}$
Luminosity distance D_L/Mpc	356^{+61}_{-162}	187^{+121}_{-52}
Redshift z	$0.08^{+0.01}_{-0.03}$	$0.04^{+0.03}_{-0.01}$
Network SNR ρ	$31.96^{+0.11}_{-0.15}$	$68.91^{+0.08}_{-0.11}$

ibration posterior is informative and distinct from the prior across the frequency range of the signal (f_{22}^{peak} is $\sim$ 170 Hz), similar to results for GW240925. For GW250207, we obtain JSDs between the posterior and prior of $0.15^{+0.11}_{-0.15}$ nat for amplitude and $0.14^{+0.13}_{-0.14}$ nat for phase. Some of the frequency-dependent structure reflects the discrete placement of spline nodes. The amplitude error near the 317.1 Hz node is only weakly constrained (likely by contributions from higher-order multipole moments); although the inferred error appears large, the posterior distribution is skewed and is still consistent with zero, with $\delta\mathcal{A} = 26^{+69}_{-32}\%$ (90% credible interval). The calibration is best constrained when using the in-situ measured priors for Livingston and Virgo, but the Hanford data alone remain informative. In the Hanford-only analysis, the overall (frequency-independent) calibration amplitude scale is fully degenerate with the source distance, since $h(\boldsymbol{\theta})$ scales inversely with distance, and the overall calibration phase scale is fully degenerate with the signal's reference phase. Therefore, the absolute scales of the Hanford-only constraints shown in Fig. 2 are prior driven: the prior favors $\delta\mathcal{A} \sim 0$ and $\delta\phi \sim 0$ deg. However, the *frequency-dependent* evolution of the calibration parameters can still be constrained using the signal morphology in the Hanford data alone.

Measurements of key astrophysical parameters for GW250207 are given in Table I. GW250207's source is similar to GW150914's [74, 92]. The BBH source has total mass of $M = 65.9^{+1.0}_{-1.7} M_\odot$ and a well-measured mass ratio of $q = 0.87^{+0.08}_{-0.08}$. The individual spins are small, with $\chi_1 < 0.15$ and $\chi_2 < 0.19$. These properties are consistent with the inferred BBH population, with component masses near the feature in the mass distribution at $\sim 35 M_\odot$ which contributes many observed binaries [83, 93]. With the inclusion of Hanford data, GW250207 has the second-highest network SNR published to date (after GW250114_082203 [7]), and its source is probably the closest BBH observed with $D_\mathrm{L} = 187^{+121}_{-52}$ Mpc [6, 92, 94, 95]. Such a high SNR facilitates more precise parameter estimation than for typical GW observations [6, 11].

GWs can be decomposed into spherical harmonics [96–99]. The $\ell = |m| = 2$ multipole moment dominates the signal. However, the high SNR of GW250207 means that other moments are observable; the signal probably has the highest $\ell = |m| = 4$ SNR found to date, $\rho_{44} = 5.1^{+0.5}_{-1.9}$ [6, 7, 100].

Comparing analysis results, we see that erroneously assuming perfect calibration for all detectors leads to narrower and, in some cases, biased posteriors for source parameters. The inferred distance becomes $D_\mathrm{L} = 175^{+42}_{-28}$ Mpc. The miscalibration at frequencies between $\sim$ 40–60 Hz is mistaken for a signature of spin precession: the constraint on the effective precession spin shifts from $\chi_\mathrm{p} = 0.06^{+0.15}_{-0.05}$, corresponding to

a precessing SNR [101, 102] of $\rho_{\rm p} = 2.4^{+4.8}_{-1.9}$ (using the wide prior for Hanford and in-situ priors for Livingston and Virgo) to $\chi_{\rm p} = 0.13^{+0.17}_{-0.07}$, $\rho_{\rm p} = 5.8^{+6.8}_{-3.1}$ (neglecting calibration uncertainties). This demonstrates how miscalibration can mimic physical effects and impact astrophysical inferences.

The sky localization is shown in Fig. 3. Again, neglecting calibration uncertainty leads to narrower posteriors. As for GW240925, and discussed in the Supplemental Material, the inclusion of Hanford data shifts the sky-position posterior such that it lies outside of the two-detector 90% area [82]. This type of shift can happen in (infrequent) cases where the third detector adds information that strongly disfavours locations in the two-detector 90% area [103, 104]. The inclusion of the Hanford data reduces the volume localization from $\sim 2 \times 10^6$ Mpc^3 to $\sim 5 \times 10^4$ Mpc^3. Without using Hanford data and accounting for its uncertain calibration, it would be difficult to locate the source.

These results for GW240925 and GW250207 demonstrate that astrophysical signals can be used to infer detector calibration, providing both a practical fallback when in-situ measured calibration is incomplete or uncertain and a valuable cross-check of analysis procedures. Further results are provided in the Supplemental Material.

Potential for dark siren cosmology— CBCs act as dark sirens providing constraints on their source distances; cross-referencing the inferred localization volume with galaxy catalogs that provide redshift information then enables inference of the Hubble constant [25, 105, 106]. Localization of GW sources is best for high-SNR signals observed with at least three detectors [80, 104, 107–109].

Since the two signals have well-localized sources, they could be considered as potentially useful dark sirens. Unfortunately, GW240925 will not provide significant cosmological information from its localization as it is hidden by the Milky Way plane. However, GW250207 has a localization volume of $\sim 5 \times 10^4$ Mpc^3, similar to that of GW190814 ($\sim 5 \times 10^4$ Mpc^3 [92, 110]), far from the Milky Way plane, making it well suited for a dark siren cosmological analysis. The host galaxy of GW250207 has an estimated probability $\sim 74\%$ to be present in the extended version of the Galaxy List for the Advanced Detector Era (GLADE+) catalog [111, 112]. This probability is based on the K-band luminosity, assumes that the likelihood of hosting a CBC is proportional to the galaxy luminosity, and adopts a flat cosmological model with $H_0 = 67.9$ km s^{-1} Mpc^{-1} and $\Omega_{\rm m} = 0.3065$ [43, 81]. Both signals will be included in a comprehensive analysis of all detections up to the end of O4, which will be presented with a future version of the Gravitational-Wave Transient Catalog (GWTC), similar to the analysis for GWTC-4.0 [106]. This population analysis will allow information from multiple detections to be combined with a proper computation of selection effects across observing runs.

Consistency tests— We perform a suite of verification tests using the two observations, including general residual analyses, tests that constrain deviations of post-Newtonian (PN) parameters from the expected GR values, and quasinormal mode (QNM) spectroscopy tests of the remnant. These tests are often framed as tests of GR, but are also sensitive to a variety of assumptions about the data. Failing to incorporate the calibration systematics in these analyses can lead to biased results, potentially mimicking or obscuring deviations from GR predictions [18, 23]. Here, we summarize results and provide additional details in the Supplemental Material.

The residuals test evaluates the agreement between the data and the best-fit GR waveform by searching for excess coherent power remaining after subtracting the signal [113–115]. Residual power may indicate the presence of calibration errors, instrumental artifacts or waveform-modeling errors. We find no evidence of residual power.

The FTI [116], TIGER [117–120] and PCA [121, 122] analyses explore deviations of the PN coefficients from the GR value in the inspiral signal. TIGER also allows for deviations in the phenomenological coefficients of the post-inspiral signal [120]. All analyses incorporate calibration uncertainties, like in the analyses to infer source properties, but now using waveform models that include the modeled deviations from GR. We find that neglecting calibration uncertainties can introduce mild biases in the inferred deviations, even though the results remain statistically consistent with GR. Using the wide, uninformative calibration priors mitigates the risk of falsely identifying GR violations. The GW250207 analyses for the PN deviation parameters give the tightest upper limits to date on the 2PN and higher-PN deviation parameters, surpassing GW250114_082203 [123]; at -1PN and 0.5PN, the constraints from GW170817 remain the best [124, 125].

For the ringdown signal, we use the pSEOBNR [126–130], QNMRF [131–134], and RINGDOWN [135–137] pipelines to perform QNM analyses. pSEOBNR can include calibration uncertainty with its parametrized waveform, but QNMRF and RINGDOWN do not currently support calibration marginalization and instead analyze Hanford and Livingston data separately to assess potential systematic errors. Figure 4 presents results from these analyses. These consistently show that neglecting calibration errors at Hanford leads to biased estimates for the $(2, 2, 0)$ QNM frequency and damping time relative to those inferred from the full inspiral–merger–ringdown (IMR) waveform. The 90% credible intervals on the $(2, 2, 0)$ QNM are compatible with GW230814_230901 [100], GW250114_082203 [7, 123], and other signals included in the GWTC-4.0 analysis [138].

Conclusion— Using the high-SNR BBH signals GW240925 and GW250207, observed during times of elevated calibration uncertainty, we have demonstrated that the information encoded within CBC signals can enable astrophysical calibration of GW detectors. With loud GW observations, we may cross-check in-situ calibration measurements. Furthermore, when we lack a complete set of calibration measurements, GW signals may be used to infer calibration properties: in such cases, signal-informed calibration is necessary and required to obtain precise and accurate source localization for multi-messenger follow-up and cosmological measurements, along with unbiased tests of

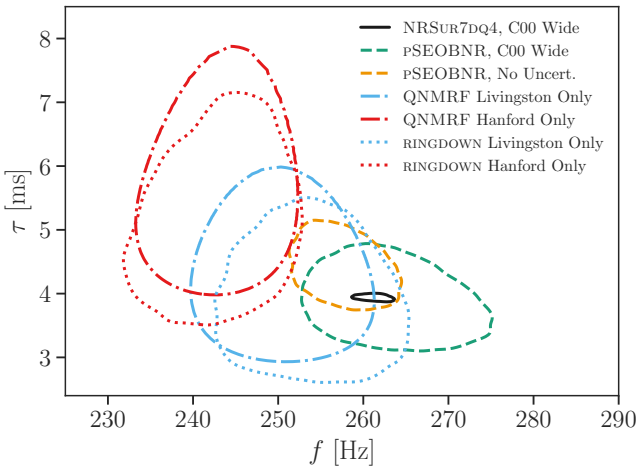

FIG. 4. Inferred $(2, 2, 0)$ QNM frequency and damping time from analyses of GW250207. The full IMR GR result, incorporating a wide prior for Hanford calibration, is indicated by the solid line. The pSEOBNR analysis (dashed) compares results obtained by either neglecting calibration uncertainties (yellow) or incorporating a wide prior for Hanford to marginalize over them (green). The QNMRF (dot–dashed) and ringdown (dotted) analyses analyze Hanford (red) and Livingston (light blue) data separately without calibration uncertainty to assess potential systematic errors. QNMRF and ringdown analyze the signal starting at $8t_{M_f}$ after the peak of the strain, where time is in units of the remnant mass in the detector frame (the maximum-likelihood estimate from the IMR analysis using the NRSur7dq4 waveform [139] and the wide calibration prior).

GR. Although astrophysical calibration has long been proposed as possible [19, 26, 29, 30], the groundbreaking higher SNRs found during O4 are now making it practical [26–28].

GW240925 and GW250207 were fortunately detected while multiple detectors were observing, allowing for a coherent analysis across the network. Having multiple observatories increases the probability of detection, improves source localization, and mitigates any adverse effects of detector noise on interpretation. Good source localization of GW250207 is only possible with the addition of LIGO Hanford data and the astrophysical inference of its calibration. Further expansion of the network [5, 80] with increasing sensitivity for KAGRA and the construction of LIGO India will enhance the opportunities for GW discovery and mitigate against cases where one observatory is adversely impacted by an instrumental problem, a glitch or a calibration issue. With a global observatory network, we are best prepared to fulfill the potential of GW astronomy and to make discoveries that advance our understanding of the Universe.

ACKNOWLEDGMENTS

We thank the anonymous referees for their constructive comments.

This material is based upon work supported by NSF's LIGO Laboratory, which is a major facility fully funded by the National Science Foundation. The authors also gratefully acknowledge the support of the Science and Technology Facilities Council (STFC) of the United Kingdom, the Max-Planck-Society (MPS), and the State of Niedersachsen/Germany for support of the construction of Advanced LIGO and construction and operation of the GEO 600 detector. Additional support for Advanced LIGO was provided by the Australian Research Council. The authors gratefully acknowledge the Italian Istituto Nazionale di Fisica Nucleare (INFN), the French Centre National de la Recherche Scientifique (CNRS) and the Netherlands Organization for Scientific Research (NWO) for the construction and operation of the Virgo detector and the creation and support of the EGO consortium. The authors also gratefully acknowledge research support from these agencies as well as by the Council of Scientific and Industrial Research of India, the Department of Science and Technology, India, the Science & Engineering Research Board (SERB), India, the Ministry of Human Resource Development, India, the Spanish Agencia Estatal de Investigación (AEI), the Spanish Ministerio de Ciencia, Innovación y Universidades, the European Union NextGenerationEU/PRTR (PRTR-C17.I1), the ICSC - CentroNazionale di Ricerca in High Performance Computing, Big Data and Quantum Computing, funded by the European Union NextGenerationEU, the Comunitat Autonòma de les Illes Balears through the Conselleria d'Educació i Universitats, the Conselleria d'Innovació, Universitats, Ciència i Societat Digital de la Generalitat Valenciana and the CERCA Programme Generalitat de Catalunya, Spain, the Polish National Agency for Academic Exchange, the National Science Centre of Poland and the European Union - European Regional Development Fund; the Foundation for Polish Science (FNP), the Polish Ministry of Science and Higher Education, the Swiss National Science Foundation (SNSF), the Russian Science Foundation, the European Commission, the European Social Funds (ESF), the European Regional Development Funds (ERDF), the Royal Society, the Scottish Funding Council, the Scottish Universities Physics Alliance, the Hungarian Scientific Research Fund (OTKA), the French Lyon Institute of Origins (LIO), the Belgian Fonds de la Recherche Scientifique (FRS-FNRS), Actions de Recherche Concertées (ARC) and Fonds Wetenschappelijk Onderzoek - Vlaanderen (FWO), Belgium, the Paris Île-de-France Region, the National Research, Development and Innovation Office of Hungary (NKFIH), the National Research Foundation of Korea, the Natural Sciences and Engineering Research Council of Canada (NSERC), the Canadian Foundation for Innovation (CFI), the Brazilian Ministry of Science, Technology, and Innovations, the International Center for Theoretical Physics South American Institute for Fundamental Research (ICTP-SAIFR), the Research Grants Council of Hong Kong, the National Natural Science Foundation of China (NSFC), the Israel Science Foundation (ISF), the US-Israel Binational Science Fund (BSF), the Leverhulme Trust, the Research Corporation, the National Science and Technology Council (NSTC), Taiwan, the United States Department of Energy,

and the Kavli Foundation. The authors gratefully acknowledge the support of the NSF, STFC, INFN and CNRS for provision of computational resources. This work was supported by MEXT, the JSPS Leading-edge Research Infrastructure Program, JSPS Grant-in-Aid for Specially Promoted Research 26000005, JSPS Grant-in-Aid for Scientific Research on Innovative Areas 2402: 24103006, 24103005, and 2905: JP17H06358, JP17H06361 and JP17H06364, JSPS Core-to-Core Program A. Advanced Research Networks, JSPS Grants-in-Aid for Scientific Research (S) 17H06133 and 20H05639, JSPS Grant-in-Aid for Transformative Research Areas (A) 20A203: JP20H05854, the joint research program of the Institute for Cosmic Ray Research, University of Tokyo, the National Research Foundation (NRF), the Computing Infrastructure Project of the Global Science experimental Data hub Center (GSDC) at KISTI, the Korea Astronomy and Space Science Institute (KASI), the Ministry of Science and ICT (MSIT) in Korea, Academia Sinica (AS), the AS Grid Center (ASGC) and the National Science and Technology Council (NSTC) in Taiwan under grants including the Science Vanguard Research Program, the Advanced Technology Center (ATC) of NAOJ, and the Mechanical Engineering Center of KEK.

Additional acknowledgements for support of individual authors may be found in: dcc.ligo.org/LIGO-M2300033/public. For the purpose of open access, the authors have applied a Creative Commons Attribution (CC BY) license to any Author Accepted Manuscript version arising.

We request that citations to this article use 'A. G. Abac *et al.* (LIGO–Virgo–KAGRA Collaboration), ...' or similar phrasing, depending on journal convention.

Calibration of the LIGO strain data was performed with GstLAL-based calibration software pipeline [34], and calibration of the Virgo strain data is performed with C-based software [17]. DQ products and event-validation results were computed using the BRiSTOL [140], DMT [141], DQR [142], DQSEGDB [143], Glitchfind [144], GSpyNetTree [145], gwdetchar [146], Hveto [147], iDQ [148], LigoDV-web [149], OmegaOverlap [150], Omicron [151], PEMcheck [152], PythonVirgoTools [153] and Stationarity [154] software packages and contributing software tools. Analyses relied upon the LALSuite software library [155, 156]. The detection of the signals and subsequent significance evaluations were performed with the GstLAL-based inspiral software pipeline [51–54], with the MBTA pipeline [60, 61], the PyCBC package [157–159] and the cWB packages [49, 50, 160–162]. Estimates of the noise spectra and glitch models, as well as tests of residuals, were obtained using BayesWave [163–165]. Signal parameter estimation was performed with the Bilby library [70, 71] using the Dynesty nested-sampling package [166]. SEOBNRv5PHM waveforms used in parameter estimation were generated using pySEOBNR [167]. PESummary was used to postprocess and collate parameter-estimation results [168]. Tests of GR were performed with the FTI [116], TIGER [118–120] and pSEOBNR [126–130] tests implemented in BilbyTGR [169], as well as with the QNMRF [131–134] and ringdown [135–137] pipelines. Cosmological inference was performed with the gwcosmo [170–172] and icarogw [173, 174] codes. Some of the parameter-estimation analysis were managed with the Asimov library [175]. Plots were prepared with Matplotlib [176], seaborn [177] and GWpy [178]. NumPy [179] and SciPy [180] were used in the preparation of the manuscript.

C01 strain data for GW240925 and C00 strain data for GW250207 analysed as part of this study are publicly available through Gravitational Wave Open Science Center (GWOSC) [181]; the (miscalibrated) C00 strain data for GW240925 are available in a supplemental release from Zenodo. Data releases of inference results, together with example scripts, are available from Zenodo [182].

REFERENCES

* Deceased, September 2024.
† Deceased, August 2025.

[1] B. P. Abbott *et al.* (LIGO Scientific Collaboration, Virgo Collaboration), Observation of Gravitational Waves from a Binary Black Hole Merger, Phys. Rev. Lett. **116**, 061102 (2016), arXiv:1602.03837 [gr-qc].

[2] J. Aasi *et al.* (LIGO Scientific Collaboration), Advanced LIGO, Classical Quantum Gravity **32**, 074001 (2015), arXiv:1411.4547 [gr-qc].

[3] F. Acernese *et al.* (Virgo Collaboration), Advanced Virgo: a second-generation interferometric gravitational wave detector, Classical Quantum Gravity **32**, 024001 (2015), arXiv:1408.3978 [gr-qc].

[4] T. Akutsu *et al.* (KAGRA Collaboration), Overview of KAGRA: Detector design and construction history, PTEP **2021**, 05A101 (2021), arXiv:2005.05574 [physics.ins-det].

[5] A. G. Abac *et al.* (LIGO Scientific Collaboration, Virgo Collaboration, KAGRA Collaboration), GWTC-4.0: An Introduction to Version 4.0 of the Gravitational-Wave Transient Catalog, Astrophys. J. Lett. **995**, L18 (2025), arXiv:2508.18080 [gr-qc].

[6] A. G. Abac *et al.* (LIGO Scientific Collaboration, Virgo Collaboration, KAGRA Collaboration), GWTC-4.0: Updating the Gravitational-Wave Transient Catalog with Observations from the First Part of the Fourth LIGO-Virgo-KAGRA Observing Run, arXiv e-prints (2025), arXiv:2508.18082 [gr-qc].

[7] A. G. Abac *et al.* (LIGO Scientific Collaboration, Virgo Collaboration, KAGRA Collaboration), GW250114: Testing Hawking's Area Law and the Kerr Nature of Black Holes, Phys. Rev. Lett. **135**, 111403 (2025), arXiv:2509.08054 [gr-qc].

[8] D. Ganapathy *et al.* (LIGO O4 Detector), Broadband Quantum Enhancement of the LIGO Detectors with Frequency-Dependent Squeezing, Phys. Rev. X **13**, 041021 (2023).

[9] W. Jia *et al.* (LIGO Instrument Science Collaboration), Squeezing the quantum noise of a gravitational-wave detector below the standard quantum limit, Science **385**, 1318 (2024), arXiv:2404.14569 [gr-qc].

[10] E. Capote *et al.*, Advanced LIGO detector performance in the fourth observing run, Phys. Rev. D **111**, 062002 (2025), arXiv:2411.14607 [gr-qc].

[11] C. Cutler and É. E. Flanagan, Gravitational waves from merg-

ing compact binaries: How accurately can one extract the binary's parameters from the inspiral waveform?, Phys. Rev. D **49**, 2658 (1994), arXiv:gr-qc/9402014.

[12] M. Pürrer and C.-J. Haster, Gravitational waveform accuracy requirements for future ground-based detectors, Phys. Rev. Res. **2**, 023151 (2020), arXiv:1912.10055 [gr-qc].

[13] B. P. Abbott *et al.* (LIGO Scientific Collaboration, Virgo Collaboration), A guide to LIGO–Virgo detector noise and extraction of transient gravitational-wave signals, Classical Quantum Gravity **37**, 055002 (2020), arXiv:1908.11170 [gr-qc].

[14] B. P. Abbott *et al.* (LIGO Scientific Collaboration), Calibration of the Advanced LIGO detectors for the discovery of the binary black-hole merger GW150914, Phys. Rev. D **95**, 062003 (2017), arXiv:1602.03845 [gr-qc].

[15] C. Cahillane *et al.* (LIGO Instrument Science Collaboration), Calibration uncertainty for Advanced LIGO's first and second observing runs, Phys. Rev. D **96**, 102001 (2017), arXiv:1708.03023 [astro-ph.IM].

[16] L. Sun *et al.*, Characterization of systematic error in Advanced LIGO calibration, Classical Quantum Gravity **37**, 225008 (2020), arXiv:2005.02531 [astro-ph.IM].

[17] F. Acernese *et al.* (Virgo Collaboration), Calibration of Advanced Virgo and reconstruction of the detector strain $h(t)$ during the Observing Run O3, Classical Quantum Gravity **39**, 045006 (2022), arXiv:2107.03294 [gr-qc].

[18] E. D. Hall, C. Cahillane, K. Izumi, R. J. E. Smith, and R. X. Adhikari, Systematic calibration error requirements for gravitational-wave detectors via the Cramér–Rao bound, Classical Quantum Gravity **36**, 205006 (2019), arXiv:1712.09719 [astro-ph.IM].

[19] R. Essick, Calibration uncertainty's impact on gravitational-wave observations, Phys. Rev. D **105**, 082002 (2022), arXiv:2202.00823 [astro-ph.IM].

[20] S. Vitale, W. Del Pozzo, T. G. F. Li, C. Van Den Broeck, I. Mandel, B. Aylott, and J. Veitch, Effect of calibration errors on Bayesian parameter estimation for gravitational wave signals from inspiral binary systems in the Advanced Detectors era, Phys. Rev. D **85**, 064034 (2012), arXiv:1111.3044 [gr-qc].

[21] S. Kumar, M. Melching, and F. Ohme, Accounting for the known unknowns: A parametric framework to incorporate systematic waveform errors in gravitational-wave parameter estimation, Phys. Rev. D **112**, 104071 (2025), arXiv:2502.17400 [gr-qc].

[22] Y. Huang, H.-Y. Chen, C.-J. Haster, L. Sun, S. Vitale, and J. S. Kissel, Impact of calibration uncertainties on Hubble constant measurements from gravitational-wave sources, Phys. Rev. D **111**, 063034 (2025), arXiv:2204.03614 [gr-qc].

[23] A. Gupta *et al.*, Possible causes of false general relativity violations in gravitational wave observations, SciPost Phys. Comm. Rep. 10.21468/SciPostPhysCommRep.5 (2024), arXiv:2405.02197 [gr-qc].

[24] M. R. Sinha, L. Sun, and S. Ma, Impact of Detector Calibration Accuracy on Black Hole Spectroscopy, Phys. Rev. D **112**, 084038 (2025), arXiv:2506.15979 [gr-qc].

[25] B. F. Schutz, Determining the Hubble Constant from Gravitational Wave Observations, Nature **323**, 310 (1986).

[26] R. Essick and D. E. Holz, Calibrating gravitational-wave detectors with GW170817, Classical Quantum Gravity **36**, 125002 (2019), arXiv:1902.08076 [astro-ph.IM].

[27] E. Payne, C. Talbot, P. D. Lasky, E. Thrane, and J. S. Kissel, Gravitational-wave astronomy with a physical calibration model, Phys. Rev. D **102**, 122004 (2020), arXiv:2009.10193 [astro-ph.IM].

[28] S. Vitale, C.-J. Haster, L. Sun, B. Farr, E. Goetz, J. Kissel, and C. Cahillane, Physical approach to the marginalization of LIGO calibration uncertainties, Phys. Rev. D **103**, 063016 (2021), arXiv:2009.10192 [gr-qc].

[29] M. Pitkin, C. Messenger, and L. Wright, Astrophysical calibration of gravitational-wave detectors, Phys. Rev. D **93**, 062002 (2016), arXiv:1511.02758 [astro-ph.IM].

[30] B. F. Schutz and B. S. Sathyaprakash, Self-calibration of Networks of Gravitational Wave Detectors, arXiv e-prints (2020), arXiv:2009.10212 [gr-qc].

[31] C. Alléné *et al.*, Relative calibration of the LIGO and Virgo detectors using astrophysical events from their third observing run, Classical Quantum Gravity **39**, 195019 (2022), arXiv:2204.00337 [gr-qc].

[32] C. Bond, D. Brown, A. Freise, and K. Strain, Interferometer Techniques for Gravitational-Wave Detection, Living Rev. Relativity **19**, 3 (2016), arXiv:0909.3661 [gr-qc].

[33] M. Pitkin, S. Reid, S. Rowan, and J. Hough, Gravitational Wave Detection by Interferometry (Ground and Space), Living Rev. Relativity **14**, 5 (2011), arXiv:1102.3355 [astro-ph.IM].

[34] A. D. Viets *et al.*, Reconstructing the calibrated strain signal in the Advanced LIGO detectors, Classical Quantum Gravity **35**, 095015 (2018), arXiv:1710.09973 [astro-ph.IM].

[35] T. Akutsu *et al.* (KAGRA Collaboration), Overview of KAGRA: Calibration, detector characterization, physical environmental monitors, and the geophysics interferometer, Prog. Theor. Exp. Phys. **2021**, 05A102 (2021), arXiv:2009.09305 [gr-qc].

[36] LIGO Scientific Collaboration, Virgo Collaboration, and KAGRA Collaboration, *LIGO Virgo KAGRA Calibration Uncertainty (O4)*, Tech. Rep. DCC-T2500288 (LIGO, Virgo, and KAGRA, 2025).

[37] B. Allen, *LIGO calibration accuracy*, Tech. Rep. LIGO-T960189 (LIGO, 1996).

[38] S. Karki *et al.*, The Advanced LIGO Photon Calibrators, Rev. Sci. Instrum. **87**, 114503 (2016), arXiv:1608.05055 [astro-ph.IM].

[39] D. Estevez, P. Lagabbe, A. Masserot, L. Rolland, M. Seglar-Arroyo, and D. Verkindt, The Advanced Virgo Photon Calibrators, Classical Quantum Gravity **38**, 075007 (2021), arXiv:2009.08103 [astro-ph.IM].

[40] D. Bhattacharjee, Y. Lecoeuche, S. Karki, J. Betzwieser, V. Bossilkov, S. Kandhasamy, E. Payne, and R. L. Savage, Fiducial displacements with improved accuracy for the global network of gravitational wave detectors, Classical Quantum Gravity **38**, 015009 (2021), arXiv:2006.00130 [astro-ph.IM].

[41] D. Chen *et al.*, Performance of the KAGRA photon calibrators during the fourth joint observing run with LIGO and Virgo, Classical Quantum Gravity **42**, 185018 (2025), arXiv:2504.12657 [astro-ph.IM].

[42] M. Wade *et al.*, Toward low-latency, high-fidelity calibration of the LIGO detectors with enhanced monitoring tools, Class. Quant. Grav. **42**, 215016 (2025), arXiv:2508.08423 [gr-qc].

[43] A. G. Abac *et al.* (LIGO Scientific Collaboration, Virgo Collaboration, KAGRA Collaboration), GWTC-4.0: Methods for Identifying and Characterizing Gravitational-wave Transients, arXiv e-prints (2025), arXiv:2508.18081 [gr-qc].

[44] F. Aubin, C. Grimaud, B. Mours, T. Pradier, L. Rolland, M. Seglar-Arroyo, H. Van Haevermaet, P. Van Hove, and D. Verkindt, From the Virgo interferometer calibration to the bias and uncertainty of the h(t) detector strain during the O4 run, J. Phys. Conf. Ser. **3177**, 012082 (2026), arXiv:2511.12566 [physics.ins-det].

[45] J. Betzwieser, *Calibration statements on OOOM requests for GW240925 and GW250207*, Tech. Rep. LIGO-T2500292

(LIGO, 2025).
[46] S. Chatterji, L. Blackburn, G. Martin, and E. Katsavounidis, Multiresolution techniques for the detection of gravitational-wave bursts, Classical Quantum Gravity **21**, S1809 (2004), arXiv:gr-qc/0412119.
[47] S. Klimenko, S. Mohanty, M. Rakhmanov, and G. Mitselmakher, Constraint likelihood analysis for a network of gravitational wave detectors, Phys. Rev. D **72**, 122002 (2005), arXiv:gr-qc/0508068.
[48] S. Klimenko, I. Yakushin, A. Mercer, and G. Mitselmakher, A coherent method for detection of gravitational wave bursts, Classical Quantum Gravity **25**, 114029 (2008), arXiv:0802.3232 [gr-qc].
[49] S. Klimenko *et al.*, Method for detection and reconstruction of gravitational wave transients with networks of advanced detectors, Phys. Rev. D **93**, 042004 (2016), arXiv:1511.05999 [gr-qc].
[50] T. Mishra, S. Bhaumik, V. Gayathri, M. J. Szczepańczyk, I. Bartos, and S. Klimenko, Gravitational waves detected by a burst search in LIGO/Virgo's third observing run, Phys. Rev. D **111**, 023054 (2025), arXiv:2410.15191 [astro-ph.HE].
[51] C. Messick *et al.*, Analysis Framework for the Prompt Discovery of Compact Binary Mergers in Gravitational-wave Data, Phys. Rev. D **95**, 042001 (2017), arXiv:1604.04324 [astro-ph.IM].
[52] S. Sachdev *et al.*, The GstLAL Search Analysis Methods for Compact Binary Mergers in Advanced LIGO's Second and Advanced Virgo's First Observing Runs, arXiv e-prints (2019), arXiv:1901.08580 [gr-qc].
[53] C. Hanna *et al.*, Fast evaluation of multidetector consistency for real-time gravitational wave searches, Phys. Rev. D **101**, 022003 (2020), arXiv:1901.02227 [gr-qc].
[54] K. Cannon *et al.*, GstLAL: A software framework for gravitational wave discovery, SoftwareX **14**, 100680 (2021), arXiv:2010.05082 [astro-ph.IM].
[55] S. Sakon *et al.*, Template bank for compact binary mergers in the fourth observing run of Advanced LIGO, Advanced Virgo, and KAGRA, Phys. Rev. D **109**, 044066 (2024), arXiv:2211.16674 [gr-qc].
[56] B. Ewing *et al.*, Performance of the low-latency GstLAL inspiral search towards LIGO, Virgo, and KAGRA's fourth observing run, Phys. Rev. D **109**, 042008 (2024), arXiv:2305.05625 [gr-qc].
[57] L. Tsukada *et al.*, Improved ranking statistics of the GstLAL inspiral search for compact binary coalescences, Phys. Rev. D **108**, 043004 (2023), arXiv:2305.06286 [astro-ph.IM].
[58] P. Joshi *et al.*, New Methods for Offline GstLAL Analyses, arXiv e-prints (2025), arXiv:2506.06497 [gr-qc].
[59] P. Joshi *et al.*, How Many Times Should We Matched Filter Gravitational Wave Data? A Comparison of GstLAL's Online and Offline Performance, arXiv e-prints (2025), arXiv:2505.23959 [gr-qc].
[60] T. Adams, D. Buskulic, V. Germain, G. M. Guidi, F. Marion, M. Montani, B. Mours, F. Piergiovanni, and G. Wang, Low-latency analysis pipeline for compact binary coalescences in the advanced gravitational wave detector era, Classical Quantum Gravity **33**, 175012 (2016), arXiv:1512.02864 [gr-qc].
[61] F. Aubin *et al.*, The MBTA pipeline for detecting compact binary coalescences in the third LIGO–Virgo observing run, Classical Quantum Gravity **38**, 095004 (2021), arXiv:2012.11512 [gr-qc].
[62] C. Alléné *et al.*, The MBTA pipeline for detecting compact binary coalescences in the fourth LIGO-Virgo-KAGRA observing run, Classical Quantum Gravity **42**, 105009 (2025), arXiv:2501.04598 [gr-qc].
[63] Q. Chu *et al.*, SPIIR online coherent pipeline to search for gravitational waves from compact binary coalescences, Phys. Rev. D **105**, 024023 (2022), arXiv:2011.06787 [gr-qc].
[64] L. P. Singer and L. R. Price, Rapid Bayesian position reconstruction for gravitational-wave transients, Phys. Rev. D **93**, 024013 (2016), arXiv:1508.03634 [gr-qc].
[65] L. P. Singer *et al.*, Going the Distance: Mapping Host Galaxies of LIGO and Virgo Sources in Three Dimensions Using Local Cosmography and Targeted Follow-up, Astrophys. J. Lett. **829**, L15 (2016), arXiv:1603.07333 [astro-ph.HE].
[66] S. Soni *et al.* (LIGO Instrument Science Collaboration), LIGO Detector Characterization in the first half of the fourth Observing run, Classical Quantum Gravity **42**, 085016 (2025), arXiv:2409.02831 [astro-ph.IM].
[67] L. K. Nuttall, Characterizing transient noise in the LIGO detectors, Phil. Trans. R. Soc. A **376**, 20170286 (2018), arXiv:1804.07592 [astro-ph.IM].
[68] J. Glanzer *et al.*, Data quality up to the third observing run of Advanced LIGO: Gravity Spy glitch classifications, Classical Quantum Gravity **40**, 065004 (2023), arXiv:2208.12849 [gr-qc].
[69] S. Hourihane and K. Chatziioannou, Glitches far from transient gravitational-wave events do not bias inference, Phys. Rev. D **112**, 084006 (2025), arXiv:2506.21869 [gr-qc].
[70] G. Ashton *et al.*, BILBY: A user-friendly Bayesian inference library for gravitational-wave astronomy, Astrophys. J. Suppl. Ser. **241**, 27 (2019), arXiv:1811.02042 [astro-ph.IM].
[71] I. M. Romero-Shaw *et al.*, Bayesian inference for compact binary coalescences with BILBY: validation and application to the first LIGO–Virgo gravitational-wave transient catalogue, Mon. Not. R. Astron. Soc. **499**, 3295 (2020), arXiv:2006.00714 [astro-ph.IM].
[72] T. Baka *et al.*, *Correcting misspecification of calibration uncertainties in gravitational-wave data analysis with efficient reweighting*, Tech. Rep. LIGO-T2500295 (LIGO, 2025).
[73] W. Farr, B. Farr, and T. Littenberg, *Modelling calibration errors in CBC waveforms*, Tech. Rep. LIGO-T1400682 (LIGO, 2014).
[74] B. P. Abbott *et al.* (LIGO Scientific Collaboration, Virgo Collaboration), Properties of the Binary Black Hole Merger GW150914, Phys. Rev. Lett. **116**, 241102 (2016), arXiv:1602.03840 [gr-qc].
[75] J. Lin, Divergence measures based on the Shannon entropy, IEEE Trans. Info. Theor. **37**, 145 (1991).
[76] B. P. Abbott *et al.* (LIGO Scientific Collaboration, Virgo Collaboration), Binary Black Hole Mergers in the first Advanced LIGO Observing Run, Phys. Rev. X **6**, 041015 (2016), [Erratum: Phys. Rev. X 8, 039903 (2018)], arXiv:1606.04856 [gr-qc].
[77] LIGO Scientific Collaboration, Virgo Collaboration and KAGRA Collaboration, LIGO/Virgo/KAGRA S240925n: Updated Sky localization and Source Classification, GCN **37607** (2024).
[78] L. Wen and Y. Chen, Geometrical Expression for the Angular Resolution of a Network of Gravitational-Wave Detectors, Phys. Rev. D **81**, 082001 (2010), arXiv:1003.2504 [astro-ph.CO].
[79] S. Fairhurst, Source localization with an advanced gravitational wave detector network, Classical Quantum Gravity **28**, 105021 (2011), arXiv:1010.6192 [gr-qc].
[80] B. P. Abbott *et al.* (KAGRA Collaboration, LIGO Scientific Collaboration, Virgo Collaboration), Prospects for observing and localizing gravitational-wave transients with Advanced

LIGO, Advanced Virgo and KAGRA, Living Rev. Relativity **23**, 3 (2020), arXiv:1304.0670 [gr-qc].
[81] P. A. R. Ade *et al.* (Planck Collaboration), Planck 2015 results. XIII. Cosmological parameters, Astron. Astrophys. **594**, A13 (2016), arXiv:1502.01589 [astro-ph.CO].
[82] LIGO Scientific Collaboration, Virgo Collaboration and KAGRA Collaboration, LIGO/Virgo/KAGRA S250207bg: Updated Sky localization, GCN **39242** (2025).
[83] A. G. Abac *et al.* (LIGO Scientific Collaboration, Virgo Collaboration, KAGRA Collaboration), GWTC-4.0: Population Properties of Merging Compact Binaries, arXiv e-prints (2025), arXiv:2508.18083 [astro-ph.HE].
[84] F. Özel, D. Psaltis, R. Narayan, and J. E. McClintock, The Black Hole Mass Distribution in the Galaxy, Astrophys. J. **725**, 1918 (2010), arXiv:1006.2834 [astro-ph.GA].
[85] W. M. Farr, N. Sravan, A. Cantrell, L. Kreidberg, C. D. Bailyn, I. Mandel, and V. Kalogera, The Mass Distribution of Stellar-Mass Black Holes, Astrophys. J. **741**, 103 (2011), arXiv:1011.1459 [astro-ph.GA].
[86] J. Casares and P. G. Jonker, Mass Measurements of Stellar and Intermediate Mass Black-Holes, Space Sci. Rev. **183**, 223 (2014), arXiv:1311.5118 [astro-ph.HE].
[87] J. Casares, I. Negueruela, M. Ribó, I. Ribas, J. M. Paredes, A. Herrero, and S. Simón-Díaz, A Be-type star with a black-hole companion, Nature **505**, 378 (2014), arXiv:1401.3711 [astro-ph.SR].
[88] J. M. Corral-Santana, J. Casares, T. Muñoz-Darias, F. E. Bauer, I. G. Martinez-Pais, and D. M. Russell, BlackCAT: A catalogue of stellar-mass black holes in X-ray transients, Astron. Astrophys. **587**, A61 (2016), arXiv:1510.08869 [astro-ph.HE].
[89] J. C. A. Miller-Jones *et al.*, Cygnus X-1 contains a 21–solar mass black hole—Implications for massive star winds, Science **371**, 1046 (2021), arXiv:2102.09091 [astro-ph.HE].
[90] P. Ajith *et al.*, Inspiral-merger-ringdown waveforms for black-hole binaries with non-precessing spins, Phys. Rev. Lett. **106**, 241101 (2011), arXiv:0909.2867 [gr-qc].
[91] L. Santamaria *et al.*, Matching post-Newtonian and numerical relativity waveforms: systematic errors and a new phenomenological model for non-precessing black hole binaries, Phys. Rev. D **82**, 064016 (2010), arXiv:1005.3306 [gr-qc].
[92] R. Abbott *et al.* (LIGO Scientific Collaboration, Virgo Collaboration), GWTC-2.1: Deep extended catalog of compact binary coalescences observed by LIGO and Virgo during the first half of the third observing run, Phys. Rev. D **109**, 022001 (2024), arXiv:2108.01045 [gr-qc].
[93] R. Abbott *et al.* (LIGO Scientific Collaboration, Virgo Collaboration), Population Properties of Compact Objects from the Second LIGO-Virgo Gravitational-Wave Transient Catalog, Astrophys. J. Lett. **913**, L7 (2021), arXiv:2010.14533 [astro-ph.HE].
[94] R. Abbott *et al.* (LIGO Scientific Collaboration, Virgo Collaboration, KAGRA Collaboration), GWTC-3: Compact Binary Coalescences Observed by LIGO and Virgo during the Second Part of the Third Observing Run, Phys. Rev. X **13**, 041039 (2023), arXiv:2111.03606 [gr-qc].
[95] A. G. Abac *et al.* (LIGO Scientific, KAGRA), GW241011 and GW241110: Exploring Binary Formation and Fundamental Physics with Asymmetric, High-spin Black Hole Coalescences, Astrophys. J. Lett. **993**, L21 (2025), arXiv:2510.26931 [astro-ph.HE].
[96] K. S. Thorne, Multipole Expansions of Gravitational Radiation, Rev. Mod. Phys. **52**, 299 (1980).
[97] L. Blanchet, Gravitational Radiation from Post-Newtonian Sources and Inspiralling Compact Binaries, Living Rev. Relativity **17**, 2 (2014), arXiv:1310.1528 [gr-qc].
[98] R. Abbott *et al.* (LIGO Scientific Collaboration, Virgo Collaboration), GW190412: Observation of a Binary-Black-Hole Coalescence with Asymmetric Masses, Phys. Rev. D **102**, 043015 (2020), arXiv:2004.08342 [astro-ph.HE].
[99] C. Mills and S. Fairhurst, Measuring gravitational-wave higher-order multipoles, Phys. Rev. D **103**, 024042 (2021), arXiv:2007.04313 [gr-qc].
[100] A. G. Abac *et al.* (LIGO Scientific Collaboration, Virgo Collaboration, KAGRA Collaboration), GW230814: investigation of a loud gravitational-wave signal observed with a single detector, arXiv e-prints (2025), arXiv:2509.07348 [gr-qc].
[101] S. Fairhurst, R. Green, C. Hoy, M. Hannam, and A. Muir, Two-harmonic approximation for gravitational waveforms from precessing binaries, Phys. Rev. D **102**, 024055 (2020), arXiv:1908.05707 [gr-qc].
[102] S. Fairhurst, R. Green, M. Hannam, and C. Hoy, When will we observe binary black holes precessing?, Phys. Rev. D **102**, 041302 (2020), arXiv:1908.00555 [gr-qc].
[103] L. P. Singer *et al.*, The First Two Years of Electromagnetic Follow-Up with Advanced LIGO and Virgo, Astrophys. J. **795**, 105 (2014), arXiv:1404.5623 [astro-ph.HE].
[104] A. Ouzriat, V. Sordini, and F. Di Renzo, Characterizing Low-Latency Sky Localization in Multi-Detector Gravitational-Wave Networks, arXiv e-prints (2025), arXiv:2510.21930 [astro-ph.HE].
[105] J. R. Gair *et al.*, The Hitchhiker's Guide to the Galaxy Catalog Approach for Dark Siren Gravitational-wave Cosmology, Astron. J. **166**, 22 (2023), arXiv:2212.08694 [gr-qc].
[106] A. G. Abac *et al.* (LIGO Scientific Collaboration, Virgo Collaboration, KAGRA Collaboration), GWTC-4.0: Constraints on the Cosmic Expansion Rate and Modified Gravitational-wave Propagation, arXiv e-prints (2025), arXiv:2509.04348 [astro-ph.CO].
[107] W. Del Pozzo, C. P. L. Berry, A. Ghosh, T. S. F. Haines, L. P. Singer, and A. Vecchio, Dirichlet Process Gaussian-mixture model: An application to localizing coalescing binary neutron stars with gravitational-wave observations, Mon. Not. R. Astron. Soc. **479**, 601 (2018), arXiv:1801.08009 [astro-ph.IM].
[108] C. Pankow, M. Rizzo, K. Rao, C. P. L. Berry, and V. Kalogera, Localization of Compact Binary Sources with Second Generation Gravitational-wave Interferometer Networks, Astrophys. J. **902**, 71 (2020), arXiv:1909.12961 [astro-ph.HE].
[109] M. Emma, T. F. de Nobrega, and G. Ashton, Comparing advanced-era interferometric gravitational-wave detector network configurations: Sky localization and source properties, Phys. Rev. D **110**, 064068 (2024), arXiv:2404.16949 [gr-qc].
[110] R. Abbott *et al.* (LIGO Scientific Collaboration, Virgo Collaboration), GW190814: Gravitational Waves from the Coalescence of a 23 Solar Mass Black Hole with a 2.6 Solar Mass Compact Object, Astrophys. J. Lett. **896**, L44 (2020), arXiv:2006.12611 [astro-ph.HE].
[111] G. Dálya, G. Galgóczi, L. Dobos, Z. Frei, I. S. Heng, R. Macas, C. Messenger, P. Raffai, and R. S. de Souza, GLADE: A galaxy catalogue for multimessenger searches in the advanced gravitational-wave detector era, Mon. Not. R. Astron. Soc. **479**, 2374 (2018), arXiv:1804.05709 [astro-ph.HE].
[112] G. Dálya *et al.*, GLADE+ : an extended galaxy catalogue for multimessenger searches with advanced gravitational-wave detectors, Mon. Not. R. Astron. Soc. **514**, 1403 (2022), arXiv:2110.06184 [astro-ph.CO].
[113] R. Abbott *et al.* (LIGO Scientific Collaboration, Virgo Col-

laboration, KAGRA Collaboration), Tests of General Relativity with GWTC-3, Phys. Rev. D **112**, 084080 (2025), arXiv:2112.06861 [gr-qc].

[114] N. K. Johnson-McDaniel, A. Ghosh, S. Ghonge, M. Saleem, N. V. Krishnendu, and J. A. Clark, Investigating the relation between gravitational wave tests of general relativity, Phys. Rev. D **105**, 044020 (2022), arXiv:2109.06988 [gr-qc].

[115] A. G. Abac *et al.* (LIGO Scientific Collaboration, Virgo Collaboration, KAGRA Collaboration), GWTC-4.0: Tests of General Relativity. I. Overview and General Tests, arXiv e-prints (2026), arXiv:2603.19019 [gr-qc].

[116] A. K. Mehta, A. Buonanno, R. Cotesta, A. Ghosh, N. Sennett, and J. Steinhoff, Tests of general relativity with gravitational-wave observations using a flexible theory-independent method, Phys. Rev. D **107**, 044020 (2023), arXiv:2203.13937 [gr-qc].

[117] T. G. F. Li, W. Del Pozzo, S. Vitale, C. Van Den Broeck, M. Agathos, J. Veitch, K. Grover, T. Sidery, R. Sturani, and A. Vecchio, Towards a generic test of the strong field dynamics of general relativity using compact binary coalescence, Phys. Rev. D **85**, 082003 (2012), arXiv:1110.0530 [gr-qc].

[118] M. Agathos, W. Del Pozzo, T. G. F. Li, C. Van Den Broeck, J. Veitch, and S. Vitale, TIGER: A data analysis pipeline for testing the strong-field dynamics of general relativity with gravitational wave signals from coalescing compact binaries, Phys. Rev. D **89**, 082001 (2014), arXiv:1311.0420 [gr-qc].

[119] J. Meidam *et al.*, Parametrized tests of the strong-field dynamics of general relativity using gravitational wave signals from coalescing binary black holes: Fast likelihood calculations and sensitivity of the method, Phys. Rev. D **97**, 044033 (2018), arXiv:1712.08772 [gr-qc].

[120] S. Roy, M. Haney, G. Pratten, P. T. H. Pang, and C. Van Den Broeck, Improved parametrized test of general relativity using the IMRPhenomX waveform family: Including higher harmonics and precession, Phys. Rev. D **113**, 024016 (2026), arXiv:2504.21147 [gr-qc].

[121] M. Saleem, S. Datta, K. G. Arun, and B. S. Sathyaprakash, Parametrized tests of post-Newtonian theory using principal component analysis, Phys. Rev. D **105**, 084062 (2022), arXiv:2110.10147 [gr-qc].

[122] P. Mahapatra *et al.*, Confronting General Relativity with Principal Component Analysis: Simulations and Results from GWTC-3 Events, Phys. Rev. D **112**, 104007 (2025), arXiv:2508.06862 [gr-qc].

[123] A. G. Abac *et al.* (LIGO Scientific Collaboration, Virgo Collaboration, KAGRA Collaboration), Black Hole Spectroscopy and Tests of General Relativity with GW250114, Phys. Rev. Lett. **136**, 041403 (2026), arXiv:2509.08099 [gr-qc].

[124] B. P. Abbott *et al.* (LIGO Scientific Collaboration, Virgo Collaboration), Tests of General Relativity with GW170817, Phys. Rev. Lett. **123**, 011102 (2019), arXiv:1811.00364 [gr-qc].

[125] A. G. Abac *et al.* (LIGO Scientific Collaboration, Virgo Collaboration, KAGRA Collaboration), GWTC-4.0: Tests of General Relativity. II. Parameterized Tests, arXiv e-prints (2026), arXiv:2603.19020 [gr-qc].

[126] R. Brito, A. Buonanno, and V. Raymond, Black-hole Spectroscopy by Making Full Use of Gravitational-Wave Modeling, Phys. Rev. D **98**, 084038 (2018), arXiv:1805.00293 [gr-qc].

[127] A. Ghosh, R. Brito, and A. Buonanno, Constraints on quasinormal-mode frequencies with LIGO-Virgo binary–black-hole observations, Phys. Rev. D **103**, 124041 (2021), arXiv:2104.01906 [gr-qc].

[128] E. Maggio, H. O. Silva, A. Buonanno, and A. Ghosh, Tests of general relativity in the nonlinear regime: A parametrized plunge-merger-ringdown gravitational waveform model, Phys. Rev. D **108**, 024043 (2023), arXiv:2212.09655 [gr-qc].

[129] A. Toubiana, L. Pompili, A. Buonanno, J. R. Gair, and M. L. Katz, Measuring source properties and quasinormal mode frequencies of heavy massive black-hole binaries with LISA, Phys. Rev. D **109**, 104019 (2024), arXiv:2307.15086 [gr-qc].

[130] L. Pompili, E. Maggio, H. O. Silva, and A. Buonanno, Parametrized spin-precessing inspiral-merger-ringdown waveform model for tests of general relativity, Phys. Rev. D **111**, 124040 (2025), arXiv:2504.10130 [gr-qc].

[131] S. Ma, K. Mitman, L. Sun, N. Deppe, F. Hébert, L. E. Kidder, J. Moxon, W. Throwe, N. L. Vu, and Y. Chen, Quasinormal-mode filters: A new approach to analyze the gravitational-wave ringdown of binary black-hole mergers, Phys. Rev. D **106**, 084036 (2022), arXiv:2207.10870 [gr-qc].

[132] S. Ma, L. Sun, and Y. Chen, Using rational filters to uncover the first ringdown overtone in GW150914, Phys. Rev. D **107**, 084010 (2023), arXiv:2301.06639 [gr-qc].

[133] S. Ma, L. Sun, and Y. Chen, Black Hole Spectroscopy by Mode Cleaning, Phys. Rev. Lett. **130**, 141401 (2023), arXiv:2301.06705 [gr-qc].

[134] N. Lu, S. Ma, O. J. Piccinni, L. Sun, and E. Finch, Statistical identification of ringdown modes with rational filters, Phys. Rev. D **112**, 064047 (2025), arXiv:2505.18560 [gr-qc].

[135] M. Isi, M. Giesler, W. M. Farr, M. A. Scheel, and S. A. Teukolsky, Testing the no-hair theorem with GW150914, Phys. Rev. Lett. **123**, 111102 (2019), arXiv:1905.00869 [gr-qc].

[136] M. Isi and W. M. Farr, Analyzing black-hole ringdowns, arXiv e-prints (2021), arXiv:2107.05609 [gr-qc].

[137] H. Siegel, M. Isi, and W. M. Farr, Analyzing black-hole ringdowns. II. Data conditioning, Phys. Rev. D **111**, 044070 (2025), arXiv:2410.02704 [gr-qc].

[138] A. G. Abac *et al.* (LIGO Scientific Collaboration, Virgo Collaboration, KAGRA Collaboration), GWTC-4.0: Tests of General Relativity. III. Tests of the Remnants, arXiv e-prints (2026), arXiv:2603.19021 [gr-qc].

[139] V. Varma, S. E. Field, M. A. Scheel, J. Blackman, L. E. Kidder, and H. P. Pfeiffer, Surrogate model of hybridized numerical relativity binary black hole waveforms, Phys. Rev. D **99**, 064045 (2019), arXiv:1812.07865 [gr-qc].

[140] F. Di Renzo, F. Fidecaro, M. Razzano, and N. Sorrentino, BRiSTOL - a Band-limited RMS Stationarity Test Tool for Gravitational Wave Data, in *55th Rencontres de Moriond on Gravitation* (2024) arXiv:2401.15392 [gr-qc].

[141] John Zweizig, The Data Monitor Tool Project, labcit.ligo.caltech.edu/˜jzweizig/DMT-Project.html (2006).

[142] LIGO Scientific Collaboration and Virgo Collaboration, Data quality report user documentation, docs.ligo.org/detchar/data-quality-report/ (2018).

[143] R. P. Fisher, G. Hemming, M.-A. Bizouard, D. A. Brown, P. F. Couvares, F. Robinet, and D. Verkindt, DQSEGDB: A time-interval database for storing gravitational wave observatory metadata, SoftwareX **14**, 100677 (2021), arXiv:2008.11316 [astro-ph.IM].

[144] L. Vazsonyi and D. Davis, Identifying glitches near gravitational-wave signals from compact binary coalescences using the Q-transform, Class. Quant. Grav. **40**, 035008 (2023), arXiv:2208.12338 [astro-ph.IM].

[145] S. Alvarez-Lopez, A. Liyanage, J. Ding, R. Ng, and J. McIver, GSpyNetTree: a signal-vs-glitch classifier for gravitational-wave event candidates, Class. Quant. Grav. **41**, 085007 (2024), arXiv:2304.09977 [gr-qc].

[146] A. L. Urban *et al.*, gwdetchar/gwdetchar, doi.org/10.5281/zenodo.2575786 (2021).

[147] J. R. Smith, T. Abbott, E. Hirose, N. Leroy, D. Macleod, J. McIver, P. Saulson, and P. Shawhan, A Hierarchical method for vetoing noise transients in gravitational-wave detectors, Classical Quantum Gravity **28**, 235005 (2011), arXiv:1107.2948 [gr-qc].

[148] R. Essick, P. Godwin, C. Hanna, L. Blackburn, and E. Katsavounidis, iDQ: Statistical Inference of Non-Gaussian Noise with Auxiliary Degrees of Freedom in Gravitational-Wave Detectors, Mach. Learn. Sci. Technol. **2**, 015004 (2020), arXiv:2005.12761 [astro-ph.IM].

[149] J. S. Areeda, J. R. Smith, A. P. Lundgren, E. Maros, D. M. Macleod, and J. Zweizig, LigoDV-web: Providing easy, secure and universal access to a large distributed scientific data store for the LIGO Scientific Collaboration, Astron. Comput. **18**, 27 (2017), arXiv:1611.01089 [astro-ph.IM].

[150] R. Macas and A. Lundgren, Sensitive test of non-Gaussianity in gravitational-wave detector data, Phys. Rev. D **108**, 063016 (2023), arXiv:2306.09019 [gr-qc].

[151] F. Robinet, N. Arnaud, N. Leroy, A. Lundgren, D. Macleod, and J. McIver, Omicron: a tool to characterize transient noise in gravitational-wave detectors, SoftwareX **12**, 100620 (2020), arXiv:2007.11374 [astro-ph.IM].

[152] A. Helmling-Cornell, P. Nguyen, R. Schofield, and R. Frey, Automated evaluation of environmental coupling for Advanced LIGO gravitational wave detections, Classical Quantum Gravity **41**, 145003 (2024), arXiv:2312.00735 [gr-qc].

[153] Virgo Collaboration, PythonVirgoTools, git.ligo.org/virgo/virgoapp/PythonVirgoTools (2021).

[154] S. Mozzon, L. K. Nuttall, A. Lundgren, T. Dent, S. Kumar, and A. H. Nitz, Dynamic Normalization for Compact Binary Coalescence Searches in Non-Stationary Noise, Classical Quantum Gravity **37**, 215014 (2020), arXiv:2002.09407 [astro-ph.IM].

[155] LIGO Scientific Collaboration, Virgo Collaboration, and KAGRA Collaboration, LVK Algorithm Library Suite, doi.org/10.7935/GT1W-FZ16 (2018).

[156] K. Wette, SWIGLAL: Python and Octave interfaces to the LALSuite gravitational-wave data analysis libraries, SoftwareX **12**, 100634 (2020), arXiv:2012.09552 [astro-ph.IM].

[157] S. A. Usman *et al.*, The PyCBC search for gravitational waves from compact binary coalescence, Classical Quantum Gravity **33**, 215004 (2016), arXiv:1508.02357 [gr-qc].

[158] A. H. Nitz, T. Dent, T. Dal Canton, S. Fairhurst, and D. A. Brown, Detecting binary compact-object mergers with gravitational waves: Understanding and Improving the sensitivity of the PyCBC search, Astrophys. J. **849**, 118 (2017), arXiv:1705.01513 [gr-qc].

[159] G. S. Davies, T. Dent, M. Tápai, I. Harry, C. McIsaac, and A. H. Nitz, Extending the PyCBC search for gravitational waves from compact binary mergers to a global network, Phys. Rev. D **102**, 022004 (2020), arXiv:2002.08291 [astro-ph.HE].

[160] S. Klimenko and G. Mitselmakher, A wavelet method for detection of gravitational wave bursts, Classical Quantum Gravity **21**, S1819 (2004).

[161] S. Klimenko, G. Vedovato, M. Drago, G. Mazzolo, G. Mitselmakher, C. Pankow, G. Prodi, V. Re, F. Salemi, and I. Yakushin, Localization of gravitational wave sources with networks of advanced detectors, Phys. Rev. D **83**, 102001 (2011), arXiv:1101.5408 [astro-ph.IM].

[162] M. Drago *et al.*, coherent WaveBurst, a pipeline for unmodeled gravitational-wave data analysis, SoftwareX **14**, 100678 (2021), arXiv:2006.12604 [gr-qc].

[163] N. J. Cornish and T. B. Littenberg, BayesWave: Bayesian Inference for Gravitational Wave Bursts and Instrument Glitches, Classical Quantum Gravity **32**, 135012 (2015), arXiv:1410.3835 [gr-qc].

[164] T. B. Littenberg, J. B. Kanner, N. J. Cornish, and M. Millhouse, Enabling high confidence detections of gravitational-wave bursts, Phys. Rev. D **94**, 044050 (2016), arXiv:1511.08752 [gr-qc].

[165] N. J. Cornish, T. B. Littenberg, B. Bécsy, K. Chatziioannou, J. A. Clark, S. Ghonge, and M. Millhouse, BayesWave analysis pipeline in the era of gravitational wave observations, Phys. Rev. D **103**, 044006 (2021), arXiv:2011.09494 [gr-qc].

[166] J. S. Speagle, dynesty: a dynamic nested sampling package for estimating Bayesian posteriors and evidences, Mon. Not. R. Astron. Soc. **493**, 3132 (2020), arXiv:1904.02180 [astro-ph.IM].

[167] D. P. Mihaylov, S. Ossokine, A. Buonanno, H. Estelles, L. Pompili, M. Pürrer, and A. Ramos-Buades, pySEOBNR: a software package for the next generation of effective-one-body multipolar waveform models, SoftwareX **30**, 102080 (2025), arXiv:2303.18203 [gr-qc].

[168] C. Hoy and V. Raymond, PESummary: the code agnostic Parameter Estimation Summary page builder, SoftwareX **15**, 100765 (2021), arXiv:2006.06639 [astro-ph.IM].

[169] G. Ashton *et al.*, Bilby TGR, doi.org/10.5281/zenodo.15676285 (2025).

[170] R. Gray *et al.*, Cosmological inference using gravitational wave standard sirens: A mock data analysis, Phys. Rev. D **101**, 122001 (2020), arXiv:1908.06050 [gr-qc].

[171] R. Gray, C. Messenger, and J. Veitch, A pixelated approach to galaxy catalogue incompleteness: improving the dark siren measurement of the Hubble constant, Mon. Not. Roy. Astron. Soc. **512**, 1127 (2022), arXiv:2111.04629 [astro-ph.CO].

[172] R. Gray *et al.*, Joint cosmological and gravitational-wave population inference using dark sirens and galaxy catalogues, J. Cosmol. Astropart. Phys. **12** (2023), 023, arXiv:2308.02281 [astro-ph.CO].

[173] S. Mastrogiovanni, D. Laghi, R. Gray, G. C. Santoro, A. Ghosh, C. Karathanasis, K. Leyde, D. A. Steer, S. Perries, and G. Pierra, Joint population and cosmological properties inference with gravitational waves standard sirens and galaxy surveys, Phys. Rev. D **108**, 042002 (2023), arXiv:2305.10488 [astro-ph.CO].

[174] S. Mastrogiovanni, G. Pierra, S. Perriès, D. Laghi, G. Caneva Santoro, A. Ghosh, R. Gray, C. Karathanasis, and K. Leyde, ICAROGW: A python package for inference of astrophysical population properties of noisy, heterogeneous, and incomplete observations, Astron. Astrophys. **682**, A167 (2024), arXiv:2305.17973 [astro-ph.CO].

[175] D. Williams, J. Veitch, M. L. Chiofalo, P. Schmidt, R. P. Udall, A. Vajpeji, and C. Hoy, Asimov: A framework for coordinating parameter estimation workflows, J. Open Source Softw. **8**, 4170 (2023), arXiv:2207.01468 [gr-qc].

[176] J. D. Hunter, Matplotlib: A 2D Graphics Environment, Comput. Sci. Eng. **9**, 90 (2007).

[177] M. L. Waskom, seaborn: statistical data visualization, J. Open Source Softw. **6**, 3021 (2021).

[178] D. Macleod *et al.*, gwpy/gwpy, doi.org/10.5281/zenodo.597016 (2021).

[179] C. R. Harris *et al.*, Array programming with NumPy, Nature **585**, 357 (2020), arXiv:2006.10256 [cs.MS].

[180] P. Virtanen *et al.*, SciPy 1.0–Fundamental Algorithms for Scientific Computing in Python, Nat. Meth. **17**, 261 (2020), arXiv:1907.10121 [cs.MS].

[181] A. G. Abac *et al.* (LIGO Scientific Collaboration, Virgo Collaboration, KAGRA Collaboration), Open Data from LIGO, Virgo, and KAGRA through the First Part of the Fourth Observing Run, arXiv e-prints (2025), arXiv:2508.18079 [gr-qc].

[182] LIGO Scientific Collaboration, Virgo Collaboration and KAGRA Collaboration, Data Release for GW240925 and GW250207: Astrophysical Calibration of Gravitational-wave Detectors (2026).

[183] C. Grimaud, *Virgo interferometer calibration and h(t) strain reconstruction uncertainty during the O4 observing run*, Ph.D. thesis, Université Savoie Mont Blanc (2025).

[184] A. G. Sullivan *et al.*, Timing system of LIGO discoveries, Phys. Rev. D **108**, 022003 (2023), arXiv:2304.01188 [astro-ph.IM].

[185] F. Aubin, E. Dangelser, D. Estevez, A. Masserot, B. Mours, T. Pradier, A. Syx, and P. Van Hove, The Virgo Newtonian calibration system for the O4 observing run, Classical Quantum Gravity **41**, 235003 (2024), arXiv:2406.10028 [gr-qc].

[186] S. Soni *et al.* (LIGO Instrument Science Collaboration), Reducing scattered light in LIGO's third observing run, Classical Quantum Gravity **38**, 025016 (2021), arXiv:2007.14876 [astro-ph.IM].

[187] J. Glanzer, S. Soni, J. Spoon, A. Effler, and G. González, Noise in the LIGO livingston gravitational wave observatory due to trains, Classical Quantum Gravity **40**, 195015 (2023), arXiv:2304.07477 [astro-ph.IM].

[188] S. Soni, J. Glanzer, A. Effler, V. Frolov, G. González, A. Pele, and R. Schofield, Modeling and reduction of high frequency scatter noise at LIGO Livingston, Classical Quantum Gravity **41**, 135015 (2024), arXiv:2311.05730 [astro-ph.IM].

[189] P. B. Covas *et al.* (LIGO Instrument Science Collaboration), Identification and mitigation of narrow spectral artifacts that degrade searches for persistent gravitational waves in the first two observing runs of Advanced LIGO, Phys. Rev. D **97**, 082002 (2018), arXiv:1801.07204 [astro-ph.IM].

[190] D. Davis *et al.* (LIGO Instrument Science Collaboration), LIGO Detector Characterization in the Second and Third Observing Runs, Classical Quantum Gravity **38**, 135014 (2021), arXiv:2101.11673 [astro-ph.IM].

[191] F. Acernese *et al.* (Virgo Collaboration), Virgo detector characterization and data quality: tools, Classical Quantum Gravity **40**, 185005 (2023), arXiv:2210.15634 [gr-qc].

[192] G. Vajente, Y. Huang, M. Isi, J. C. Driggers, J. S. Kissel, M. J. Szczepańczyk, and S. Vitale, Machine-learning nonstationary noise out of gravitational-wave detectors, Phys. Rev. D **101**, 042003 (2020), arXiv:1911.09083 [gr-qc].

[193] S. Hourihane, K. Chatziioannou, M. Wijngaarden, D. Davis, T. Littenberg, and N. Cornish, Accurate modeling and mitigation of overlapping signals and glitches in gravitational-wave data, Phys. Rev. D **106**, 042006 (2022), arXiv:2205.13580 [gr-qc].

[194] D. Davis, T. B. Littenberg, I. M. Romero-Shaw, M. Millhouse, J. McIver, F. Di Renzo, and G. Ashton, Subtracting glitches from gravitational-wave detector data during the third LIGO-Virgo observing run, Classical Quantum Gravity **39**, 245013 (2022), arXiv:2207.03429 [astro-ph.IM].

[195] B. Allen, W. G. Anderson, P. R. Brady, D. A. Brown, and J. D. E. Creighton, FINDCHIRP: An Algorithm for detection of gravitational waves from inspiraling compact binaries, Phys. Rev. D **85**, 122006 (2012), arXiv:gr-qc/0509116.

[196] H.-Y. Chen, D. E. Holz, J. Miller, M. Evans, S. Vitale, and J. Creighton, Distance measures in gravitational-wave astrophysics and cosmology, Classical Quantum Gravity **38**, 055010 (2021), arXiv:1709.08079 [astro-ph.CO].

[197] B. P. Abbott *et al.* (LIGO Scientific Collaboration, Virgo Collaboration), Low-latency Gravitational-wave Alerts for Multimessenger Astronomy during the Second Advanced LIGO and Virgo Observing Run, Astrophys. J. **875**, 161 (2019), arXiv:1901.03310 [astro-ph.HE].

[198] T. Dal Canton, A. H. Nitz, B. Gadre, G. S. Cabourn Davies, V. Villa-Ortega, T. Dent, I. Harry, and L. Xiao, Real-time Search for Compact Binary Mergers in Advanced LIGO and Virgo's Third Observing Run Using PyCBC Live, Astrophys. J. **923**, 254 (2021), arXiv:2008.07494 [astro-ph.HE].

[199] T. Dal Canton *et al.*, Implementing a search for aligned-spin neutron star-black hole systems with advanced ground based gravitational wave detectors, Phys. Rev. D **90**, 082004 (2014), arXiv:1405.6731 [gr-qc].

[200] B. P. Abbott *et al.* (LIGO Scientific Collaboration, Virgo Collaboration), GW150914: First results from the search for binary black hole coalescence with Advanced LIGO, Phys. Rev. D **93**, 122003 (2016), arXiv:1602.03839 [gr-qc].

[201] R. Essick *et al.*, Compact binary coalescence sensitivity estimates with injection campaigns during the LIGO-Virgo-KAGRA Collaborations' fourth observing run, Phys. Rev. D **112**, 102001 (2025), arXiv:2508.10638 [gr-qc].

[202] L. Blanchet, T. Damour, B. R. Iyer, C. M. Will, and A. G. Wiseman, Gravitational radiation damping of compact binary systems to second postNewtonian order, Phys. Rev. Lett. **74**, 3515 (1995), arXiv:gr-qc/9501027.

[203] N. Christensen and R. Meyer, Parameter estimation with gravitational waves, Rev. Mod. Phys. **94**, 025001 (2022), arXiv:2204.04449 [gr-qc].

[204] T. B. Littenberg and N. J. Cornish, Bayesian inference for spectral estimation of gravitational wave detector noise, Phys. Rev. D **91**, 084034 (2015), arXiv:1410.3852 [gr-qc].

[205] G. Pratten *et al.*, Computationally efficient models for the dominant and subdominant harmonic modes of precessing binary black holes, Phys. Rev. D **103**, 104056 (2021), arXiv:2004.06503 [gr-qc].

[206] M. Colleoni, F. A. R. Vidal, C. García-Quirós, S. Akçay, and S. Bera, Fast frequency-domain gravitational waveforms for precessing binaries with a new twist, Phys. Rev. D **111**, 104019 (2025), arXiv:2412.16721 [gr-qc].

[207] E. Hamilton, L. London, J. E. Thompson, E. Fauchon-Jones, M. Hannam, C. Kalaghatgi, S. Khan, F. Pannarale, and A. Vano-Vinuales, Model of gravitational waves from precessing black-hole binaries through merger and ringdown, Phys. Rev. D **104**, 124027 (2021), arXiv:2107.08876 [gr-qc].

[208] E. Hamilton *et al.*, PhenomXPNR: An improved gravitational wave model linking precessing inspirals and NR-calibrated merger-ringdown, arXiv e-prints (2025), arXiv:2507.02604 [gr-qc].

[209] A. Ramos-Buades, A. Buonanno, H. Estellés, M. Khalil, D. P. Mihaylov, S. Ossokine, L. Pompili, and M. Shiferaw, Next generation of accurate and efficient multipolar precessing-spin effective-one-body waveforms for binary black holes, Phys. Rev. D **108**, 124037 (2023), arXiv:2303.18046 [gr-qc].

[210] H. Estellés, A. Buonanno, R. Enficiaud, C. Foo, and L. Pompili, Adding equatorial-asymmetric effects for spin-precessing binaries into the SEOBNRv5PHM waveform model, Phys. Rev. D **113**, 044049 (2026), arXiv:2506.19911 [gr-qc].

[211] G. Pratten, S. Husa, C. Garcia-Quiros, M. Colleoni, A. Ramos-Buades, H. Estelles, and R. Jaume, Setting the cornerstone for a family of models for gravitational waves from compact binaries: The dominant harmonic for nonprecessing quasicircular black holes, Phys. Rev. D **102**, 064001 (2020), arXiv:2001.11412 [gr-qc].

[212] R. Abbott *et al.* (LIGO Scientific Collaboration, Virgo Collaboration), GWTC-2: Compact Binary Coalescences Observed by LIGO and Virgo During the First Half of the Third Observing Run, Phys. Rev. X **11**, 021053 (2021), arXiv:2010.14527 [gr-qc].
[213] LIGO Scientific Collaboration, Virgo Collaboration and KAGRA Collaboration, LIGO/Virgo/KAGRA S240925n: Identification of a GW compact binary merger candidate, GCN **37604** (2024).
[214] A. Krolak and B. F. Schutz, Coalescing binaries — Probe of the universe, Gen. Relativ. Gravit. **19**, 1163 (1987).
[215] S. Nissanke, D. E. Holz, S. A. Hughes, N. Dalal, and J. L. Sievers, Exploring short gamma-ray bursts as gravitational-wave standard sirens, Astrophys. J. **725**, 496 (2010), arXiv:0904.1017 [astro-ph.CO].
[216] T. Narikawa, M. Kaneyama, and H. Tagoshi, Optimal follow-up observations of gravitational wave events with small optical telescopes, Phys. Rev. D **96**, 084067 (2017), arXiv:1705.04008 [gr-qc].
[217] S. A. Usman, J. C. Mills, and S. Fairhurst, Constraining the Inclinations of Binary Mergers from Gravitational-wave Observations, Astrophys. J. **877**, 82 (2019), arXiv:1809.10727 [gr-qc].
[218] B. S. Sathyaprakash and B. F. Schutz, Physics, Astrophysics and Cosmology with Gravitational Waves, Living Rev. Relativity **12**, 2 (2009), arXiv:0903.0338 [gr-qc].
[219] B. P. Abbott *et al.* (LIGO Scientific Collaboration, Virgo Collaboration), Effects of waveform model systematics on the interpretation of GW150914, Classical Quantum Gravity **34**, 104002 (2017), arXiv:1611.07531 [gr-qc].
[220] K. S. Thorne, Gravitational radiation, in *Three hundred years of gravitation*, edited by S. W. Hawking and W. Israel (Cambridge University Press, Cambridge, 1987) Chap. 9, pp. 330–458.
[221] L. S. Finn and D. F. Chernoff, Observing binary inspiral in gravitational radiation: One interferometer, Phys. Rev. D **47**, 2198 (1993), arXiv:gr-qc/9301003.
[222] B. F. Schutz, Networks of gravitational wave detectors and three figures of merit, Classical Quantum Gravity **28**, 125023 (2011), arXiv:1102.5421 [astro-ph.IM].
[223] B. P. Abbott *et al.* (LIGO Scientific Collaboration, Virgo Collaboration), GW170814: A Three-Detector Observation of Gravitational Waves from a Binary Black Hole Coalescence, Phys. Rev. Lett. **119**, 141101 (2017), arXiv:1709.09660 [gr-qc].
[224] B. P. Abbott *et al.* (LIGO Scientific Collaboration, Virgo Collaboration), GW170817: Observation of Gravitational Waves from a Binary Neutron Star Inspiral, Phys. Rev. Lett. **119**, 161101 (2017), arXiv:1710.05832 [gr-qc].
[225] K. Pearson, Note on regression and inheritance in the case of two parents, Proc. R. Soc. Lond. **58**, 240 (1895).
[226] R. Essick, S. Vitale, E. Katsavounidis, G. Vedovato, and S. Klimenko, Localization of short duration gravitational-wave transients with the early advanced LIGO and Virgo detectors, Astrophys. J. **800**, 81 (2015), arXiv:1409.2435 [astro-ph.HE].
[227] L. Sampson, N. Cornish, and N. Yunes, Gravitational Wave Tests of Strong Field General Relativity with Binary Inspirals: Realistic Injections and Optimal Model Selection, Phys. Rev. D **87**, 102001 (2013), arXiv:1303.1185 [gr-qc].
[228] B. Edelman *et al.*, Constraining unmodeled physics with compact binary mergers from GWTC-1, Phys. Rev. D **103**, 042004 (2021), arXiv:2008.06436 [gr-qc].
[229] L. Pompili *et al.*, Laying the foundation of the effective-one-body waveform models SEOBNRv5: Improved accuracy and efficiency for spinning nonprecessing binary black holes, Phys. Rev. D **108**, 124035 (2023), arXiv:2303.18039 [gr-qc].
[230] R. Abbott *et al.* (LIGO Scientific Collaboration, Virgo Collaboration), Tests of general relativity with binary black holes from the second LIGO–Virgo gravitational-wave transient catalog, Phys. Rev. D **103**, 122002 (2021), arXiv:2010.14529 [gr-qc].
[231] E. M. Sänger *et al.*, Tests of General Relativity with GW230529: a neutron star merging with a lower mass-gap compact object, arXiv e-prints (2024), arXiv:2406.03568 [gr-qc].
[232] A. Pai and K. G. Arun, Singular value decomposition in parametrised tests of post-Newtonian theory, Classical Quantum Gravity **30**, 025011 (2013), arXiv:1207.1943 [gr-qc].
[233] A. A. Shoom, P. K. Gupta, B. Krishnan, A. B. Nielsen, and C. D. Capano, Testing the post-Newtonian expansion with GW170817, Gen. Rel. Grav. **55**, 55 (2023), arXiv:2105.02191 [gr-qc].

SUPPLEMENTAL MATERIAL

CALIBRATION TECHNIQUES AND MONITORING

Since the detector arm length L is known to high precision, to reconstruct the strain we must accurately measure the differential arm length change $\Delta L_{\rm free}$. However, as $\Delta L_{\rm free}$ is suppressed by feedback control, the detectors only measure the residual differential arm displacement $\Delta L_{\rm res}$. In LIGO, this is converted to a digital error signal $d_{\rm err}$ via the sensing transfer function C, such that $d_{\rm err} = C\Delta L_{\rm res}$ (all quantities are denoted in frequency domain) [14–16, 34]. The error signal is processed by a set of digital filters D to generate the digital control signal $d_{\rm ctrl} = Dd_{\rm err}$, which is sent through the actuation transfer function A to produce the analog control displacement $\Delta L_{\rm ctrl} = Ad_{\rm ctrl}$. The total free differential arm length change is given by $\Delta L_{\rm free} = \Delta L_{\rm res} + \Delta L_{\rm ctrl}$. Defining the detector response function as [13]

$$R = \frac{1}{C} + AD, \tag{3}$$

the strain is reconstructed as [37]

$$d = \frac{R\, d_{\rm err}}{L}. \tag{4}$$

KAGRA adopts an approach closely aligned with that of LIGO [35], and Virgo follows similar procedures, with minor differences in conventions and technical implementations [17, 183].

The timing for the detectors' real-time control systems and recorded data, provided by Global Positioning System (GPS) receivers located at the corner and end stations of each detector, serves as a critical absolute reference. Cross-checks between multiple GPS clocks and a local atomic clock estimate the timing accuracy to be better than ± 1 μs [42, 184].

Calibration errors in the modeled response function $R^{(\rm model)}(f;t)$ may result from imperfect estimates of model

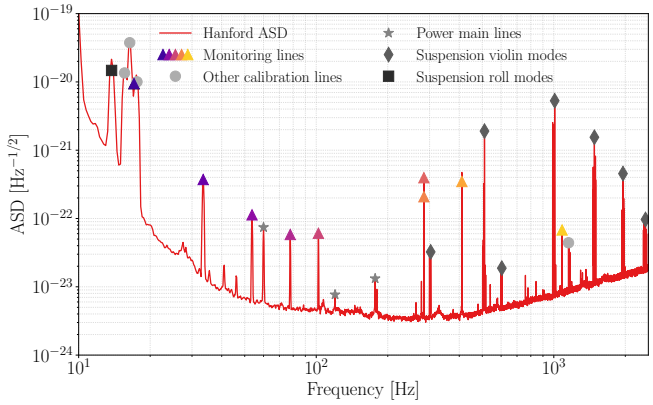

FIG. 5. ASD of the LIGO Hanford detector one day before the arrival of GW240925. Colored triangles indicate the calibration monitoring lines used for real-time tracking of the detector response. Dots, stars, diamonds and squares mark the additional calibration tracking lines for time-dependent correction factors, power mains, suspension violin harmonics and suspension roll modes, respectively.

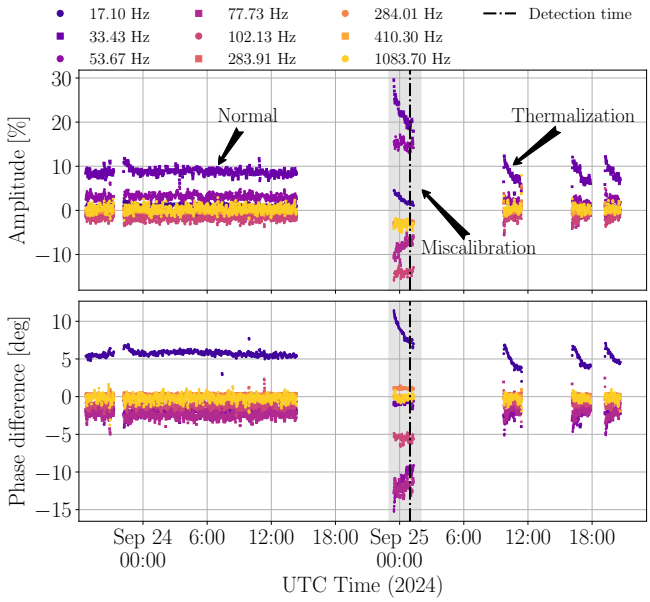

FIG. 6. Real-time calibration monitoring for Hanford around the time of GW240925 (spanning ~ 2 days). The top and bottom panels show the estimated amplitude and phase of the calibration error, $\delta\mathcal{A}$ and $\delta\phi$, respectively, expressed through the complex correction factor η. The shaded region highlights the miscalibrated interval.

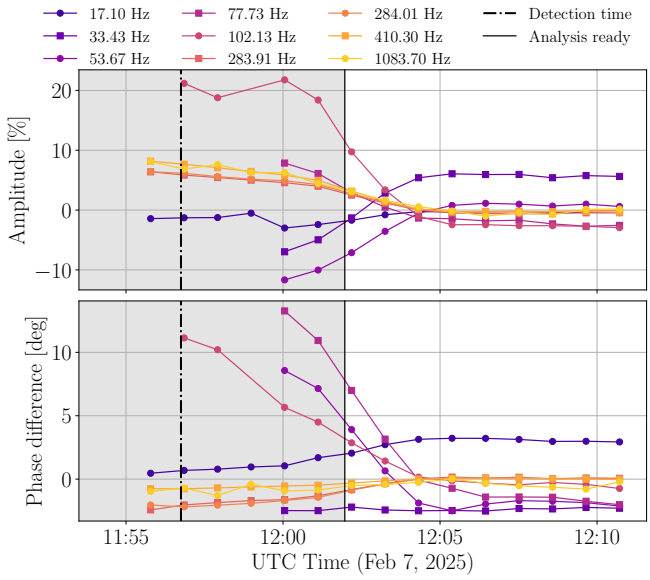

FIG. 7. Similar to Fig. 6, real-time calibration monitoring for Hanford around the time of GW250207 (zoomed in to the detection and observing starting times). The shaded region marks the interval during which the detector had not yet reached analysis-ready observing status.

parameters, uncompensated time dependencies, or missing features present in the true detector response. The probability distribution of the correction factor $\eta(f;t)$ is evaluated hourly throughout the observing run by incorporating both in-situ regular measurements taken when the detector is not observing (typically once or twice per week) and real-time measurements within a one-hour window [42]. This distribution is constructed numerically using 10^3 realizations of $R(f;t)$ [15, 16]. The resulting uncertainty envelope is used to construct the calibration prior employed in signal parameter estimation for all candidates whose trigger time lies closest to the given hour $t_{\rm near}$ [43].

In addition to the procedures adopted during the early observing runs [14, 15, 34], a real-time monitoring system was introduced in Virgo during the third observing run (O3) [17] and in LIGO during O4 [42] to improve the evaluation of $\eta(f;t)$ in the low-latency calibrated data. This system operates by continuously injecting monochromatic calibration lines at discrete frequencies (nine lines for LIGO) via the photon calibrator [38–41]. These lines enable direct measurement of the detector response at their respective frequencies. Figure 5 shows the locations and relative strengths of these lines in the amplitude spectral density (ASD) of Hanford detector data. Two closely spaced lines at 283.91 Hz and 284.01 Hz are injected into the X- and Y-end test masses, respectively, to monitor the photon-calibrator absolute references [42]. For Virgo, absolute calibration was further improved through the deployment of a Newtonian calibrator, which provides a precise reference at low frequencies [185]. The detector response to these injected lines is continuously measured in real time, allowing direct inference of $\eta(f;t)$ at those frequencies.

Figures 6 and 7 show the real-time calibration monitoring measurements for the Hanford detector response function around the times of GW240925 and GW250207, respectively [42]. These figures show the estimated amplitude and phase errors derived from the monitoring lines at their respective frequencies. These diagnostics help assess the calibration accuracy during the periods of interest.

For GW240925, Fig. 6 spans ~ 2 days to illustrate three

representative periods of detector behavior: (i) a normal period on the day before the signal, during which the measured calibration amplitude and phase errors are within $|\delta\mathcal{A}| \lesssim 10\%$ and $|\delta\phi| \lesssim 6$ deg; (ii) a miscalibrated interval, where the measurements deviate significantly from $\delta\mathcal{A} = 0$ and $\delta\phi = 0$ deg, indicating a known calibration issue, and (iii) several short-duration lock stretches lasting $\lesssim 2$ h, where low-frequency evolution due to *thermalization* effects (time-varying lensing by the test masses due to differential heating by the laser beam profile) is evident, e.g., in the amplitude at 33.43 Hz and in the phase at 17.10 Hz.

For GW250207, Fig. 7 is zoomed in around the detection. The shaded region marks the interval when the detector had not yet reached observing status and was undergoing thermalization, as indicated by larger deviations from $\delta\mathcal{A} = 0$ and $\delta\phi = 0$ deg at various frequencies. The calibration is best modeled when the interferometer is fully thermalized and operating in a steady state. Several monitoring lines were also not yet recording measurements during this period.

With real-time monitoring and hourly evaluation of systematic errors, similarly elevated calibration errors to those seen around these two detections are not observed in other observing-mode stretches of O4 [36].

EVENT VALIDATION

Detector data can be impacted by noise of instrumental or environmental origin [186–188]. Noise artifacts can manifest in several ways, such as shorter-duration, broadband non-Gaussian features known as *glitches* [67, 68], and narrowband features known as *spectral lines* [189]. DQ vetting around candidate events involves multiple checks [66], such as event validation, the DQ Report (DQR) [190, 191], and (when needed) glitch subtraction [192–194].

GW240925 was detected while Livingston was observing with binary neutron star inspiral range (a conventional measure of detector sensitivity [5, 195, 196]) of $\sim$ 168 Mpc, Virgo was observing with range $\sim$ 51 Mpc, and Hanford was observing with an estimated range of $\sim$ 147 Mpc, neglecting its calibration uncertainty. During event validation, some components of the DQR were flagged for investigation. At both Hanford and Livingston, excess noise was identified in an auxiliary channel that monitors environmental noise [152]; however, this noise occurred at sufficiently high frequencies to be well separated from the GW signal band, and we found no evidence that it coupled into the GW strain during the times of interest. In addition, a glitch was identified in Livingston data 1.4–1.7 s after the signal in the frequency range 25–50 Hz. The glitch occurred sufficiently far from the signal that it does not impact the inference of source properties [69]. Thus, glitch mitigation was deemed unnecessary. Overall, no DQ issues impacting the observation were found for any of the detectors.

Approximately 80 s of Hanford strain data preceding the time of GW240925 were initially marked as non-observing, as the interferometer was briefly taken out of observing mode to make a digital configuration change to a control loop that is a part of the arm-length stabilization system. This stabilization system is inactive when the detector is in a low-noise state and only used during lock acquisition. The configuration-change procedure had no impact on the strain data, which remain valid for analysis during that interval [45].

GW250207 was detected while Livingston and Virgo were observing with binary neutron star inspiral ranges of $\sim$ 168 Mpc and $\sim$ 51 Mpc, respectively; Hanford formally entered observing mode with a range of $\sim$ 149 Mpc approximately five minutes later. During event validation, one DQR task that monitors auxiliary channels for excess noise overlapping the signal [150] was flagged for investigation. As with GW240925, no DQ issues were identified for any of the detectors, as no excess noise was found in the strain data during the time of interest.

ADDITIONAL SEARCH-ANALYSIS RESULTS

Multiple search pipelines are used to search for CBC signals [43], for both low-latency, online analyses and higher-latency, offline analyses. Online searches prioritize rapid identification of candidates for prompt alerts to the astronomical community [94, 197], whereas offline searches are performed later to provide more comprehensive results. The offline searches can analyze recalibrated data, incorporate updated DQ information, and use more computationally expensive algorithms [43]. While online searches evaluate candidate significance using background data collected only prior to the candidate, offline searches can use data from both before and after the candidate time. As a result, marginal candidates can vary in significance between online and offline analyses, while highly significant candidates generally remain so [6]. High-SNR candidates are typically recovered as significant across all pipelines [43, 94].

GW240925 was identified in low-latency by cWB [47–50], GstLAL [51–59], MBTA [60–62] and SPIIR [63]. The PyCBC search pipeline [198] did not report the candidate in low latency because there were insufficient contiguous observing-mode data to identify a Hanford trigger, and it only considers single-detector candidates with potential electromagnetic counterparts (a duration > 7 s) [43, 198]. Nevertheless, PyCBC did recover a trigger with consistent SNR and timestamp in Livingston.

GW250207 was identified in low latency by GstLAL and SPIIR. The other low-latency search pipelines did not report the candidate because they did not account for Virgo triggers when constructing multi-detector coincidences, and they were configured to either require at least two-detector coincidence (for cWB [49, 50]) or only report single-detector candidates likely to accompany electromagnetic emissions [43] (e.g., a detector-frame chirp mass below $7M_\odot$ for MBTA [62]). Nevertheless, both MBTA and PyCBC recovered a trigger with consistent SNR and timestamp in Livingston.

TABLE II. Offline search results for GW240925. The table lists the SNR in the LIGO Hanford and Livingston detectors and the FAR reported by each pipeline. The FARs are capped at $< 1 \times 10^{-5}$ yr^{-1} to ensure a consistent limit across pipelines.

Pipeline	$\rho_{\rm H}$	$\rho_{\rm L}$	FAR/yr^{-1}
GstLAL	16.8	25.5	$< 1 \times 10^{-5}$
MBTA	17.3	25.8	$< 1 \times 10^{-5}$
PyCBC	17.3	25.7	3.95×10^{-5}

Full offline search results for O4b will be presented in GWTC-5.0, with results for O4c to follow in GWTC-6.0 [5]. In Table II, we present the currently available offline results for GW240925, analyzed with the GstLAL [51–55, 57–59], MBTA [60–62] and PyCBC [157, 158, 199] matched-filter pipelines using the C00 data. To assess the potential impact of miscalibration on the search results, we also analyzed the C01 data with the MBTA and PyCBC pipelines, and found that the SNR and 90% credible area of the sky localization differed by only a few percent relative to the C00 results. This suggests that the Hanford miscalibration did not significantly affect the search results for GW240925, which is consistent with expectations [37, 200, 201].

PARAMETER-ESTIMATION METHODS AND RESULTS

To characterize each signal, we use the Dynesty nested sampler [166], as implemented in the Bilby Bayesian inference library [70, 71], to obtain samples from the posterior probability distributions of both the source and calibration parameters. Changing these parameters alters the waveform: for example, varying the chirp mass changes the frequency evolution of the inspiral [11, 76, 202]. Hence, we calculate the posterior probability distribution for the input parameters by assessing how well the corresponding waveform matches the data [74, 203].

Both signals were observed in the Hanford, Livingston and Virgo detectors, and we coherently analyze data from all three [74] (except when investigating the potential to constrain calibration with Hanford data alone). For GW240925, we analyze 32 s of data employing a sampling frequency of 4096 Hz, with a frequency range from 20 Hz to 1792 Hz. For GW250207, we analyze 8 s of data employing a sampling frequency of 1024 Hz, with a frequency range of 20 Hz to 448 Hz. For both signals, estimates of the detectors' power spectral densities (PSDs) are obtained using BayesWave [163, 165, 204].

The strain data consist of the GW signal and detector noise, $d^{(\rm corr)} = h(\boldsymbol{\theta}) + n^{(\rm corr)}$, where $h(\boldsymbol{\theta})$ is the waveform corresponding to parameters $\boldsymbol{\theta}$, and $n^{(\rm corr)}$ is the residual noise after applying the calibration correction. To account for calibration uncertainties in the inference, we apply the calibration correction factor η to the waveform model rather than the detector data:

$$d = \frac{d^{(\rm corr)}}{\eta} = \frac{1}{\eta}\left(h + n^{(\rm corr)}\right) = \frac{h}{\eta} + n, \tag{5}$$

where $n = n^{(\rm corr)}/\eta$ is the effective noise without applying the calibration correction. Since the likelihood is a function of d, rather than $d^{(\rm corr)}$, and the PSD characterizes n, not $n^{(\rm corr)}$, applying the calibration correction to the waveform is the more convenient approach [43].

We parametrize the calibration uncertainty in the inference as

$$\frac{1}{\eta(f; t_{\rm near})} = \left[1 + \delta\mathcal{A}'(f)\right] \exp\left[i\delta\phi'(f)\right], \tag{6}$$

where $\delta\mathcal{A}'(f)$ and $\delta\phi'(f)$ are the amplitude and phase deviation parameters, respectively [72]. The frequency-dependent amplitude and phase corrections are modeled using cubic splines [43, 73, 74]. The deviation parameters are related to the calibration errors defined in Eq. (1) of the main paper as

$$\delta\phi'(f) = -\delta\phi(f; t_{\rm near}); \quad 1 + \delta\mathcal{A}'(f) = \frac{1}{1 + \delta\mathcal{A}(f; t_{\rm near})}. \tag{7}$$

The in-situ measured calibration uncertainty estimates provide the distribution of $\{[1 + \delta\mathcal{A}(f; t_{\rm near})], \delta\phi(f; t_{\rm near})\}$ at discrete frequencies. These are converted to $\{[1 + \delta\mathcal{A}'(f)], \delta\phi'(f)\}$ and interpolated to a set of 10 frequency nodes with log-uniform spacing over the analysis frequency range for each detector. Gaussian priors are then set on $\delta\mathcal{A}'(f)$ and $\delta\phi'(f)$ at each node frequency, with medians and standard deviations determined from the in-situ measurements.

For the analysis of GW240925, we use three different IMR waveform models, all of which include the effects of spin precession and higher-order multipole moments, while neglecting orbital eccentricity: the frequency-domain IMRPhenomXPHM [205, 206] and IMRPhenomXPNR [207, 208], and the time-domain SEOBNRv5PHM [209, 210], which additionally includes equatorial asymmetric contributions to multipole moments. For the analysis of GW250207, we use the same three models as for GW240925, and additionally include NRSur7dq4 [139], a time-domain numerical-relativity surrogate model. This model cannot be used for GW240925 due to constraints on the mass range over which it can generate waveforms down to 20 Hz. We also perform an analysis with the frequency-domain IMRPhenomXAS waveform [211], which assumes aligned spins, thereby excluding orbital-plane precession effects, and includes only the contribution from the dominant $(2, 2)$ multipole. This waveform is included for comparison with results from the search pipelines, which use waveforms incorporating similar physics. Our overall parameter estimates for both signals are obtained by combining results from a set of the different waveform models that include the effects of spin precession with equal weight (excluding IMRPhenomXAS) [43, 74]; since IMRPhenomXPNR supersedes IMRPhenomXPHM, the latter is excluded from the combination to avoid double-counting the results obtained with this waveform family.

For both signals, we adopt default priors for the source parameters: a uniform prior on detector-frame component masses, with bounds on the detector-frame chirp mass wide enough to avoid truncating the posterior; a uniform prior on spin magnitudes with isotropic spin directions; uniform priors on the reference phase and time; a uniform distribution on the polarization angle; a uniform distribution over the sphere for binary inclination; a uniform distribution over the sky for sky position, and a distance prior corresponding to a uniform distribution in comoving time and volume [43, 71, 212]. For analyses using IMRPhenomXAS, which neglect spin precession, we adopt a prior on the spin magnitudes that gives the same distribution for spin components aligned with the orbital angular momentum as the prior used in the other analyses. For analyses of Hanford data where we assume a wide calibration prior, we do not use frequency-dependent in-situ measurements to set uncertainties for $\delta\mathcal{A}(f; t_{\rm near})$ and $\delta\phi(f; t_{\rm near})$, but instead assume zero-mean Gaussian uncertainties with frequency-independent standard deviations of 20% and 20 deg, respectively. These calibration uncertainty priors are sufficiently broad to encompass the miscalibrations present at the times of the two signals, as illustrated in Fig. 6 and Fig. 7.

Results from the various analyses of the two signals are given in Table III, with the inferred component masses shown in Fig. 8. In addition to the analyses described in the main text, we also provide results for GW240925 assuming perfect calibration in all three detectors, to assess potential biases arising from neglecting calibration uncertainties. In Fig. 9, we show the inferred spin parameters for GW250207, where the inclusion of calibration uncertainty leads to a difference for $\chi_{\rm p}$ but not $\chi_{\rm eff}$, illustrating how some signal properties and more sensitive to the calibration than others.

In contrast to the significant differences found for GW250207 discussed in the main text and shown in Fig. 9, for GW240925, neglecting calibration uncertainty leads to small shifts in most intrinsic parameters. For example, the detector-frame chirp mass is $(1+z)\mathcal{M} = 7.368^{+0.011}_{-0.009} M_\odot$ without incorporating calibration uncertainty, compared to $7.371^{+0.012}_{-0.010} M_\odot$ when using the wide calibration prior. The luminosity distance is inferred as $D_{\rm L} = 369^{+54}_{-156}$ Mpc when neglecting calibration uncertainty, shifted from 348^{+69}_{-160} Mpc with the wide calibration prior. The most significant impact is seen in the sky area [76], which increases from 22 deg^2 without incorporating calibration uncertainty to 60 deg^2 with the wide calibration prior, as illustrated in Fig. 10.

The source-mass distributions for GW240925 exhibit bimodality, as visible in the two-dimensional distributions of Fig. 8. The detector-frame masses have a unimodal distribution, but the distance distribution has two modes, which impacts the inferred source masses [5, 214]. The distance distribution has one mode at larger values (favored by the prior) corresponding to face-on inclinations, and another at smaller values corresponding to edge-on inclinations [215–217]. For edge-on inclinations, the signal is dominated by a single polarization component [11, 218, 219]. While the two LIGO detectors are approximately aligned, and so have similar sensitivities to signal polarization [5, 220, 221], Virgo has a different sensitivity [222, 223]. Hence with edge-on inclinations, the polarization can be adjusted to an alignment that Virgo is less sensitive to, and this accounts for the disparate SNRs measured in the Virgo and LIGO detectors (the inferred Virgo SNR is $\rho_{\rm V} = 1.9^{+0.2}_{-0.7}$ versus $\rho_{\rm L} = 26.46^{+0.11}_{-0.13}$ in Livingston). Similar to the sky localization of GW170817 [224], this illustrates how multi-detector observations can constrain source properties even when SNR is low in one detector.

We find that systematic differences from the choice of waveform model are small for both signals, as typical JSDs between the intrinsic parameter posteriors obtained with different waveforms are $O(0.01)$ nat. The most significant variations appear in parameters that are defined differently between the waveform families, like azimuthal angles and coalescence time. The differences in the posteriors for the calibration parameters are generally smaller than those found for the intrinsic binary parameters; however, larger differences between the calibration-parameter posteriors obtained with the various waveforms are found when using the wide priors than when using the more constraining in-situ envelope priors. Given the properties of the sources, it is expected that the different waveform models should give consistent results [6].

We expect constraints on the calibration to improve with increasing SNR. Low-SNR signals will have posteriors dominated by the prior, while the likelihood becomes more dominant at high SNRs [19, 26]. From Fig. 2 of the main paper, we can see that constraints from GW250207 are often tighter than for GW240925, but that depends on the frequency. Since the frequency contents of the signals differ, they provide different amounts of information about the calibration parameters as a function of frequency. If we examine the constraints around physically comparable frequencies corresponding to the minimum-energy circular orbit $f_{22}^{\rm MECO}$ for the two signals, for GW240925 we infer $\delta\mathcal{A} = -7^{+27}_{-18}\%$ and $\delta\phi = -4^{+19}_{-19}$ deg (90% credible interval) at the spline node at 243.0 Hz, while for GW250207 we infer $\delta\mathcal{A} = -16^{+10}_{-9}\%$ and $\delta\phi = 7^{+8}_{-8}$ deg at the spline node at 56.4 Hz. These constraints are tighter for GW250207. In general, the measurement precision will depend upon both the SNR in the relevant detector, and the network SNR, which governs how well source properties can be determined [11–13, 27, 28].

To assess potential correlations between the inferred source and calibration parameters, we calculate the Pearson correlation coefficient (PCC) [225] between each source parameter and the frequency-dependent amplitude and phase calibration parameters. We find no significant correlations for GW240925 (PCC < 0.3). For the coherent, multi-detector analyses of GW250207, we find that the calibration phase corrections are correlated with both the sky position and polarization, while the calibration amplitude corrections are correlated with the inclination and luminosity distance, with PCC > 0.4 in both cases. For the single-detector, Hanford-only analysis, the calibration amplitude corrections show correlations with the inferred chirp mass and reference time, since the lumi-

TABLE III. Inferred source properties for GW240925 and GW250207. We report median values with 90% symmetric credible intervals from various analyses for various parameters [5], and the 90% credible area for the sky location. Four GW240925 analyses are presented: using the initial calibration of the data and assuming all three detectors are perfectly calibrated (C00 no uncertainty); assuming a wide, uninformative prior for Hanford calibration and the in-situ measured uncertainty envelopes for the other detectors (C00 wide); assuming the in-situ measured uncertainty envelopes for all detectors (C00 envelope), and using recalibrated data assuming the in-situ measured uncertainty envelopes for all detectors (C01 envelope). Two GW250207 analyses are presented: assuming all three detectors are perfectly calibrated (C00 no uncertainty), and assuming a wide, uninformative prior for Hanford calibration and the in-situ measured uncertainty envelopes for the other detectors (C00 wide). The analyses that neglect calibration uncertainty are expected to yield biased results. Parameters that evolve throughout the inspiral are quoted at a reference frequency of 20 Hz. All results are computed assuming a standard cosmology with $H_0 = 67.9\,\mathrm{km\,s^{-1}\,Mpc^{-1}}$ [43, 81].

	GW240925				GW250207	
Parameter	C00 no uncertainty	C00 wide	C00 envelope	C01 envelope	C00 no uncertainty	C00 wide
Primary mass $m_1/M_\odot$	$9.0^{+1.8}_{-1.0}$	$9.0^{+1.8}_{-1.0}$	$9.0^{+1.7}_{-1.0}$	$9.0^{+2.0}_{-1.0}$	$35.4^{+1.4}_{-1.4}$	$35.2^{+1.7}_{-1.7}$
Secondary mass $m_2/M_\odot$	$6.9^{+0.9}_{-1.1}$	$7.0^{+0.8}_{-1.2}$	$7.0^{+0.8}_{-1.2}$	$7.0^{+0.8}_{-1.3}$	$30.5^{+1.3}_{-1.2}$	$30.6^{+1.5}_{-1.8}$
Total mass $M/M_\odot$	$16.0^{+0.7}_{-0.4}$	$16.1^{+0.6}_{-0.5}$	$16.1^{+0.6}_{-0.4}$	$16.1^{+0.7}_{-0.4}$	$66.0^{+0.8}_{-1.1}$	$65.9^{+1.0}_{-1.7}$
Chirp mass $\mathcal{M}/M_\odot$	$6.83^{+0.21}_{-0.07}$	$6.86^{+0.22}_{-0.09}$	$6.85^{+0.22}_{-0.08}$	$6.85^{+0.22}_{-0.08}$	$28.61^{+0.35}_{-0.46}$	$28.57^{+0.44}_{-0.77}$
Final mass $M_\mathrm{f}/M_\odot$	$15.2^{+0.7}_{-0.4}$	$15.3^{+0.7}_{-0.5}$	$15.3^{+0.6}_{-0.4}$	$15.3^{+0.7}_{-0.4}$	$62.8^{+0.7}_{-1.0}$	$62.7^{+1.0}_{-1.6}$
Effective inspiral spin χ_eff	$0.02^{+0.07}_{-0.02}$	$0.03^{+0.07}_{-0.02}$	$0.02^{+0.07}_{-0.02}$	$0.02^{+0.08}_{-0.02}$	$-0.00^{+0.03}_{-0.04}$	$0.00^{+0.03}_{-0.04}$
Effective precession spin χ_p	$0.22^{+0.31}_{-0.18}$	$0.26^{+0.37}_{-0.21}$	$0.25^{+0.39}_{-0.20}$	$0.25^{+0.37}_{-0.20}$	$0.13^{+0.17}_{-0.07}$	$0.06^{+0.15}_{-0.05}$
Final spin χ_f	$0.69^{+0.01}_{-0.03}$	$0.69^{+0.02}_{-0.03}$	$0.69^{+0.02}_{-0.02}$	$0.69^{+0.02}_{-0.03}$	$0.68^{+0.01}_{-0.01}$	$0.69^{+0.01}_{-0.01}$
Luminosity distance D_L/Mpc	369^{+54}_{-156}	348^{+69}_{-160}	355^{+63}_{-165}	356^{+61}_{-162}	175^{+42}_{-28}	187^{+121}_{-52}
Redshift z	$0.08^{+0.01}_{-0.03}$	$0.07^{+0.01}_{-0.03}$	$0.08^{+0.01}_{-0.03}$	$0.08^{+0.01}_{-0.03}$	$0.04^{+0.01}_{-0.01}$	$0.04^{+0.03}_{-0.01}$
Network SNR ρ	$31.34^{+0.10}_{-0.14}$	$31.44^{+0.16}_{-0.20}$	$31.50^{+0.11}_{-0.16}$	$31.96^{+0.11}_{-0.15}$	$68.66^{+0.05}_{-0.08}$	$68.91^{+0.08}_{-0.11}$
Hanford SNR ρ_H	$17.58^{+0.09}_{-0.14}$	$17.75^{+0.18}_{-0.25}$	$17.82^{+0.09}_{-0.13}$	$17.95^{+0.08}_{-0.13}$	$48.55^{+0.10}_{-0.11}$	$48.81^{+0.08}_{-0.11}$
Livingston SNR ρ_L	$25.98^{+0.11}_{-0.13}$	$25.99^{+0.12}_{-0.14}$	$25.99^{+0.11}_{-0.13}$	$26.46^{+0.11}_{-0.13}$	$47.90^{+0.08}_{-0.10}$	$48.00^{+0.05}_{-0.07}$
Virgo SNR ρ_V	$1.9^{+0.1}_{-0.5}$	$1.9^{+0.2}_{-0.8}$	$1.9^{+0.2}_{-0.8}$	$1.9^{+0.2}_{-0.7}$	$8.2^{+0.2}_{-0.4}$	$8.1^{+0.3}_{-0.6}$
Sky area Ω/deg^2	22	60	29	25	5	20

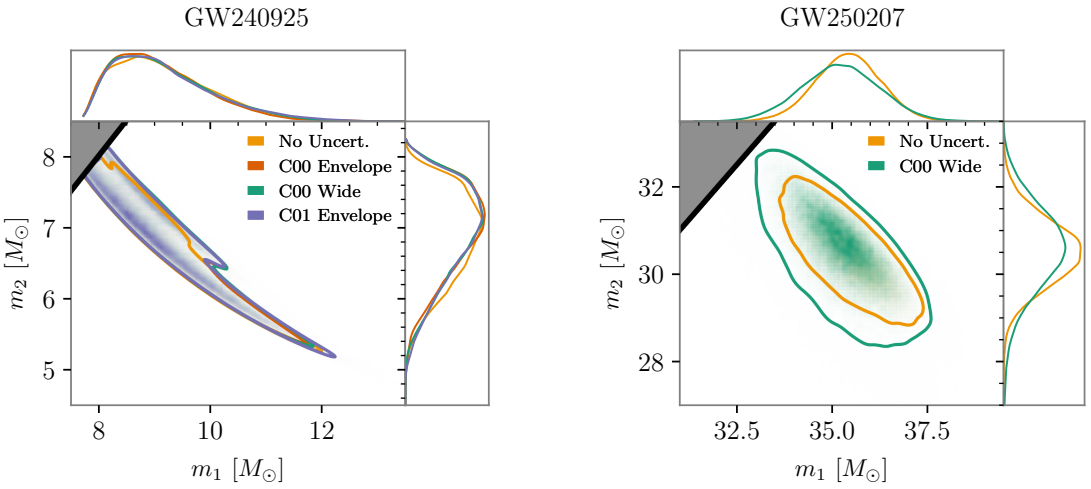

FIG. 8. Inferred component masses for GW240925 (left) and GW250207 (right). Results are shown for analyses that neglect calibration uncertainty (yellow) and that adopt a wide prior on the Hanford calibration (green), for both signals. For GW240925, we additionally show results using the in-situ measured calibration priors applied to the Hanford miscalibrated C00 (orange) and recalibrated C01 (purple) data. The component masses follow the convention that $m_1 \geq m_2$. Two-dimensional plots show the joint posterior probability densities with 90% credible contours; one-dimensional plots show the corresponding marginalized posteriors.

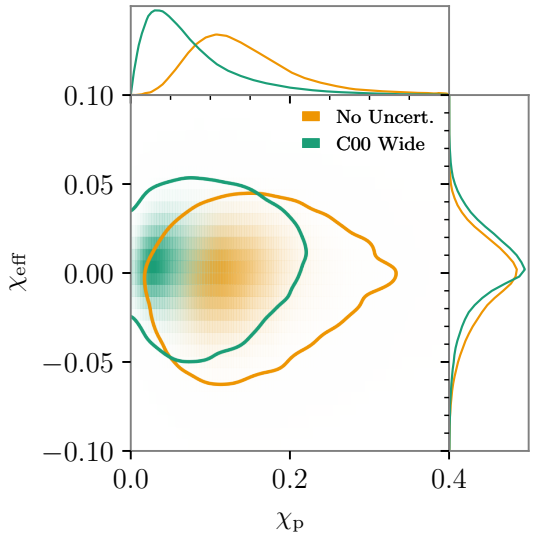

FIG. 9. Inferred effective inspiral spin $\chi_{\rm eff}$ and effective precession spin $\chi_{\rm p}$ for GW250207 under two different calibration prior assumptions. Results are shown for analyses that neglect calibration uncertainty (yellow) and that adopt a wide prior on the Hanford calibration (green). Two-dimensional plots show the joint posterior probability densities with 90% credible contours; one-dimensional plots show the corresponding marginalized posteriors. While the inferred $\chi_{\rm eff}$ is similar in both cases, neglecting to account for calibration uncertainty leads to a shift in the $\chi_{\rm p}$ posterior that erroneously ascribes the effect of miscalibration to spin precession in the signal.

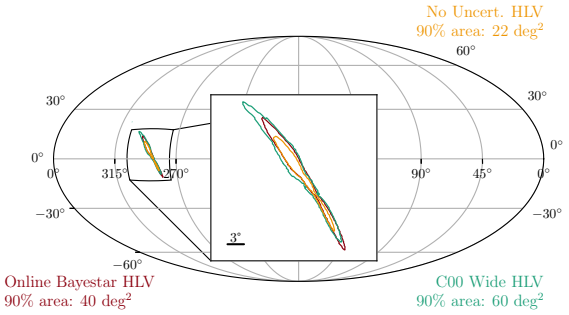

FIG. 10. Sky localization for GW240925 from the low-latency BAYESTAR analysis (which does not account for calibration uncertainty) [213], and Bilby analyses including and excluding calibration uncertainty. All analyses use data from Hanford, Livingston and Virgo. While including calibration uncertainty broadens the localization, failing to marginalize over calibration uncertainty may lead to biased results in the presence of significant miscalibration.

nosity distance posterior is more prior driven for the single-detector analysis.

We also investigate the cause of the inconsistency between the Livingston–Virgo and three-detector sky localizations. The effect of including Hanford data is illustrated in Fig. 11, which shows the posteriors on the sky location and time delays between detector pairs for both the two- and three-detector analyses for each signal. For GW240925, the two-detector sky localization has multiple modes, each corresponding to a different Livingston–Virgo time delay. The low Virgo SNR means that there is posterior support for time delays corresponding to offsets of approximately a GW cycle [226]. Adding Hanford data adds significant extra information to the analysis, resulting in a change in the localization [103, 104]. The three-detector localization is primarily constrained by the Hanford–Livingston time delay, and the three-detector analysis selects one of the secondary modes for the Livingston–Virgo time delay from the two-detector analysis as most probable. The two-detector localization does have some posterior support at the sky location identified in the three-detector analysis, but this is outside of the 90% credible area. For GW250207, the two-detector localization exhibits two separate modes, although again only the primary mode falls within the 90% credible area. The secondary mode corresponds to a much closer inferred distance than the primary mode and is therefore downweighted by the prior in the two-detector analysis. However, adding Hanford data shifts the localization around the ring of constant Livingston–Virgo time delay, to a point consistent with the observed Hanford time; the additional constraint on the timing overcomes the prior suppression of the secondary mode, which then becomes the preferred source location. The precise sky localization obtained with the inclusion of Hanford data for both signals was enabled by the simultaneous inference of the calibration parameters in the parameter-estimation analyses.

Another source of the discrepancy between the low-latency BAYESTAR localization and the offline Bilby results arises from differences in the physical effects included in the waveform models underlying each analysis. The search pipelines that produce the matched-filter SNR time series used by BAYESTAR include only aligned-spin effects and GW emission from the dominant $(2, 2)$ multipole moment, analogous to the IMRPhenomXAS Bilby analyses. They also assume that the data are perfectly calibrated. In Fig. 12, we show how the three-detector sky localization for GW250207 changes when these assumptions are relaxed in full parameter-estimation analyses. The inclusion of higher-order multipole moments and precession effects, which are better measured with three detectors than with two, leads to an improvement in the sky localization relative to analyses using waveforms that only model the dominant $(2, 2)$-multipole emission and aligned spins. Finally, marginalizing over calibration uncertainty broadens the sky localization.

CONSISTENCY TESTS

Analyses that test the consistency of GW signals with GR predictions can reveal potential errors in the underlying assumptions, whether due to deviations from GR, missing physics in waveform models, mismodeling of the noise, or miscalibration of the data [23, 100, 113]. Different tests are complementary, since they probe different types of devia-

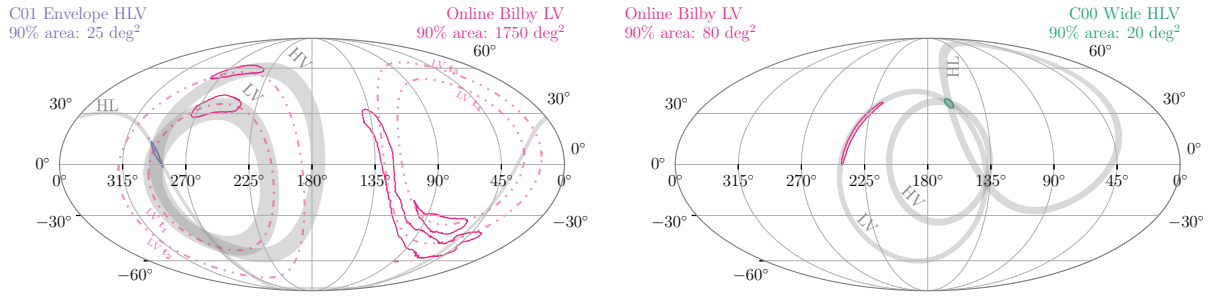

FIG. 11. Posteriors on the sky location together with rings corresponding to the inferred time delays between detector pairs for GW240925 (left) and GW250207 (right). Solid curves enclose the 90% credible areas for the two-detector (Livingston–Virgo; LV) [77, 82] and three-detector (HLV) analyses. The grey bands represent 90% credible intervals for time delays from the three-detector analyses; the three-detector localizations lie at intersections of these bands. For GW240925, the two-detector analysis produces a multimodal posterior distribution for the LV time delay, and the dot–dashed rings illustrate the approximate positions of its peaks. The time delay t_1 is selected by the three-detector analysis through consistency with the Hanford–Livingston (HL) and Hanford–Virgo (HV) time delays. For GW250207, the two- and three-detector analysis lie on a ring of consistent LV time delay. For both signals, inclusion of Hanford data improves the time-delay constraints and shifts the sky-location posterior distributions.

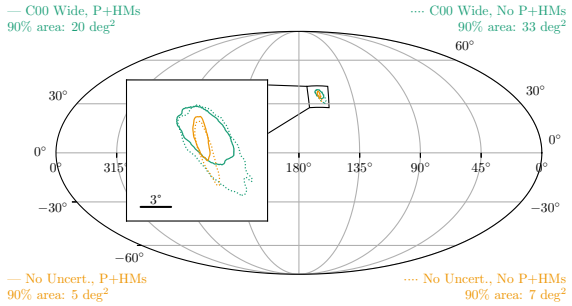

FIG. 12. Sky localization for GW250207 from four different Bilby analyses using data from Hanford, Livingston and Virgo. We show results from analyses with and without (solid and dotted lines, respectively) the inclusion of spin-precession effects and higher-order multipole moments (P+HMs), and that incorporate or neglect calibration uncertainties (green and yellow, respectively).

tions [114]. We perform a set of tests to search for inconsistencies in the signal modeling, DQ and detector calibration.

Residual tests

The residuals test examines the data for excess coherent power remaining in the detector network after subtracting a best-fit waveform [113–115]. Significant residual power may indicate additional physical effects beyond those captured by BBH waveform models, alternative physics, unmodeled calibration systematic errors or instrumental noise artifacts.

The residual data are obtained by subtracting the maximum-likelihood waveform, inferred from the parameter estimation, from the original data. If the waveform model adequately captures the GW signal, the resulting residuals should be consistent with stationary Gaussian noise. We analyze the residual data using BayesWave [163–165] and compute the 90% credible upper limit on the network SNR, denoted ρ_{90}. To assess the significance of the obtained ρ_{90}, we also analyze nearby segments of detector data around the signal (without simulated signals) to estimate the background distribution. The probability of obtaining a ρ_{90} higher than or equal to that calculated from the residual data is reported as the p-value, $P(\rho^n_{90} \geq \rho_{90})$, where ρ^n_{90} is the 90% credible upper limit on the coherent network SNR from the noise-only background segments. A higher p-value indicates that the residual power is likely to originate from instrumental noise. For a single signal consistent with GR, the p-value is expected to follow a uniform distribution on the interval $(0, 1]$ [113]. The goodness-of-fit of the GR-based waveform to the data can also be quantified by calculating the 90% credible lower limit on the fitting factor:

$$\mathrm{FF}_{90} = \rho_{\mathrm{GR}}\left(\rho^2_{\mathrm{GR}} + \rho^2_{90}\right)^{-1/2}, \tag{8}$$

where ρ_{GR} is the optimal network SNR for the maximum-likelihood waveform, and a value of $\mathrm{FF}_{90} = 1$ indicates perfect agreement between the waveform and the data [113].

We compute residuals using the C00 strain data, $r(t) = d_{\mathrm{C00}}(t) - h_{\mathrm{ML}}(t)/\eta$, where $1/\eta$ is the median calibration correction factor inferred from parameter estimation, and $h_{\mathrm{ML}}(t)$ is the maximum-likelihood waveform. In analyses where calibration parameters are not inferred, the residuals are computed in the standard way as $r(t) = d_{\mathrm{C00}}(t) - h_{\mathrm{ML}}(t)$. We show the results in Fig. 13.

For GW240925, when calibration effects are not included in the analysis, $\rho_{90} = 7.2$ with a p-value of 0.26 and $\mathrm{FF}_{90} = 0.97$. When the residuals are computed using the calibration correction factor from the wide prior analysis, $\rho_{90} = 7.2$ with a p-value of 0.30 and $\mathrm{FF}_{90} = 0.97$. These ρ_{90} values fall within the range reported in analyses of previous detections [115]. The top two panels of Fig. 13 show the residuals for these two cases. No excess residual power can be identified, and these results remain consistent with the expectation for Gaussian

noise, regardless of the calibration treatment.

For GW250207, $\rho_{90} = 7.2$ with a p-value of 0.28 and $\mathrm{FF}_{90} = 0.99$ when calibration effects are neglected, and $\rho_{90} = 7.6$ with a p-value of 0.19 and $\mathrm{FF}_{90} = 0.99$ when the calibration correction factor from the wide prior analysis is applied. The corresponding residuals are shown in the bottom two panels of Fig. 13. Although the Hanford residuals appear to exhibit visible excess power in both cases, the results are consistent with expectations for Gaussian noise. We confirm that there is no correlation between these peaks and environmental monitors. We further investigate the residuals in Hanford by performing the Anderson–Darling test on a 1 s segment of the residual data centered on the search-analysis trigger time. We then compute a p-value for this statistic against the background segments. Both cases result in an equal Anderson–Darling statistic of 1.07, with a p-value of 0.98. These results indicate that the residuals are consistent with Gaussian noise.

Parametrized tests

The parametrized tests modify the signal waveforms by introducing parametrized deviations away from the GR model [125]. Modifying the waveform in this case is not expected to reproduce a signal in an alternative theory of gravity, but the additional flexibility in the waveform may identify phenomena such as missing physics in the waveform or an issue with DQ [23, 100, 119, 227]. Calibration errors could potentially mimic or mask the parametrized deviations considered here; hence, we expect that biases may result from miscalibration. However, as waveform modifications produce coherent effects across the detector network, while calibration errors affect each detector independently, the impact of miscalibration may not lead to an observable effect [228].

We study the impact of calibration uncertainties on the FTI test [116], which examines deviations in the PN coefficients during the inspiral phase. To assess this, we perform analyses both with and without marginalization over calibration uncertainties for each signal; in the latter case, we assume the data are perfectly calibrated. The analyses adopt the same settings and calibration priors as those used for the inference of source properties. We use the aligned-spin SEOBNRv5HM_ROM waveform model [229] as the GR baseline and allow a single PN deviation parameter to vary at a time.

For both signals, the FTI results are all consistent with their GR values. When calibration uncertainty is not marginalized, the posteriors on the deviation parameters peak further from zero compared to the results obtained using the wide calibration prior. Marginalizing over the wide calibration prior also broadens the posteriors on the deviation parameters. Figure 14 shows the GW250207 results for $\delta\hat{\varphi}_0$ as a representative example. The choice of calibration prior affects GW240925 less than GW250207; an illustrative example for GW240925 is shown in Fig. 14 with the $\delta\hat{\varphi}_7$ posteriors. The resulting constraints on the PN deviation parameters are summarized as 90% upper bounds in Table IV. Despite the wide calibration prior assumed for Hanford, the FTI bounds obtained for GW250207 on the 0PN, 1PN and higher-order PN coefficients are the most stringent achieved from GW observations to date [123–125]. Such tight constraints would not have been possible if the Hanford data were excluded from the analysis.

TABLE IV. The 90% upper bounds on the PN deviation parameters obtained with FTI and TIGER, as well as bounds on the post-inspiral deviation parameters from TIGER. Results are from analyses that use the in-situ measured calibration prior for Hanford in the case of GW240925 and a wide calibration prior for Hanford in the case of GW250207. If the GR waveform accurately models the signal and the data are accurately described by our analysis assumptions (well-calibrated data with stationary Gaussian noise), we expect the results to be statistically consistent with deviation values of zero; conversely, a deviation away from zero does not necessarily imply a modification of GR.

		GW240925		GW250207	
PN order	Parameter	FTI	TIGER	FTI	TIGER
−1	$\delta\hat{\varphi}_{-2}$	5.0×10^{-4}	5.8×10^{-4}	2.6×10^{-3}	3.0×10^{-3}
0	$\delta\hat{\varphi}_0$	0.085	0.20	0.034	0.05
0.5	$\delta\hat{\varphi}_1$	0.37	0.22	0.11	0.21
1	$\delta\hat{\varphi}_2$	0.17	0.14	0.056	0.13
1.5	$\delta\hat{\varphi}_3$	0.076	0.10	0.027	0.08
2	$\delta\hat{\varphi}_4$	0.36	0.88	0.14	0.59
2.5 log	$\delta\hat{\varphi}_{5l}$	0.088	0.33	0.037	0.20
3	$\delta\hat{\varphi}_6$	0.11	0.45	0.046	0.31
3 log	$\delta\hat{\varphi}_{6l}$	1.9	2.15	0.87	1.35
3.5	$\delta\hat{\varphi}_7$	0.22	1.15	0.088	0.88
Post-inspiral parameter		TIGER		TIGER	
$\delta\hat{b}_1$		0.04		0.03	
$\delta\hat{b}_2$		0.01		0.01	
$\delta\hat{b}_3$		0.01		0.01	
$\delta\hat{b}_4$		0.03		0.02	
$\delta\hat{c}_1$		0.84		0.25	
$\delta\hat{c}_2$		0.26		0.08	
$\delta\hat{c}_3$		0.75		0.24	
$\delta\hat{c}_\ell$		1.30		0.34	

We similarly assess the impact of calibration uncertainties on the TIGER test [120], which allows for deviations in both the inspiral PN coefficients and the phenomenological coefficients in the post-inspiral regime. Using the IMRPhenomXPHM waveform model [205, 206] as the GR baseline, we vary one deviation parameter at a time, repeating the analysis with and without calibration uncertainty. As in the FTI case, we find that including calibration uncertainties leads to broader posteriors and improved consistency with the GR values. In the analysis of GW250207, one of the merger–ringdown parameters ($\delta\hat{c}_\ell$, which scales the damping frequency of the ringdown signal) shows that the GR value falls outside the 90% credible interval when calibration uncertainties are neglected,

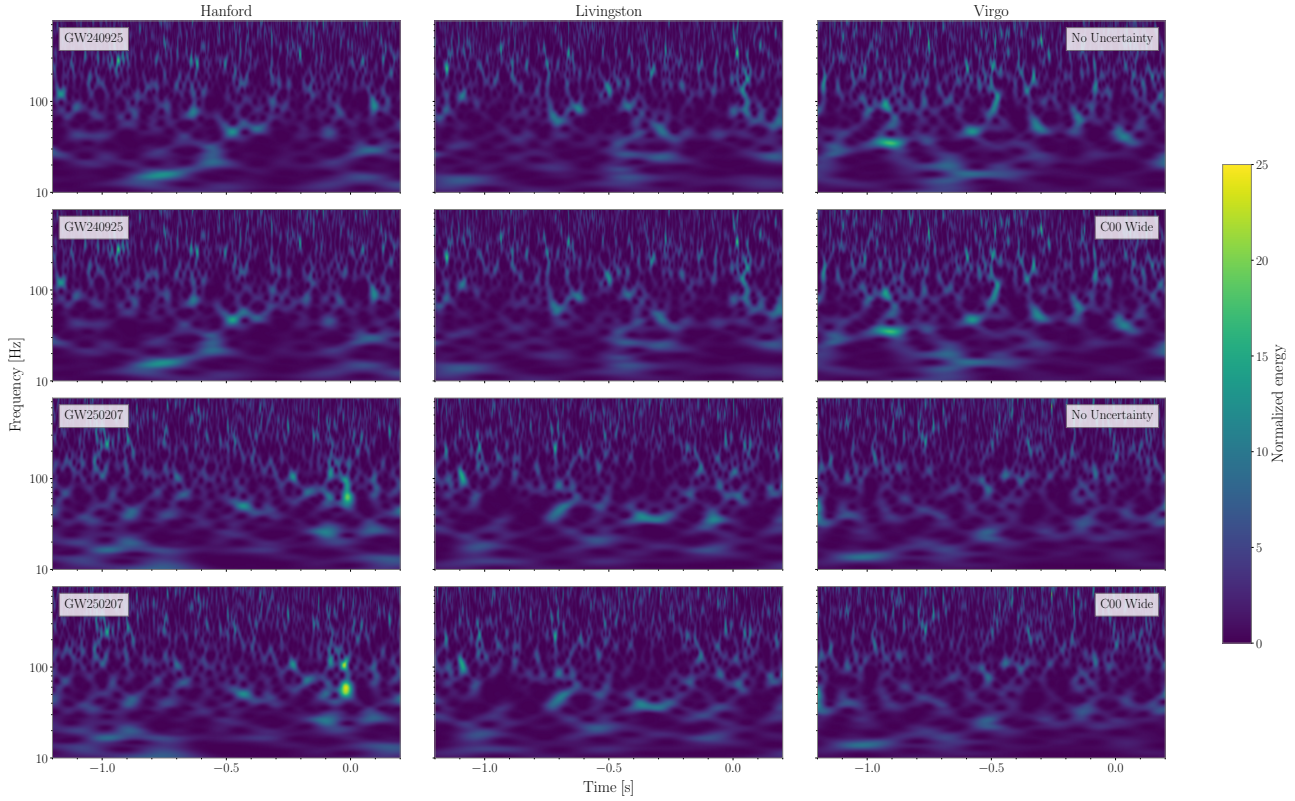

FIG. 13. Time–frequency spectrograms [46] showing residual data from LIGO Hanford (left), LIGO Livingston (middle) and Virgo (right) after waveform subtraction. Data for GW240925 and GW250207 are shown in the two top and bottom panels, respectively; for both signals, the upper panels are for results neglecting calibration uncertainty, and the lower panels are for those using a wide, uninformative prior for Hanford calibration and in-situ measured uncertainty for other detectors. Times are measured relative to the times reported from the search algorithms. The data have been whitened [13], and the scale bar shows the normalized energy (which has a reduced range compared to Fig. 1 of the main paper).

as shown in Fig. 14. The resulting constraints on the PN deviation parameters and the phenomenological post-inspiral parameters are reported as 90% upper bounds in Table IV. The TIGER bounds from GW250207 are the most stringent from a single GW observation for the 2PN and higher-order PN coefficients, as well as for the post-inspiral parameters excluding $\delta\hat{c}_\ell$, where GW250114_082203 is the most constraining [123–125].

To understand why GW250207 is particularly informative, we may consider its source properties. There is significant posterior support for near edge-on inclinations, a configuration that naturally enhances the visibility of higher-order spherical-harmonic moments, in particular the $(4,4)$ multipole [99], and the component masses are unequal (for comparison, GW250114_082203 does not have support for edge-on inclinations and is consistent with having equal component masses [7]). These characteristics lead to a non-trivial contribution of higher-order multipoles to the observed signal, which are correlated with precise measurements of the properties like chirp mass, mass ratio and component spins, as well as the deviation parameters themselves [120, 230]. Having precise measurements of the source properties is beneficial because deviation parameters are correlated with the underlying GR parameters, and such degeneracies often weaken constraints on the PN terms, even with many inspiral cycles in-band [124, 231]. The signal properties of GW250207 reduce these degeneracies, and allow the analyses to obtain stringent constraints on the higher-PN deviation parameters and the phenomenological post-inspiral parameters.

The TIGER inspiral bounds are generally weaker than those from FTI. In these PN-parametrized tests, the beyond-GR correction is included only in the inspiral regime, while the merger–ringdown sector remains fixed to its GR prediction. The difference in bounds between the two frameworks likely arises from the different choices of upper cutoff frequency for the beyond-GR correction. TIGER terminates these corrections at the $(2,2)$-multipole frequency at approximately the minimum-energy circular orbit $f_{22}^{\rm MECO}$, whereas FTI tapers the waveform at the peak frequency of the $(2,2)$ multipole $f_{22}^{\rm peak}$ [116, 120, 124]. For GW240925 (GW250207), the cutoff frequencies are approximately 259 Hz (64 Hz) for TIGER and 684 Hz (169 Hz) for FTI. The higher cutoff frequency in the FTI analysis leads to the tighter constraints [125].

We also investigate the impact of detector calibration on the

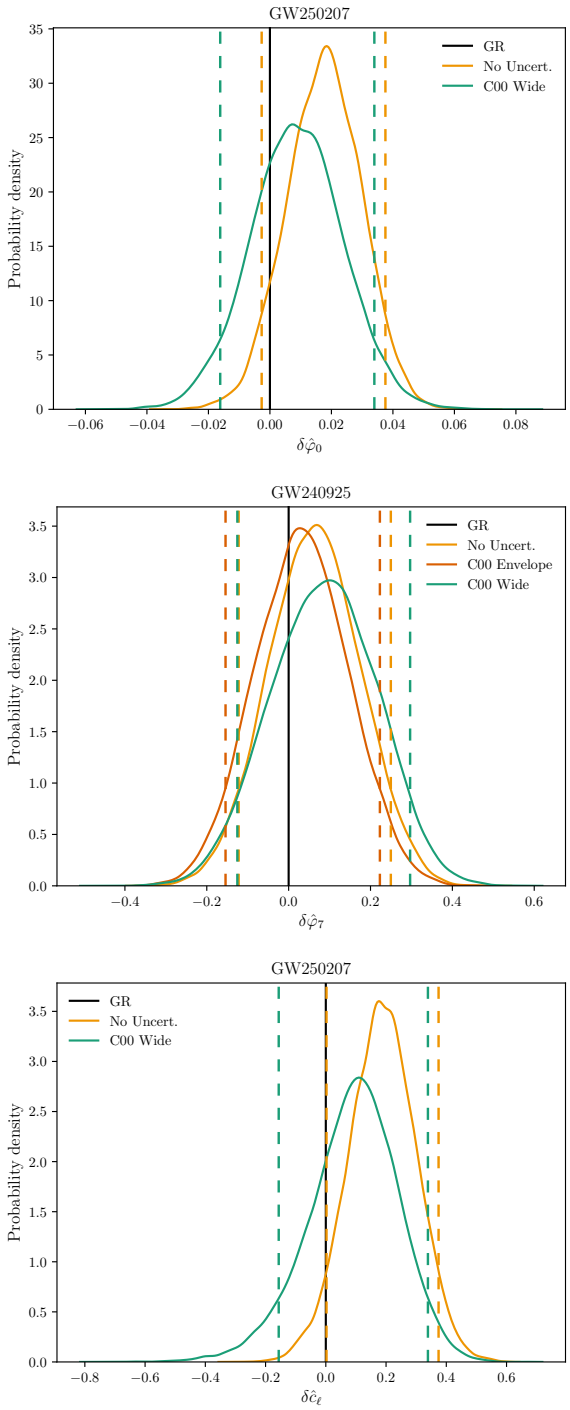

FIG. 14. Illustrative results from the FTI (top, middle) and TIGER (bottom) analyses for GW250207 and GW240925. The dashed lines indicate the 90% credible interval, and the solid black line indicates the GR value. Shown are selected deviation parameters; other parameters exhibit similar behaviors. Results are shown using a wide calibration prior for Hanford (green) and neglecting calibration uncertainty (yellow) for both signals. For GW240925, we additionally show results using the in-situ measured calibration prior for Hanford (orange). Neglecting calibration uncertainty leads to narrower posteriors and reduced agreement with GR.

PCA test of GR, which looks for correlated deviations across multiple PN orders simultaneously, thereby probing signatures of more complex departures from GR predictions [121, 122, 232, 233]. We perform PCA analyses with and without calibration uncertainty for each signal, using the same analysis settings and priors as in the source-parameter estimation. In the TIGER framework, we use the IMRPhenomXPHM waveform model [205, 206], while in the FTI framework, we adopt SEOBNRv5HM_ROM [229] as the baseline GR model and simultaneously vary six fractional PN deformation parameters between 1.5PN and 3.5PN order. We then apply PCA to identify linear combinations of PN deformation parameters that are best constrained by the data: those aligned with the eigenvectors corresponding to the smallest uncertainties define the principal directions of parameter covariance, with the leading component representing the linear combination of PN coefficients that is most tightly constrained. For GW250207, the PCA posteriors in both frameworks are consistent with the GR values. For GW240925, we only report results within the TIGER framework due to the computational cost of analyzing this longer signal; again we find consistency with GR. Incorporating wide, uninformative calibration priors broadens the PCA parameter posteriors and shifts their peaks closer to zero, improving agreement with GR relative to analyses that neglect calibration uncertainty. Figure 15 presents the 90% credible contours for the leading two PCA parameters, $\delta\hat{\varphi}^{(1)}_{\rm PCA}$ and $\delta\hat{\varphi}^{(2)}_{\rm PCA}$.

These results show that not including calibration uncertainty could potentially lead to biases in tests of GR. Using wide calibration priors when the calibration of the detector is unknown can prevent this from happening, at the cost of losing some constraining power.

Ringdown tests

We perform a range of QNM analyses using the ringdown [135–137], QNMRF [131–134], and pSEOBNR [126–128, 130] pipelines. For GW240925, the ringdown SNR is low, as expected for a lower-mass BBH, and is therefore not suitable for an in-depth ringdown test. The pSEOBNR analysis requires a SNR of $\rho \geq 8$ in both the inspiral and post-inspiral regimes to break the degeneracy between the QNM frequency deviation and the remnant mass [127], while the ringdown analysis requires a post-peak SNR of $\rho > 10$. Only GW250207 satisfies the SNR thresholds for both pSEOBNR and ringdown analyses. As a check, we perform the QNMRF analysis focusing on the dominant $(2, 2, 0)$ mode for GW240925. The resulting broad posteriors are generally uninformative for both the C00 and C01 data. Therefore, we focus on the results from GW250207, where the higher ringdown SNR enables a more informative test.

Both ringdown and QNMRF pipelines do not implement marginalization over calibration uncertainty, so we perform single-detector analyses of Hanford and Livingston data individually to explore results with different calibration errors. We

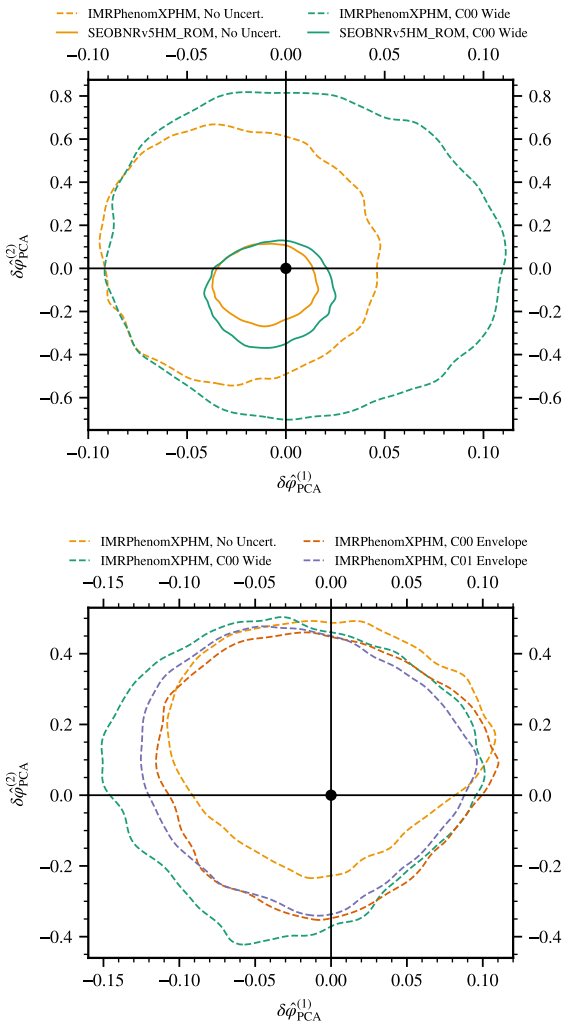

FIG. 15. The 90% credible contours for the leading two PCA parameters for GW250207 (top) and GW240925 (bottom). Results are presented for analyses that neglect calibration uncertainty (yellow) and those that adopt a wide prior on the Hanford calibration (green), for both signals, in the TIGER (dashed) and FTI (solid) frameworks. For GW240925, we additionally show results using the in-situ measured calibration priors applied to the Hanford miscalibrated C00 (orange) and recalibrated C01 (purple) data. Neglecting calibration uncertainty leads to narrower posteriors that peak further from zero, while incorporating a wide calibration prior yields wider posteriors that exhibit improved consistency with GR.

fit the dominant Kerr $(2,2,0)$ mode to the data over a ~ 1 ms range of late starting times, $t_{\rm peak}+\Delta t$, where $\Delta t \in [8,11] t_{M_{\rm f}}$ with $t_{M_{\rm f}} = G(1+z)M_{\rm f}/c^3$, and $t_{\rm peak}$ is the reference peak time of the strain. The reference peak time $t_{\rm peak}$, remnant mass $M_{\rm f}$, and extrinsic parameters are fixed to those from the maximum-likelihood posterior sample of the NRSur7dq4 IMR analysis using the wide calibration prior. To condition the data prior to fitting with ringdown, we high-pass filter the time series above a cut-off frequency of 10 Hz, downsample with an anti-aliasing digital filter [137] to a 2048 Hz sampling rate, and crop to a 0.66 s analysis segment beginning at the native 16384 Hz discretized sample closest to $t_{\rm peak}+\Delta t$. In the QNMRF analysis, we analyze the data over the intervals $[\Delta t, \Delta t + 0.2\,{\rm s}]$, downsampled at 4096 Hz. A check was also performed over longer 0.66 s segments to verify that differences in configuration between QNMRF and ringdown do not affect the results. We obtain consistent results from both pipelines: for all start times, the remnant black hole properties inferred from the Livingston data are consistent with the maximum-likelihood IMR result, while the measured $(2,2,0)$ QNM from the Hanford analysis are biased to lower frequencies and higher damping times, disagreeing with the full-signal inference at the 90% credible level. No evidence for an overtone is found in the Livingston-only analysis within this time window by either pipeline (e.g., with all QNMRF detection statistics falling below threshold [134]), thereby justifying a fit using only the fundamental $(2,2,0)$ mode.

The pSEOBNR analysis [126–130] introduces fractional deviations to the frequency and damping time of the fundamental QNMs in the underlying SEOBNRv5PHM waveform model, parametrized as

$$f_{\ell m 0} = f^{\rm GR}_{\ell m 0}(1+\delta\hat{f}_{\ell m 0}), \quad \tau_{\ell m 0} = \tau^{\rm GR}_{\ell m 0}(1+\delta\hat{\tau}_{\ell m 0}). \tag{9}$$

Unlike analyses that isolate the ringdown phase, pSEOBNR directly modifies parameters within an IMR waveform model, allowing it to leverage the full signal duration and total SNR, while avoiding ambiguities in the choice of the ringdown start time. The analysis constraints fractional deviations in the $(2,2,0)$ QNM in addition to the GR parameters of the waveform model, assuming uniform priors of $\delta\hat{f}_{220} \in [-0.8, 2]$ and $\delta\hat{\tau}_{220} \in [-0.8, 2]$. The high SNR of GW250207 also allows us to constrain fractional deviations in the $(4,4,0)$ QNM, assuming uniform priors of $\delta\hat{f}_{440} \in [-0.8, 0.8]$ and $\delta\hat{\tau}_{440} \in [-0.8, 0.8]$. Since this analysis can explicitly incorporate calibration uncertainties, we perform analyses both with and without calibration uncertainties, adopting a wide, uninformative prior for Hanford in the latter case. In both cases, the inferred remnant parameters and QNM deviations remain consistent with the IMR analysis within the 90% credible interval; however, neglecting calibration uncertainty reduces this level of agreement. The $(2,2,0)$ QNM is well constrained, with $\delta\hat{f}_{220} = 0.01^{+0.03}_{-0.03}$ and $\delta\hat{\tau}_{220} = -0.02^{+0.17}_{-0.15}$ when calibration uncertainty is incorporated, compared to $\delta\hat{f}_{220} = -0.01^{+0.02}_{-0.02}$ and $\delta\hat{\tau}_{220} = 0.12^{+0.14}_{-0.13}$ when it is neglected, for the analyses with fractional deviations in the $(2,2,0)$ QNM in addition to the GR parameters. The frequency of the $(4,4,0)$ QNM is constrained to $\delta\hat{f}_{440} = 0.03^{+0.20}_{-0.64}$ and $\delta\hat{f}_{440} = 0.00^{+0.12}_{-0.28}$ with and without incorporating calibration uncertainty, respectively. The damping time of the $(4,4,0)$ QNM remains unconstrained. The impact of calibration uncertainties is less pronounced in the pSEOBNR analysis, potentially because it incorporates data from all three detectors and uses a full waveform model, in contrast to single-detector, ringdown-only analyses of QNMRF and ringdown.